Impeller-Diffuser Interaction in Centrifugal Compressors

by

Yu Kwong Patrick Shum

B.Sc. University of Alberta (1990)
M.Sc. University of Alberta (1992)

Submitted to the Department of Aeronautics and Astronautics in partial fulfillment of the requirements for the degree of

Doctor of Philosophy

at the
Massachusetts Institute of Technology
February 2000

© Massachusetts Institute of Technology. All rights reserved.

Author__________________________________
Department of Aeronautics and Astronautics
October 29, 1999

Certified by__________________________________
Choon S. Tan
Senior Research Engineer, Gas Turbine Laboratory
Thesis Supervisor

Certified by__________________________________
Edward M. Greitzer
H. N. Slater Professor of Aeronautics and Astronautics
Associate Head of the Department

Certified by__________________________________
Mark Drela
Associate Professor of Aeronautics and Astronautics

Certified by__________________________________
Nicholas A. Cumpsty
Professor of Aerothermal Technology, University of Cambridge

Accepted by__________________________________
Nesbitt W. Hagood
Associate Professor of Aeronautics and Astronautics
Chairman, Department Graduate Committee

MASSACHUSETTS INSTITUTE OF TECHNOLOGY
SEP 07 2000
LIBRARIES
ARCHIVES

Impeller-Diffuser Interaction in Centrifugal Compressors

by

Yu Kwong Patrick Shum

Submitted to the Department of Aeronautics and Astronautics
on October 29, 1999, in partial fulfillment of the
requirements for the degree of Doctor of Philosophy

Abstract

A study has been conducted, using an unsteady three-dimensional Reynolds-averaged Navier-Stokes simulation, to define the effect of impeller-diffuser interaction on the performance of a centrifugal compressor stage. The principal finding from the study was that the most influential aspect of this unsteady interaction was the effect on impeller tip leakage flow. In particular, the unsteadiness due to the upstream potential effect of the diffuser vanes led to larger viscous losses associated with the impeller tip leakage flow. The consequent changes at the impeller exit with increasing interaction were identified as reduced slip, reduced blockage, and increased loss. The first two were beneficial to pressure rise while the third one was detrimental. The magnitudes of the effects were examined using different impeller-diffuser spacings and it was shown that there was an optimal radial gap size for maximum impeller pressure rise. The physical mechanism was also determined: when the diffuser was placed closer to the impeller than the optimum, increased loss overcame the benefits of reduced slip and blockage. The findings provide a rigorous explanation for experimental observations made on centrifugal compressors. The success of a simple flow model in capturing the pressure rise trend indicated that although the changes in loss, blockage and slip were due largely to unsteadiness, the consequent impacts on performance were mainly one-dimensional. The influence of flow unsteadiness on diffuser performance was found to be less important than the upstream effect, by a factor of seven in terms of stage pressure rise in the present geometry. It is thus concluded that the beneficial effects of impeller-diffuser interaction on overall stage performance come mainly from the reduced blockage and reduced slip associated with the unsteady tip leakage flow in the impeller.

Thesis Supervisor: Choon S. Tan
Title: Senior Research Engineer, Gas Turbine Laboratory

Acknowledgments

This project was made possible because of the generous support from Ishikawajima-Harima Heavy Industries Co. Ltd, with Mr. Hideaki Tamaki as technical monitor. Additional funding was provided by the NASA Glenn Research Center NAG3-1598 and NAG3-2101 with Dr. D. Reddy as Technical Monitor and Dr. K. Suder as Contract Monitor, and Allied Signal Inc. Contract No. E391868 with Dr. A. Sehra [1] as technical monitor. Thanks also go to the NASA ACCL computational support staff for their assistance.

I would like to thank my advisor, Dr. Choon S. Tan, for taking me under his wing. Dr. Tan's dedication to my understanding and his faith in my abilities deserves my total gratitude. Professor Edward Greitzer always kept me focused on the problem at hand, and taught me the intricacies of internal/compressible/one-dimensional flows. I am indebted to Professor Nicholas Cumpsty and Professor William Dawes (University of Cambridge) who provided invaluable advice on fluid mechanics issues and the numerical code. Advice from Professor Mark Drela, Professor Frank Marble (Caltech), Dr. Jerry Wood (NASA) and minor program supervision from Professor Steve Hall are always appreciated. Post-processing was performed using Professor Jaime Peraire's FELISA and Mr. Robert Haimes's VISUAL3.

Thanks go to Dr. Yifang Gong who always provide me with superb technical and political insights and warm hospitality during F-1 race weekends, very important! Thanks go to Takeo Kuraishi for sharing his expertise in both software/hardware and friendship. Thanks go to Dr. Sabri Deniz who are always enthusiastic in showing me the latest technical paper. Also appreciated are the friendship and technical help from Mike Phillips, Duc Vo, Yang Tzeng and Hiroki Ugajin on grid generation, blockage, vortex tracing, run strategy, etc. Finally, thanks go to Ms. Holly Anderson and Ms. Lori Martinez for solving the real world problems I encountered in GTL.

Besides the students named above, I also want to show my appreciation to GTL people Jinwoo, Keith, Tony, Shengfang, Sanith, Luc, Amit, Steve, Ken, Jinwook, Joe, Dan and many others for their support, exchange of view and gossips (mostly via Duc) in some weird owl hours. Outside GTL, I have the privilege to hang out with some cool (relatively) friends ShinJuh Chen, John Fung, Masa Ikuta, Robert Sung and Tony Eng. Besides the very warm friendship and the occasional free food, they also provided me with some sensible alternatives to the MBTA.

For those who cared the most, my family, who have never questioned my spending all these years (cash and time), here is my thesis. I also want to dedicate this work to my little niece Caitlyn and little cousin Anita.

---

[1] presently with NASA

CONTENTS

Nomenclature **15**

1 Introduction **19**

1.1 Background and Motivation 19

1.2 Review of Previous Work 22

1.3 Research Objectives and Problem Statement 24

1.4 Contributions of Thesis 24

1.5 Outline of Thesis 26

2 Technical Approach **29**

2.1 Description of Solution Algorithm 29

2.2 Computational Grid 30

2.3 Code Validation 32

2.4 Control Numerical Experiment 35

2.4.1 Influence of Interaction on Impeller Flow 35

2.4.2 Influence of Interaction on Diffuser Flow 36

3 Influence of Interaction on Impeller Flow **43**

3.1 Introduction 43

3.2 Numerical Results 44

3.3 Explanation of Observations 46

3.3.1 One-Dimensional Model of Impeller Total Pressure Ratio . . . 46

3.3.2 One-Dimensional Model on Impeller Static Pressure Ratio . . 50

3.3.3 Flow Visualization on Computed Flow Field 52

3.4 Summary 57

4 Influence of Interaction on Diffuser Flow and Stage Performance 81

4.1 Introduction 81

4.2 Numerical Results 82

4.3 Explanation of Observations 83

4.3.1 Effect of Interaction on Diffuser Performance 83

4.3.2 Effect of Interaction on Stage Total-to-Static Pressure Ratio . 86

4.4 Summary 87

5 Synthesis of Computed Results for Centrifugal Compressor Stage 95

5.1 Guidelines for Numerical Simulation 95

5.2 Comments on Current Design Trends 97

6 Conclusion 99

6.1 Overview of Research Contributions 99

6.1.1 Generic Findings 99

6.1.2 Specific Findings 100

6.2 Implications in Future Design 101

6.3 Recommendations for Future Study 101

A Time-Averaging Procedures for Diffuser Inlet Nodes 103

B Development of One-Dimensional Quasi-Steady Flow Model 105

C Blockage Evaluation 107

Bibliography 109

LIST OF FIGURES

1-1 A cutaway schematic of a centrifugal compressor stage with geometry obtained from Krain [26] 27

2-1 The unstructured mesh used for the $r_{2'}/r_2 = 1.092$ configuration with the casings of both impeller and diffuser removed 40

2-2 The relationship between radial velocity V_{r2} and tangential velocity V_{t2} at impeller exit for the 9.2% radial gap configuration, both speeds non-dimensionalized by U_2 41

2-3 Correlations between polytropic efficiency η_{poly} and specific speed N_s reproduced from [5], with the present data point added 41

2-4 Comparison of respective grid for diffuser calculations 4 and 5 42

3-1 Effect of radial gap size $r_{2'}/r_2$ on impeller performance, reproduced from [37] 61

3-2 Impeller total-to-total pressure for the three different radial gap sizes, with the complete characteristic of $r_{2'}/r_2 = 1.092$ case shown 62

3-3 Mass and time averaged total pressure distribution along the impeller passage for the three different radial gap sizes 63

3-4 Instantaneous total-to-static pressure ratio p/p_{01} along impeller passage centerline of the $r_{2'}/r_2 = 1.092$ configuration, obtained at 8 different instants of one period with equal time intervals in between . . 64

3-5 Rms time fluctuation of static pressure along impeller passage centerline of the $r_{2'}/r_2 = 1.092$ configuration, non-dimensionalized against impeller exit dynamic pressure $p_{02} - p_2$ 65

3-6 Velocity triangle at the impeller exit 66

3-7 Effect of radial gap size on impeller total pressure ratio and static pressure ratio, expressed in increment change from the vaneless configuration 66

3-8 Contours of entropy production $\rho\frac{Ds}{Dt}$ at impeller exit for vaneless configuration 67

3-9 Contours of entropy production $\rho\frac{Ds}{Dt}$ at impeller exit for $r_{2'}/r_2 = 1.092$ $(t = 0.000T)$ 67

3-10 Contours of entropy production $\rho\frac{Ds}{Dt}$ at impeller exit for $r_{2'}/r_2 = 1.092$ $(t = 0.125T)$ 67

3-11 Contours of entropy production $\rho\frac{Ds}{Dt}$ at impeller exit for $r_{2'}/r_2 = 1.092$ $(t = 0.250T)$ 68

3-12 Contours of entropy production $\rho\frac{Ds}{Dt}$ at impeller exit for $r_{2'}/r_2 = 1.092$ $(t = 0.375T)$ 68

3-13 Contours of entropy production $\rho\frac{Ds}{Dt}$ at impeller exit for $r_{2'}/r_2 = 1.092$ $(t = 0.500T)$ 68

3-14 Contours of entropy production $\rho\frac{Ds}{Dt}$ at impeller exit for $r_{2'}/r_2 = 1.092$ $(t = 0.625T)$ 69

3-15 Contours of entropy production $\rho\frac{Ds}{Dt}$ at impeller exit for $r_{2'}/r_2 = 1.092$ $(t = 0.750T)$ 69

3-16 Contours of entropy production $\rho\frac{Ds}{Dt}$ at impeller exit for $r_{2'}/r_2 = 1.092$ $(t = 0.875T)$ 69

3-17 Incremental entropy production $\Delta(\rho\frac{Ds}{Dt})$ for the two vaned configurations when compared to the vaneless configuration 70

3-18 Time averaged accumulated tip leakage mass flow $\frac{\dot{m}_{tip}}{\dot{m}}$ for three different radial gap sizes 71

3-19 Comparison of main blade clearance periodic tip leakage mass flux at 90%, 95%, 99% meridional stations for three different radial gap sizes 72

3-20 Comparison of splitter clearance periodic tip leakage mass flux at 90%, 95%, 99% meridional stations for three different radial gap sizes . . . 73

3-21 Comparison of periodic main blade tip loading $\frac{p_{ps}-p_{ss}}{p_{02}-p_2}$ at 90%, 95%, 99% meridional stations for three different radial gap sizes 74

3-22 Comparison of periodic splitter tip loading $\frac{p_{ps}-p_{ss}}{p_{02}-p_2}$ at 90%, 95%, 99% meridional stations for three different radial gap sizes 75

3-23 Comparison of entropy rise $\frac{s-s_1}{C_p}$ at the 90% meridional station between three different radial gap sizes 76

3-24 Comparison of entropy rise $\frac{s-s_1}{C_p}$ at the 95% meridional station between three different radial gap sizes 77

3-25 Comparison of entropy rise $\frac{s-s_1}{C_p}$ at the 99% meridional station between three different radial gap sizes 78

3-26 Comparison of non-dimensional mass flux at the 99% meridional station between three different radial gap sizes 79

4-1 Comparison of local swirl angle (in degrees) at the diffuser vane leading edge plane at $r/r_2 = 1.092$ after elimination of upstream non-uniformities: unsteadiness and axial distortions 89

4-2 Comparison of pressure recovery C_p and loss C_{loss} for calculations 2, 4, 5 90

4-3 Effect of unsteadiness on the swirl angle at mid-pitch of the diffuser inlet plane 91

4-4 Comparison of time-averaged pressure distribution ($\Delta\left(\frac{p-p_2}{p_{02}-p_2}\right) = 0.05$) around the leading edge region at three different axial planes for the $r/r_2 = 1.092$ configuration (Calculation 2) 92

4-5 Comparison of pressure distribution ($\Delta\left(\frac{p-p_2}{p_{02}-p_2}\right) = 0.05$) around the leading edge region at three different axial planes for the diffuser alone calculation with upstream unsteadiness eliminated (Calculation 4) . . 93

LIST OF TABLES

2.1 Comparison of measured and computed performance parameters generated from the 9.2% radial gap configuration 39

2.2 Comparison of diffuser inlet conditions for calculation 2, 4, 5 39

3.1 Comparison of computed impeller performance parameters from different radial gap size ($r_{2'}/r_2$) 59

3.2 Incremental changes of independent variables in the impeller flow field due to vanes being placed downstream 59

3.3 Relative importance of independent factors for impeller total pressure ratio 60

3.4 Comparison of accumulated tip leakage mass flow at impeller trailing edge for different radial gap size 60

4.1 Change of stage total-to-static pressure ratio and other performance parameters due to a reduction of radial gap size $r_{2'}/r_2$ from 1.092 to 1.054 88

C.1 Effect of the velocity gradient cut-off value on the computed $\frac{\Delta A_{eff}}{A_{eff}}$ . . 108

NOMENCLATURE

A	channel geometrical area
A_{eff}	effective passage area at impeller exit
B	blockage
b	blade thickness
C_A, C_s, C_θ	influence coefficients for total pressure perturbation
$C_{\tilde{A}}, C_{\tilde{s}}$	influence coefficients for static pressure perturbation
C_{loss}	diffuser loss coefficient
C_p	diffuser pressure recovery coefficient, defined in Equation 2.1
C_{p0}	specific heat capacity at constant pressure
C_x	axial velocity in axial machine
c	chord for axial machine
D	impeller diameter
d	general deviation
K_{p02}, K_{p2}, K_{Cp}	influence coefficients for stage pressure rise perturbation
k	turbulent kinetic energy
k_e	thermal conductivity
M	Mach number
$\dot{m}$	mass flow
N	blade count
N_s	impeller specific speed
n	number of time steps in one period
p, p_0	static, total pressure
R	gas constant
r	radial coordinate
s	entropy
T, T_0	static, total temperature
T	period, blade passing
t	time

U	impeller speed $= r \times \Omega$
V	absolute velocity
V_s	slip velocity
W	relative velocity
x	axial coordinate (from diffuser hub to shroud)

Greek

α	absolute swirl angle referenced to the meridional direction
β	reduced frequency
γ	specific heat ratio
Δ	incremental change from vaneless configuration
Δ'	incremental change due to reduction of radial gap size
δ	change due to elimination of non-uniformities
ε	turbulent dissipation rate
η_{isen}, η_{poly}	impeller isentropic and polytropic efficiency
θ	relative flow angle referenced to the meridional direction
ρ	density
σ	slip factor
τ_{ij}	stress tensor
χ	blade angle (measured from meridional direction)
Ω	impeller rotation speed

Superscripts, Subscripts and Operators

1	at impeller inlet
2	at impeller exit or same as vaneless space inlet
2+	interaction plane location where impeller grid and diffuser grid meets
2'	at diffuser inlet or same as vaneless space exit
3	at diffuser exit
e	edge, blocked region boundary
m	meridional
mp	mid-pitch, midway between the diffuser vane leading edges
ps	pressure side
r	radial
rel	in relative (impeller) frame
ss	suction side

t	tangential
tip	tip-leakage
overbar	time-averaged quantities, only for expression with both time-averaged and instantaneous quantities present

CHAPTER 1

INTRODUCTION

1.1 Background and Motivation

Centrifugal compressors have many applications, ranging from ground-based turbochargers to helicopter gas turbine engines. Other potential high technology applications include microengines [13] and artificial hearts [35]. The biggest advantage of *centrifugal* compressor over its *axial* counterpart is fabrication cost as it has fewer parts.

A centrifugal compressor stage consists of a rotating impeller and a stationary diffuser. As shown in Figure 1-1, flow enters the impeller axially and exits radially through a 90 degree bend. Compared to axial machines with the same diffusion factor, a much higher pressure ratio, up to 10:1 [20], can be obtained by centrifugal machines because most of the impeller pressure rise is associated with the centrifugal force field. However, a substantial part of the impeller work is in the form of high absolute exit velocity. The function of the diffuser is to recover this remaining dynamic pressure by decelerating the swirling flow, and efficient operation of the diffuser is crucial for obtaining satisfactory overall stage pressure ratio [5, 20].

The inlet condition to the diffuser is characterized by the highly non-uniform impeller outflow, which is commonly referred to as the "jet and wake" structure. This is a result of secondary flow induced by the blade-to-blade and axial-to-radial turning. The flow non-uniformity is further exacerbated in an unshrouded impeller, in which high-entropy fluid resulted from the tip-leakage gets collected in the vicinity of the casing-suction surface corner [11].

Models of vaneless diffuser flow are available, including the one developed by Dean and Senoo [8]. This model allows the interaction between jet and wake in the diffuser. Their calculation suggests that the rapid attenuation of flow distortions can be attributed to the reversible energy transfer between the two regions. As a result, most of the diffuser loss is caused by wall friction. Another model by Johnston and Dean [23] assumes the diffuser inlet flow is mixed out to a uniform state through a sudden expansion, so most of the diffuser loss is attributed to the mixing loss at the inlet. Inoue [21] compared these two models and found that both predicted similar loss for a wide range of inlet conditions with typical design parameters, despite the fundamentally different assumption involved in each model. He also verified that the reversible energy exchange increased with the incoming swirl into the diffuser.

The interaction between impeller and vaned diffuser is more difficult to model. This is reflected by Cumpsty's [5] comment that mismatching is far more common as a cause of poor performance with high pressure ratio machines than details of impeller or diffuser vane shape. Individual component's satisfactory performance does not guarantee the integrated design will also have satisfactory flow range and overall stage efficiency. Engineers have used empirical method to account for impeller-diffuser interaction in designs [3, 37, 4]. Rodgers' [37] and Clements et al.'s [4] results are particularly important to the current investigation. Both demonstrate there is an optimum impeller-diffuser gap size for maximum impeller pressure rise and efficiency. The findings show that impeller-diffuser interaction can have impact on stage performance.

Inoue and Cumpsty [22] have found that the circumferential distortion from the impeller attenuates rapidly in the entrance region of a vaned diffuser. This suggests that the presence of the vanes enhances the flow uniformity coming into the diffuser. The current industrial trend is to have the vaneless region shortened as much as possible to increase efficiency [11], magnifying such effect. Consequently, the impact of impeller-diffuser interaction on performance needs to be addressed.

Until now, axial flow machines have attracted substantially more attention than centrifugal machines because of their mission-critical roles in aviation. Experimental observation on the influence of blade row interaction on stage performance has been made by different parties [19, 30] for axial machines. Similar to Rodgers' [37] findings in centrifugal machines, their results show that rotor-stator spacing can affect stage pressure ratio in axial machines. Of the investigations focused on the influence of blade row interaction on upstream rotor flow, Shang et al. [39] found that the upstream potential field of a stator could lead to substantial circumferential flow non-uniformity at rotor exit, with the magnitude of the circumferential non-uniformity dependent on the rotor-stator spacing.

With the advance of computational fluid dynamic (CFD) capabilities, researchers can examine the mechanisms of how the flow reacts to blade row interaction. Such observation would otherwise be difficult to make experimentally. Meece [29] has reported that rotor-stator spacing can affect time-averaged performance after conducting CFD simulation on various turbine designs. Another example is the recent work by Valkov and Tan [43, 44], who investigated how disturbances from upstream were transported through downstream components. They linked a possible performance improvement to the reversible recovery of the energy in both the rotor blade wake and the tip vortex. It is doubtful that their findings in the axial stator can be applied directly to the diffusers of centrifugal machines, because diffuser geometry limits the amount of wake stretching, which is an essential step in the wake recovery process.

Also using CFD, Graf [16] has found that the unsteady response of the rotor tip vortex can be a measurable contributor to performance change. His conclusion is that closer coupling between the rotor and stator can improve the endwall flow field in both loss and blockage, at the expense of more rotor profile loss and stator loss away from the tip region. Hence a trade off between these effects may be warranted. Influences of downstream stator pressure field on the tip clearance vortex blockage and loss were also observed by Graf and Sharma [17] when they substituted the conventional radial stator profile with a bowed one. It is likely that Graf's observations also apply to centrifugal compressor, because impeller-diffuser coupling (radius ratio $r_{2'}/r_2 \sim 1.1$) is typically stronger than rotor-stator coupling in an axial machine (axial spacing between 0.20 to 0.40 blade chords [43]). A goal of this project is to model the influence of impeller-diffuser interaction on upstream flow. Such a model is a useful design tool to estimate engineering tradeoffs between different configurations.

1.2 Review of Previous Work

Three-dimensional flow calculations are feasible nowadays, allowing designers to have a better estimate of the influence of spatial flow non-uniformity on performance. Computation results from Dawes [6] and experimental observations from Tamaki [42] have shown that the intensity of separation on diffuser leading edge can be different from hub to shroud, suggesting that any realistic flow simulation has to be done on a three-dimensional basis. However, Phillips [33] has shown that axial distortion at the diffuser inlet has little influence on diffuser pressure recovery, because energy transfer in the axial direction helps energize the region with high flow incidence misalignment, allowing flow re-attachment and preserving diffuser pressure recovery. This is also the reason why diffuser pressure recovery coefficient correlates so well with diffuser inlet momentum averaged flow angle only. A large amounts of diffuser performance data fitting into this one-dimensional parameter relationship has been demonstrated experimentally [9, 10, 14, 15].

Another issue in impeller-vaned diffuser interaction is the role of unsteadiness in affecting stage performance. Not until recently can researchers simulate impeller-diffuser interaction using time-accurate stage calculations [6, 32]. Muggli et al. [32] simulated a water pump diffuser with a time periodic inlet profiles and concluded that there was no substantial difference in the resulting time-averaged flow field and pressure ratio, when compared to those generated with a steady inlet profiles. Dawes' [6] comparison of the results of a time-accurate stage calculation performed at a high subsonic condition against that of an equivalent steady diffuser calculation also suggests that the contribution of unsteadiness to the entropy production is small (in the order of 5% of the total time-averaged entropy production in the diffuser). However, it should be recognized that both studies were performed at subsonic condition for low stage total-to-static pressure ratio ($p_3/p_{01} < 2$), while current industrial standard designs ($p_3/p_{01} > 5$), operate at transonic conditions. Neither study addressed how interaction can affect the flow field in the impeller.

Of the experimental investigations on how impeller-diffuser interaction affects upstream flow, Pinarbasi and Johnson [34] have confirmed that the presence of the diffuser vanes can influence the flow in the vaneless space in the form of circumferential non-uniformity. A similar observation was made by Arndt et al. [1], whose centrifugal water pump tests show that increasing the number of diffuser vanes reduce the impeller blade pressure fluctuations. Both studies were conducted at low speed, with tip Mach number on the order of 0.1.

Kirtley and Beach [25] investigated the influence of impeller-diffuser interaction on upstream flow by applying CFD to a configuration with tip Mach number of about 0.5. They used body force modeling and deterministic stresses to avoid the necessity of time-accurate calculation. By comparing the divergence of the deterministic stress to that of the Reynolds stress, they came to a conclusion that vane-induced unsteadiness was more important than turbulence in affecting the flow field upstream of the diffuser vanes. Similar to what Graf [16] observed in axial machine, they also found that the impeller flow in the stage calculation had less shroud separation compared to the isolated impeller flow, and they attributed the observation to the additional blockage the diffuser vanes provided. Since then, Dawes [6] and Domercq et al. [12] have demonstrated that time-accurate simulation with a sliding plane approach can be a feasible tool for studying interaction, as detailed unsteady flow features can be captured in the interaction region. Their findings indicate that the presence of diffuser vanes can affect the impeller flow.

1.3 Research Objectives and Problem Statement

This thesis examines the impact of unsteady impeller-diffuser interaction on the performance of a centrifugal compressor stage, most notably the stage total-to-static pressure ratio. The objectives of the investigation were:

- To assess the importance of interaction on the impeller and diffuser flow fields in terms of time averaged pressure rise capability, loss, blockage, etc., and the consequence for the stage performance.
- To determine the mechanisms by which interaction influences the above figures of merit for performance, especially the stage total-to-static pressure ratio.
- To develop a simple model to describe the observed phenomenon for preliminary design evaluation.

To accomplish the above objectives, the following fluid dynamic questions need to be addressed:

- How do downstream conditions, in the form of an unsteady pressure field, affect the impeller performance?
- How do upstream conditions, characterized by the rotating jet-and-wake structure, affect the diffuser performance?
- Can flow coupling between the impeller and the diffuser benefit stage performance when compared to that of vaneless configuration, and under what conditions can this occur?

1.4 Contributions of Thesis

The time-averaged computational results demonstrate that the most influential aspect of the impeller-diffuser interaction is the unsteady influence on impeller tip leakage flow. The unsteadiness can lead to an increase in the stage total-to-static pressure ratio, by about 2% in the current geometry, because of its influence on the following quantities at the impeller exit:

- Increased loss;
- Reduced blockage;
- Reduced slip.

The response of the impeller tip-leakage flow to the downstream unsteady pressure field is identified as the mechanism responsible for the changes outlined above. A one-dimensional model which relates the impeller pressure ratios (total-to-total and total-to-static) to the above three quantities is developed. This model is tested against the three-dimensional time-accurate CFD results and gives satisfactory estimates of the incremental change of impeller pressure ratios, 3.1% for total-to-total and 1.4% for total-to-static respectively, when the radial gap between the two components is reduced.

The unsteadiness from upstream is found to have little effect on the diffuser pressure recovery. The effect is roughly equivalent to a 0.3 degree change in the swirl angle at the diffuser inlet. Such magnitude is in the same order as that due to axial non-uniformity at the diffuser entrance, or one order smaller than the flow angle range acceptable by a vaned diffuser.

Combining the above two observations, it is concluded that the impact of impeller-diffuser interaction on the stage pressure ratio is largely due to the change in the impeller flow, instead of the change in diffuser performance. The former is seven times more influential than the latter, in terms of the change observed in stage total-to-static pressure ratio in the current geometry. Also, the competing effects of increased loss and reduced blockage, both brought about by closer coupling, is the main reason for the observed optimum radial gap when maximizing pressure rise capability. The detrimental effect of increased loss can overtake the beneficial effect of reduced blockage and slip, thus this thesis explains why bringing impeller and diffuser closer will not necessarily enhance pressure rise, as observed in known experimental studies.

1.5 Outline of Thesis

This thesis is organized in the following manner:

Chapter 2 presents the overall approach and methodology and provides descriptions of the CFD codes utilized. Measures aimed at overcoming difficulties encountered in grid generation and achieving convergence will also be discussed, followed by a summary of code validation.

Chapter 3 covers the impact of interaction on the impeller flow field, including the one-dimensional flow model which describes how these changes affect impeller pressure rise capabilities. The flow mechanisms responsible for the changes will also be presented.

Chapter 4 covers the impact of interaction on the diffuser performance. Its relative importance compared to other diffuser inlet factors or the change occurs upstream will be discussed.

Chapter 5 provides a synthesis of results by discussing how findings in the previous two chapters can help engineers in implementing future design evaluations.

Chapter 6 incorporates a summary of findings, the implications of this study, and recommendations for future work.

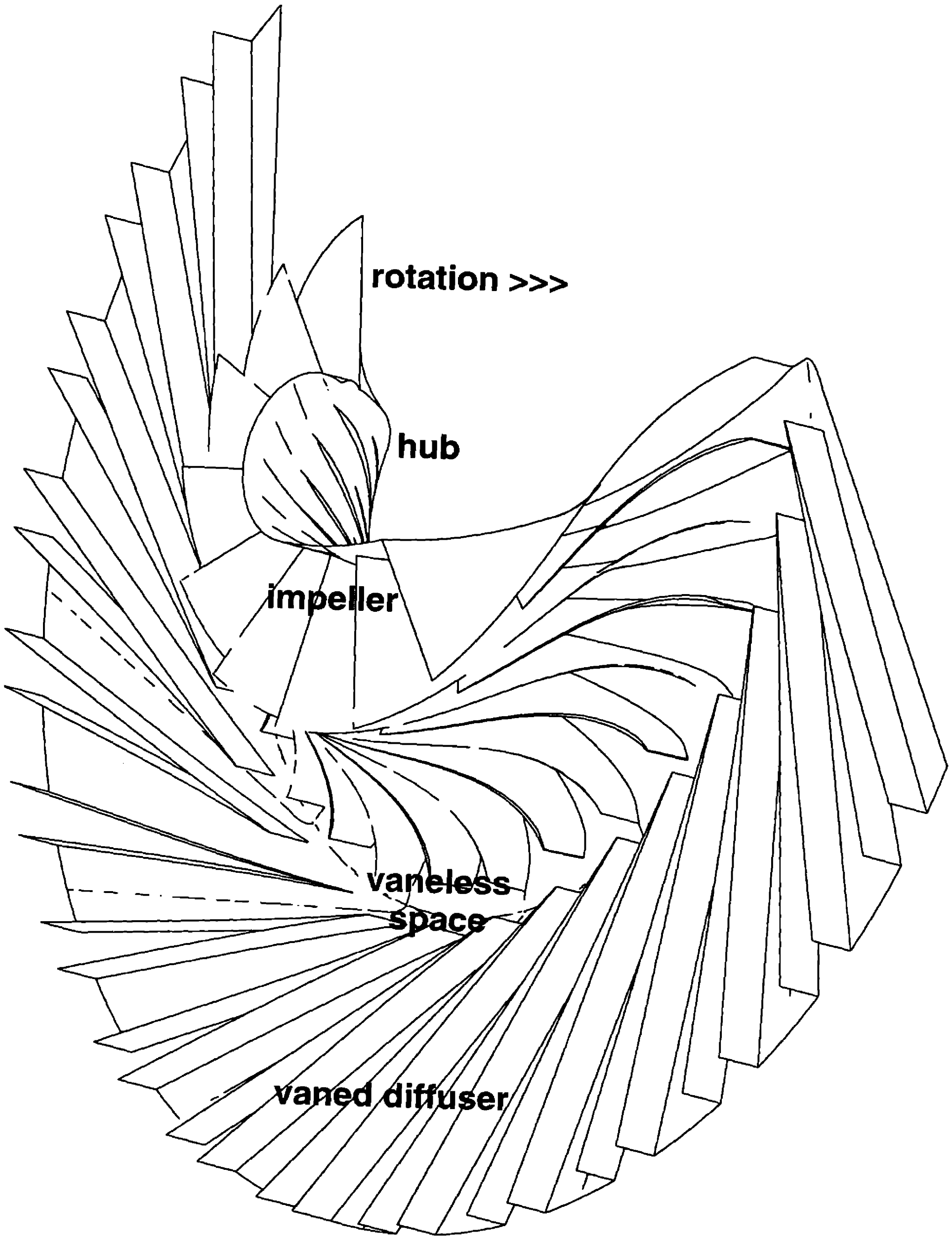
rotation >>>
hub
impeller
vaneless
space
vaned diffuser

Figure 1-1: A cutaway schematic of a centrifugal compressor stage with geometry obtained from Krain [26]

CHAPTER 2

TECHNICAL APPROACH

2.1 Description of Solution Algorithm

With continuing growth in the availability of computational resources, it has become feasible to simulate the unsteady flow field of a centrifugal compressor stage. The code utilized for the present study was provided by Dawes [6]. It simulates the impeller motion and employs a *sliding plane* to transfer axial and circumferential distortions between impeller and diffuser flow field at each time step with no modification to the distortions. A volume weighted interpolation procedure is adopted to ensure conservation. Besides preserving the flow details in the interaction region, the sliding plane approach also streamlines the algorithm because the entire flow field including the moving impeller can be evaluated in the absolute frame.

The equations being solved are the five fully three-dimensional, unsteady, compressible, Reynolds-averaged Navier-Stokes equations expressed in strong conservation form, coupled to two additional equations for the k-ε turbulence model. The seven equations are discretised in finite volume form on each of the tetrahedral control volumes with vertex variable storage, and time-marched to convergence using a four step Runge-Kutta residual smoothing procedure.

At the inflow boundaries the total pressure (p_{01}), total temperature (T_{01}), the two flow angles, turbulent kinetic energy (k_1), turbulent dissipation rate (ε_1) and the two flow angles are prescribed, while at the outflow boundaries the static pressure (p_3) is specified. The time-averaged mass flow of the stage is computed instead of being specified. Wall functions are employed to avoid the need of simulating the laminar sub-layer, allowing coarser grid at the viscous surface.

As it will be explained in the next section, the flow field is adjusted to have a cyclic repetition with one period equals to one blade passing. The number of steps per period should be maintained upwards of 500 [7], and for this reason the CFL number for all the time-accurate calculations in this investigation is limited to 0.75.

2.2 Computational Grid

The centrifugal compressor stage selected for this investigation is representative of a stage from current industry design. The important design variables are summarized as follows:

- impeller blade count: 17 main blades + 17 splitters
- impeller blade backsweep = 52°
- impeller tip clearance = 2% of impeller exit height
- diffuser blade count: 19 main wedges + 19 splitters
- radius ratio of diffuser entrance to impeller exit, $r_{2'}/r_2 = 1.092$
- radius ratio of diffuser discharge to impeller exit, $r_3/r_2 = 1.46$
- throat aspect ratio = 1.65
- length to width ratio of diffuser channel = 4.5
- channel divergence angle = 7.5°
- diffuser vane stagger angle = 17.6°

The unstructured mesh generated for the present numerical simulation is shown in Figure 2-1. The casings of both the impeller and diffuser are removed to show the location of the splitters.

Although the flow domain can be described by a three-dimensional rectangular array, an unstructured mesh (tetrahedral cells) is used instead of a structured mesh (cubic cells). The decision was made after communication with Dawes [7] who indicated that an unstructured mesh held the advantage over a structured mesh in terms of numerical stability due to grid skewness in the interaction region. The resulting mesh thus consists of close to 70000 nodes.

As seen in Figure 2-1, the number of impeller blades has been increased to 19 from 17 to allow a periodic unit of 1 main impeller blade per 1 main diffuser vane. The thickness of the impeller blade has been adjusted accordingly so that the area of flow passage is preserved. It has been verified that the blade increase has negligible effect on the impeller performance, and most importantly the adjustment does not cause any choking. The advantage of the one-to-one blade ratio is the enormous saving in computational resources because the necessity of modeling the entire annulus is avoided.

Another saving comes from the blade tip region where the gap between the casing and the blade tip is modeled by three grid points. Storer and Cumpsty [41] have shown that the tip-leakage flow is controlled by a primarily inviscid mechanism, thus even with relatively coarse mesh the static pressure field and the magnitude of leakage flow rate can be predicted very satisfactorily. Lately Van Zante et.al. [45] have pointed out that a substantially finer grid is required to resolve the important details of the wall-bounded shear layer which is responsible for the formation and structure of the tip leakage vortex. Such details are crucial for stall inception prediction. The focus of the present investigation is on understanding how the blockage associated with leakage flow reacts to downstream unsteadiness (rather than capturing the flow mechanisms responsible for stall inception), and the operating point is not close to the stall point, so such grid refinement appears to be unnecessary.

2.3 Code Validation

The code was developed by Dawes [6] and has been validated using a stage designed by Krain [26] with a total-to-static pressure ratio of 1.7. The capability of the code in simulating the flow field, including velocity profiles and vortex structure, has been assessed. Thus, the present validation will focus only on global performance parameters.

The following prescribed conditions are required when the code is applied to the grid described in the last section:

- impeller speed $U_2 = 622\mathrm{m/s}$
- impeller inlet flow at standard atmospheric conditions with $p_{01} = 1.013\mathrm{N/m}^2$, $T_{01} = 288\mathrm{K}$
- no pre-swirl in the impeller inlet flow

The diffuser exit pressure p_3 is chosen so that the computed time-averaged mass flow matches the target of 1.77 kg/s.

As it will be seen in the next chapter, unsteadiness only appears in the impeller in the last 10% of the flow path. Thus one good indicator of convergence is the flow field of this interaction region (mass flux, pressure, local Mach number, etc.) settling into a periodic state. Another indicator of convergence is the mass flow at the impeller entrance settling to a steady value. Depending on the prescribed initial condition, convergence can be achieved in about 1.5 through-flow times, or about 30 blade passings.

As stated above, comparison of computed results and experimental measurements are made based on one-dimensional time-averaged global performance parameters only. They are listed in Table 2.1, where diffuser pressure recovery coefficient C_p is defined as,

$$C_p = \frac{p_3 - p_2}{p_{02} - p_2} \tag{2.1}$$

and diffuser loss coefficient C_{loss} is defined as,

$$C_p = \frac{p_{02} - p_{03}}{p_{02} - p_2} \tag{2.2}$$

It can be seen in Table 2.1 that the experimental and computational results have excellent agreement in terms of diffuser performance, expressed in C_p, C_{loss}, and the highest Mach number, although larger discrepancies (about 4%) show up in both impeller pressure ratios p_{02}/p_{01} and p_2/p_{01}. According to the work by Rhie et al. [36], industry practice typically uses 200000 nodes per blade row, while the present impeller grid consists of less than 40000 nodes (see Figure 2-1). Thus, the prediction accuracy can be improved further by refining the impeller grid. Nevertheless, since an objective of this investigation is to study performance *trends* when impeller-differ interaction intensifies, it is the incremental performance change from one configuration to another which will be focused on. Therefore, prediction discrepancies as above are acceptable as long as the code produces consistent results.

The capability of the code in predicting performance trend can be demonstrated by plotting the non-dimensional tangential velocity V_{t2}/U_2 against the non-dimensional radial velocity V_{r2}/U_2. Data are readily available because several runs were conducted to find the corresponding p_3 for the target mass flow. As shown in Figure 2-2, the results demonstrate the ability of the code in capturing the linear relationship between V_{r2} and V_{t2} documented in Cumpsty [5] as,

$$\frac{V_{t2}}{U_2} = -\sigma \tan \chi_2 (\frac{V_{r2}}{U_2}) + \sigma \tag{2.3}$$

where σ is the ratio of the actual absolute swirl V_{t2} to the idealized case V_{t2i} for which the impeller outflow follows the blade contour up to the trailing edge. Commonly referred as the slip factor, σ can be written as,

$$\sigma = \frac{V_{t2}}{V_{t2i}} \tag{2.4}$$

while χ_2 is the blade backsweep angle at impeller trailing edge. Since V_{t2} is equivalent to the impeller work and V_{r2} is directly related to the mass flow, Equation 2.3 defines the impeller performance characteristic over the operating range.

The best-fit line in Figure 2-2 has a slope $(-\sigma \tan \chi_2) = -1.222$ and an offset $(\sigma) = 0.950$. The backsweep χ_2 can thus be deduced as 52°, confirming the measurements obtained directly from the grid. The best-fit σ also agrees excellently with the Stanitz's correlations for slip factor,

$$\sigma = 1 - \frac{1.98}{N} = 0.948 \tag{2.5}$$

or the Busemann's correlations,

$$\sigma = 1 - \frac{\sqrt{\cos \chi_2}}{N^{0.7}} = 0.939 \tag{2.6}$$

Both Stanitz's and Busemann's correlations can be found in Cumpsty [5]. N is 38 in both cases because there are 19 main blades and 19 splitters in the impeller grid.

Readers may notice that the description of impeller loss is missing in Table 2.1. Direct comparison with measurement is not possible because the measured value of polytropic efficiency η_{poly} is not available. However, the computed value of η_{poly} can be validated against a set of correlations between η_{poly} and N_s (impeller specific speed) documented by Cumpsty [5]. N_s, essentially the non-dimensional ratio of flow coefficient to loading, is defined by,

$$N_s = \frac{\dot{m}^{\frac{1}{2}} \rho_2^{\frac{1}{4}} \Omega}{(p_2 - p_1)^{\frac{3}{4}}} \tag{2.7}$$

with the impeller rotation speed Ω expressed in radian/s. The polytropic efficiency η_{poly} can be deduced from the following relationship,

$$\frac{p_{02}}{p_{01}} = \left[1 + \frac{V_{t2} U_2}{C_{p0} T_{01}}\right]^{\eta_{poly} \frac{\gamma}{\gamma - 1}} \tag{2.8}$$

which is a derived from of Euler turbine equation for impeller flow with no pre-swirl coming into it. Without pre-swirl, the impeller exit tangential velocity also represents the impeller work, $V_{t2}U_2$. The correlation plot from [5] is reproduced in Figure 2-3.

Using the CFD data generated for the validation case, η_{poly} and N_s are computed using Equation 2.7 and 2.8. The results are 90.9% and 0.90 respectively. It can be seen in Figure 2-3 that the newly computed data point falls into the data band of the correlations.

In view of the success of the above validation, it is concluded that the application of the solution algorithm to the present grid resolution represents a good compromise between computational economy and prediction accuracy. Thus, the same level of resolution will be used throughout this investigation.

2.4 Control Numerical Experiment

2.4.1 Influence of Interaction on Impeller Flow

Since the aim of the current project is to investigate the stage performance trend under the influence of stronger interaction, it is important to maintain a control experiment environment to single out the contributing factor to be studied. Thus, to study the effect of downstream condition on the impeller performance, an identical impeller is coupled to three different diffusers to simulate different degrees of interaction. The major difference between these three configurations is the size of the radial gap, or the diffuser leading-edge to impeller trailing-edge ratio ($r_{2'}/r_2$). Respectively, the impeller is coupled to the following three diffusers:

- 1. vaneless with $r_{2'}/r_2 = \infty$, no interaction
- 2. vaned with $r_{2'}/r_2 = 1.092$, intermediate interaction
- 3. vaned with $r_{2'}/r_2 = 1.054$, strong interaction

Other than $r_{2'}/r_2$, all geometrical parameters, such as vane stagger angle, the channel area $A(r)$ of the three diffusers, are kept the same. After a discussion with Marble [28], both the hub and shroud surfaces of the vaneless diffuser are tapered axially to account for the absence of mechanical blockage associated with the vanes. Thus, the second requirement is achieved. It should be noted that the exit radius of the vaneless diffuser has been cut short: $r_3/r_2 = 1.23$; while the value of r_3/r_2 is maintained at 1.46 for the two vaned configurations. Otherwise, the vaneless diffuser tends to have separation, similar to the type observed by Senoo et al. [38], and such separation jeopardizes solution convergence.

The performance from these three configurations at the same impeller speed U_2 and time-averaged mass flow $\dot{m}$ have been compared. Iterations on the exit pressure p_3 were necessary before the target mass flow, a computed output, was obtained for each configuration.

2.4.2 Influence of Interaction on Diffuser Flow

The geometry of the diffuser is kept the same when the effect of upstream condition on its performance is being studied. The full interaction run with $r_{2'}/r_2 = 1.092$ configuration (calculation 2) was chosen as the reference case. In the stationary frame, the rotating impeller outflow can be decomposed into three parts:

- base flow with uniform momentum averaged swirl angle [14] in both axial and circumferential direction (steady)
- axial (hub-to-shroud) distortions (steady)
- unsteadiness, or the circumferential non-uniformity from upstream

It is known that the momentum averaged inlet swirl angle is the most important parameter in setting diffuser pressure recovery [15]. Phillips [33] has found that the influence of axial non-uniformity is negligible compared to that of inlet swirl angle. Thus, the present investigation is designed to isolate out the effect of unsteadiness and compare it to the effect of axial distortions. As explained hereafter, two more steady diffuser-alone calculations (listed in Table 2.2) are needed for isolating the respective effects of unsteadiness and axial distortions.

To do this, the unsteady inlet flow to the diffuser from calculation 2 is time-averaged at each node on the interaction plane to form the boundary condition for the first diffuser-alone steady calculation, designated as calculation 4. Detailed in Appendix A, the time-averaging procedures are conducted by conserving the local mass, angular momentum, and impulse at each of the interaction plane nodes in one period (blade passing). The inlet conditions for calculation 4 thus contain no unsteadiness but have the axial non-uniformity and the circumferential non-uniformity from the downstream vanes retained. The resulting flow field of calculation 4 therefore represents that of calculation 2 with unsteadiness filtered out.

The second diffuser-alone steady calculation is designed to isolate the effect of axial-distortions in the impeller exit flow. The procedures are more subtle because spatial averaging will also eliminate the circumferential non-uniformity from the downstream vanes. Attempts to prescribe uniform boundary conditions at the original diffuser inlet boundary (interaction plane) fail because portion of the flow will then have its incidence mis-aligned with the diffuser vanes, resulting in high loss and jeopardizing diffuser performance. Thus, the inlet boundary of the next calculation (no. 5) has to be moved upstream before a set of uniform boundary conditions (p_0,

T_0, α) can be applied. As seen in Figure 2-4, the inlet boundary of calculation 5 is located at $r/r_2 = 0.82$, about one pitch upstream of the diffuser vane leading edge, while the original inlet boundary is located at the interaction plane ($r_{2+}/r_2 = 1.02$). Iterations on the inlet boundary conditions were required before the following integrated quantities at the original inlet boundary matched those of calculation 2 (after time-averaging).

- mass flow, $\int d\dot{m}$
- angular momentum, $r \int V_t d\dot{m}$
- impulse, $\int pdA + \int V_r d\dot{m}$

Once they are matched, the resulting flow field of calculation 5 is equivalent to that of calculation 2 except that unsteadiness and inlet axial non-uniformity have been filtered out. Table 2.2 outlines the difference between the three calculations in terms of inlet diffuser boundary location.

As designed, the difference between calculations 2 and 4 isolates the effect of unsteadiness, while the difference between calculations 4 and 5 isolates the effect of axial non-uniformity. It should be emphasized that both factors are representative of a typical impeller exit flow, as they are derived directly from the results of calculation 2. Also, all three cases allow the presence of downstream induced circumferential non-uniformity in the interaction region. Retaining such non-uniformity is necessary for the accurate simulation of the diffuser performance.

Time-averaged quantities	Measured	Computed
mass flow $\dot{m}$ (kg/s)	1.77 (target)	1.77
impeller total-to-total pressure ratio p_{02}/p_{01}	6.9	6.6
impeller total-to-static pressure ratio p_2/p_{01}	3.7	3.5
stage total-to-static pressure ratio p_3/p_{01}	5.7	5.5
diffuser pressure recovery coefficient C_p	0.62	0.62
diffuser loss coefficient C_{loss}	0.20	0.19
highest Mach number in diffuser	1.2	1.17

Table 2.1: Comparison of measured and computed performance parameters generated from the 9.2% radial gap configuration

No.	Location	Unsteadiness	Axial non-uniformity	Circumf. non-u. from upstream	Circumf. non-u. from downstream
2	Interaction plane	Present (from impeller)	Present	Present	Present
4	same as no. 2	Absent	Present	Absent	Present
5	Moved upstream	Absent	Absent	Absent	Present (negligible)

Table 2.2: Comparison of diffuser inlet conditions for calculation 2, 4, 5

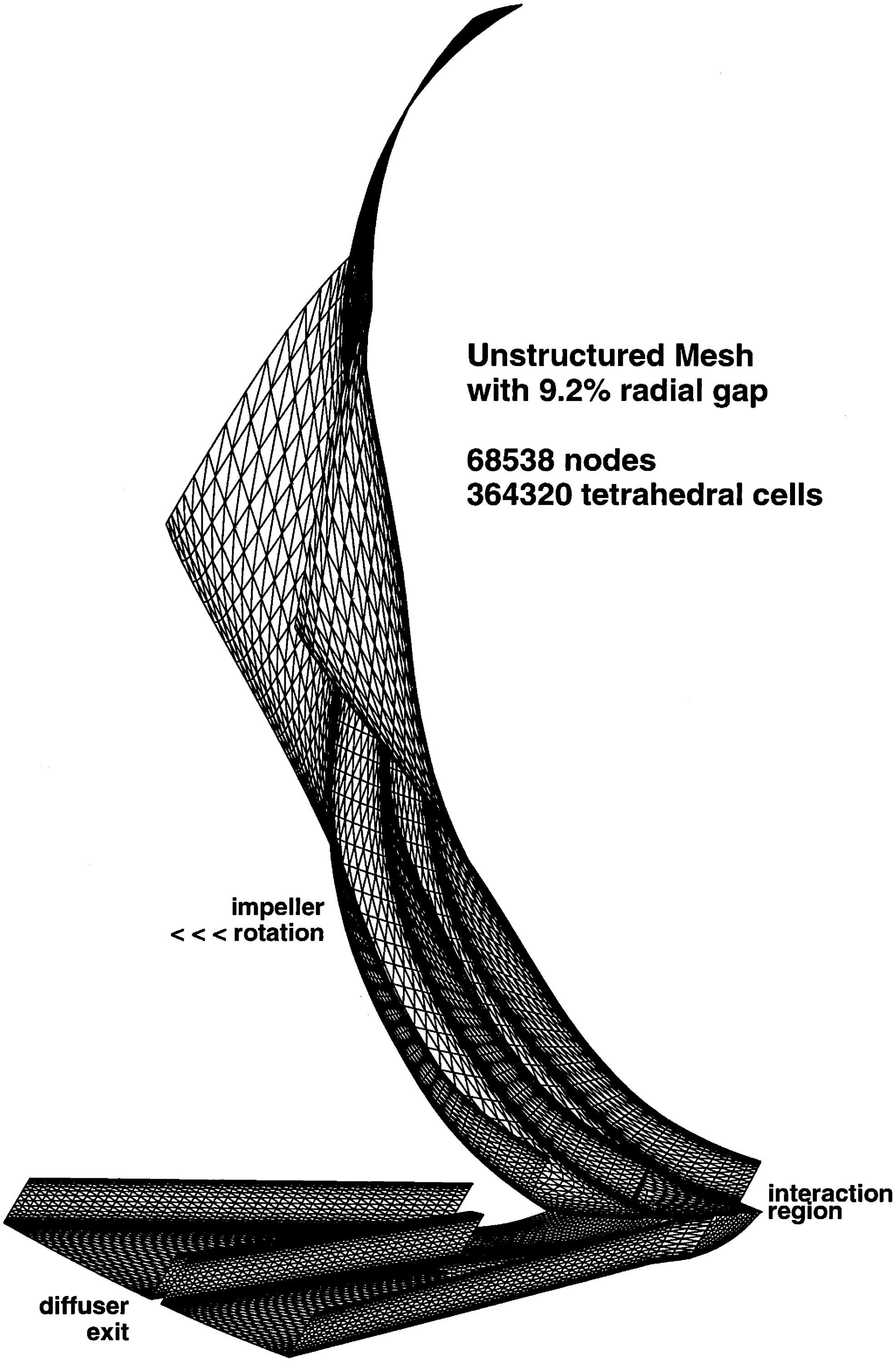
Unstructured Mesh
with 9.2% radial gap
68538 nodes
364320 tetrahedral cells
impeller
< < < rotation
interaction
region
diffuser
exit

Figure 2-1: The unstructured mesh used for the $r_{2'}/r_2 = 1.092$ configuration with the casings of both impeller and diffuser removed

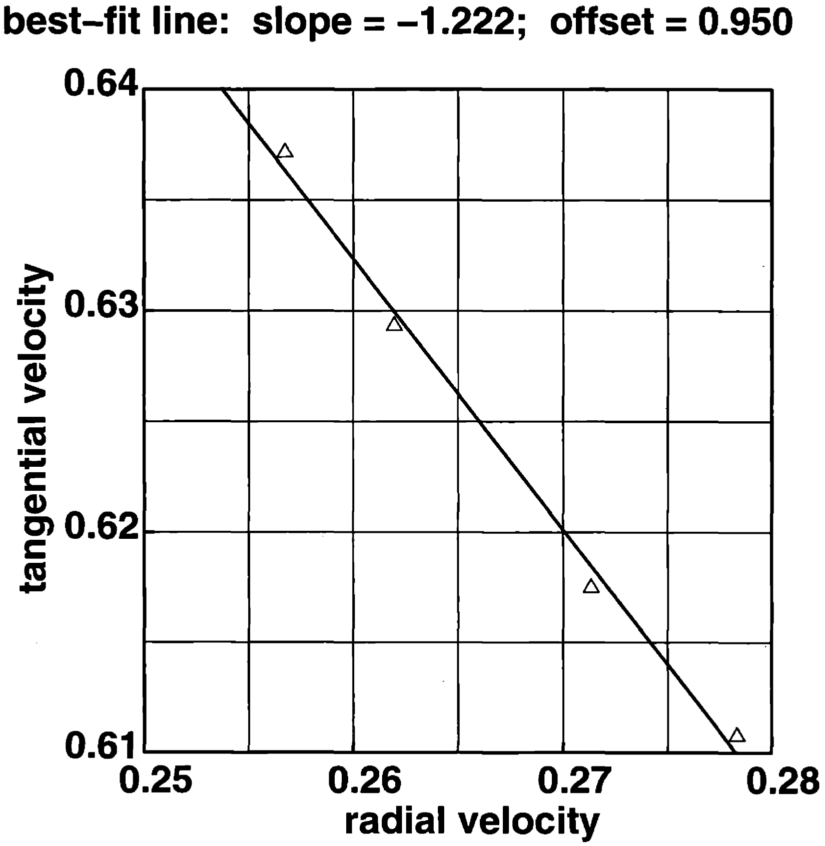

Figure 2-2: The relationship between radial velocity V_{r2} and tangential velocity V_{t2} at impeller exit for the 9.2% radial gap configuration, both speeds non-dimensionalized by U_2

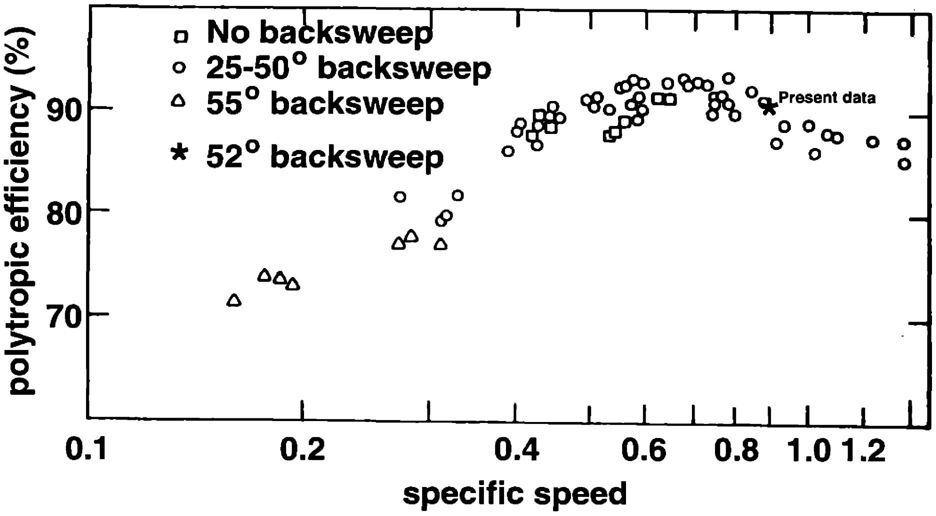

Figure 2-3: Correlations between polytropic efficiency η_{poly} and specific speed N_s reproduced from [5], with the present data point added

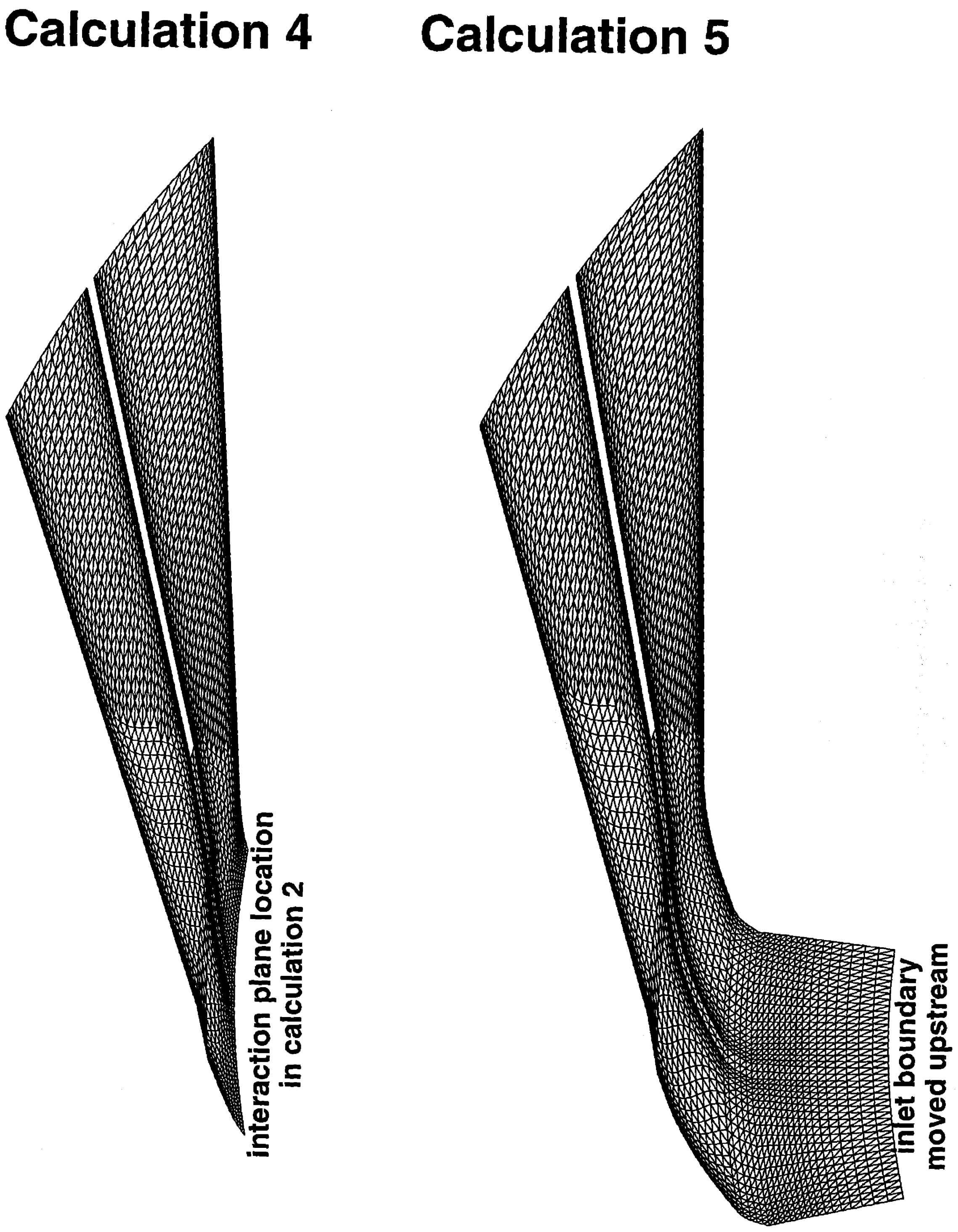
Calculation 4

Calculation 5

interaction plane location
in calculation 2
inlet boundary
moved upstream

Figure 2-4: Comparison of respective grid for diffuser calculations 4 and 5

CHAPTER 3

INFLUENCE OF INTERACTION ON IMPELLER FLOW

3.1 Introduction

This chapter presents qualitative and quantitative descriptions of the flow in the impeller with different degrees of interaction. These are obtained by varying the radial gap size $r_{2'}/r_2$, which is the only control variable in this numerical experiment. The procedures for the control study were discussed in section 2.4.

Rodgers' [37] experimental study on how the effect of $r_{2'}/r_2$ influences performance has a similar approach to the current one. His results, reproduced from [37], are summarized in Figure 3-1. It can be seen in Figure 3-1 that the configuration with the strongest interaction ($r_{2'}/r_2 = 1.035$) actually has inferior impeller performance compared to the configuration with a wider radial gap ($r_{2'}/r_2 = 1.125$). Impeller total pressure ratio p_{02}/p_{01} is 5.3 vs. 5.5, while the isentropic efficiency η_{isen} is 0.76 vs. 0.78. Widening the radial gap from $r_{2'}/r_2 = 1.125$ to 1.180 results in a drop of performance in terms of both p_{02}/p_{01} and η_{isen}, though they are still higher than their counterparts in the $r_{2'}/r_2 = 1.035$ case. The widest gap configuration with $r_{2'}/r_2 = 1.215$ produces the worst impeller performance. In summary, Rodgers demonstrates experimentally that there exists an optimum radial gap size for impeller performance. In other words, impeller-diffuser interaction contributes positively to impeller performance unless the two components are placed too close. No explanation was provided in the reference. A goal of this investigation is to verify Rodgers' observation by applying CFD to a stage of recent industry design, and then explain why such changes occur when the radial gap size is varied.

3.2 Numerical Results

Calculations 1, 2, 3 are carried out according to the procedures in Section 2.4 and the results (p_{02}/p_{01} vs. $\dot{m}$) are plotted in Figure 3-2. As seen in Figure 3-2, a perfect match for the resulting mass flow $\dot{m}$ between all three configurations cannot be achieved, because $\dot{m}$ is the end-product of a calculation. Limitation of resources does not allow too many runs for the searching of perfect match. Nevertheless, the variance of $\dot{m}$ in the three cases is within 1% of the reference value, considerably smaller than the operating range of any well-designed machine.

There was concern on whether the different pressure ratio p_{02}/p_{01} observed in the three cases was due to the slight mismatch of mass flow. To verify that sensitivity to $\dot{m}$ is not the major factor in the difference observed in the pressure rise characteristic for the $r_{2'}/r_2 = 1.092$ case was established using the data collected from various runs of this configuration, each prescribed with a different diffuser exit pressure p_3. The characteristic is obtained in Figure 3-2 as the best-fit line of the $r_{2'}/r_2 = 1.092$ data points. The two data points respectively from the vaneless and $r_{2'}/r_2 = 1.054$ are not close to the $r_{2'}/r_2 = 1.092$ characteristic, demonstrating that radial gap size can indeed influence the impeller total pressure ratio. In other words, impeller-diffuser interaction severity is identified as the major contributor to the performance change.

The performance parameters of the three calculations are tabulated in Table 3.1 for comparison. The most significant aspect of the results is that they echo Rodgers' observation; placing the two components closer does not necessarily result in higher impeller pressure ratio. As shown in Table 3.1, the highest pressure ratio $p_{02}/p_{01} = 6.63$ is produced by the $r_{2'}/r_2 = 1.092$ configuration which has intermediate interaction severity, higher than p_{02}/p_{01} in the vaneless configuration by more than 3%. Closing the radial gap from $r_{2'}/r_2 = 1.092$ down to 1.054 causes p_{02}/p_{01} to drop to 6.51. Similar "turn-around" behavior is also observed on the isentropic efficiency η_{poly}, which is evaluated using Equation 2.8.

The efficiency for the strong interaction case is lower than that of the medium interaction case by close to a percentage point, while the impeller work (represented by the exit tangential velocity V_{t2}) is roughly equal for the two vaned cases ($V_{t2}/U_2 =$ 0.628 vs. 0.629). What contributes to the change in both circulation and loss will become the focus of further investigation.

With the performance difference between the three configurations identified, the next question to answer is where the difference originates. Figure 3-3 shows the total pressure ratio p_0/p_{02}, mass and time averaged at each meridional station, for the three configurations. Noticeable differences only arise at the last 10% of the impeller passage near the blade trailing edge. This region, denoted by the circle in Figure 3-3, is within one pitch distance upstream of the diffuser vane leading edge. It therefore should be influenced by the potential field of the diffuser vanes. With $r_{2'}/r_2$ acting as the only control variable in the comparison, Figure 3-3 provides evidence that impeller-diffuser interaction induces the observed performance change in the impeller.

The direct consequence of the potential effect from the diffuser vanes is the introduction of unsteadiness into the impeller flow field because relative to the impeller, the pressure field associated with downstream vanes is rotating. Figure 3-4 plots the instantaneous static pressure along the impeller passage centerline for the $r_{2'}/r_2 = 1.092$ configuration, as the static pressure gradient is the driving force for the flow field. The data are obtained at 8 different instants of one period (one blade passing) with equal time interval separating them, so each line in Figure 3-4 is a snap-shot of the meridional distribution of static pressure. Again, only in the last 10% of the impeller passage the pressure field undergoes large changes, in the form of unsteadiness.

The above observation is summarized in Figure 3-5 where the rms time fluctuation of static pressure along the same path is plotted. The fluctuation drops from roughly 5% of the impeller exit dynamic pressure $(p_{02} - p_2)$ to about 0.5% at 90% meridional distance and is essentially negligible upstream of the 80% meridional station. Figure 3-4 and Figure 3-5 strongly indicate, though not conclusively, that unsteadiness induced by interaction is responsible for the observed change of impeller performance. Lacking yet is the flow mechanism(s) which links the unsteady pressure field to the performance change. The investigation of such flow mechanism(s) is the main subject of the next section.

3.3 Explanation of Observations

The aim of this section is to show that one-dimensional flow models (documented in Section 3.3.1 - 3.3.2) can describe the change in the impeller total and static pressure ratio as a result of diffuser vanes being placed closer to the impeller. The model also allows the identification of the major contributors to the change in impeller performance. The flow mechanism(s) which leads to the contributors can then be traced by applying flow visualization on the computed data, as described in Section 3.3.3.

3.3.1 One-Dimensional Model of Impeller Total Pressure Ratio

To explain why impeller total pressure ratio p_{02}/p_{01}, changes with the addition of diffuser vanes downstream, it is convenient from here on to express the pressure ratio and loss relationship in terms of entropy s. Equation 2.8, the modified Euler turbine equation which expresses loss in the relative term η_{poly}, is thus rewritten as,

$$\frac{p_{02}}{p_{01}} = \left[1 + \frac{V_{t2}U_2}{C_{p0}T_{01}}\right]^{\frac{\gamma}{\gamma-1}} \mathrm{e}^{-(s_2-s_1)/R} \tag{3.1}$$

The advantage of using Equation 3.1 instead of Equation 2.8 is that both of the two independent variables in Equation 2.8, V_{t2} and s_2, can be obtained directly from the computed flow data after mass and time averaging. Linearization of Equation 3.1 isolates the effect of these two independent variables on Δp_{02} as:

$$\frac{\Delta p_{02}}{p_{02}} = \left[\left(\frac{\gamma}{\gamma-1}\right)\left(\frac{V_{t2}U_2}{C_{p0}T_{01}+V_{t2}U_2}\right)\right]\frac{\Delta V_{t2}}{V_{t2}} - \left[\frac{\gamma}{\gamma-1}\right]\frac{\Delta s_2}{C_{p0}} \tag{3.2}$$

where Δ is used to denote the incremental change of flow quantities from those of vaneless configuration.

However, V_{t2} is not the most fundamentally independent variable because it depends on the channel velocity W_2 in the relative frame, and the dependence of V_{t2} can be illustrated more clearly using the velocity triangle in Figure 3-6. The main message from Figure 3-6 is that the flow does not follow the blade contour (backsweep angle χ_2 in Figure 3-6) completely. Thus, the actual tangential velocity V_{t2} differs from that based on blade backsweep angle by a slip velocity V_s. V_s itself is predominantly a result of inviscid effect [5], which depends largely on the circumferential spacing of the impeller blades. Since the impeller geometry has not been changed in this control experiment, the incremental change of V_s can only be attributed to the presence of the downstream vanes. Furthermore, this implies that impeller-diffuser interaction can also affect the channel velocity W_2 via its influence on V_s.

The description of this relationship is made somewhat simpler by employing θ, the angle between the radial direction and the exit flow direction in the relative frame, instead of V_s as the independent variable; and the relationship is,

$$V_{t2} = U_2 - W_2 \sin\theta \tag{3.3}$$

Equation 3.3 can be linearized into the following form,

$$\frac{\Delta V_{t2}}{V_{t2}} = \left[\frac{-(U_2 - V_{t2})}{V_{t2}}\right] \frac{\Delta W_2}{W_2} + \left[\frac{1}{\tan\alpha}\right](-\Delta\theta) \tag{3.4}$$

The negative sign preceding θ in Equation 3.4 signifies that a smaller θ implies reduced slip, which is beneficial to impeller pressure ratio.

How W_2 responds to change in the local flow condition can be derived using one-dimensional flow conservation equations expressed in incremental form as in Shapiro [40]. Details of the development are outlined in Appendix B and the resulting relationship is,

$$\frac{\Delta W_2}{W_2} = \left[\frac{-1}{1 - M_{rel,2}^2}\right] \frac{\Delta A_{eff}}{A_{eff}} + \left[\left(\frac{\gamma}{\gamma - 1}\right)\left(\frac{1}{1 - M_{rel,2}^2}\right)\right] \frac{\Delta s_2}{C_{p0}} \tag{3.5}$$

where $M_{rel,2}$ is the relative Mach number of the impeller passage flow evaluated in the frame of the impeller, and A_{eff} is the effective flow passage area, which is the geometrical passage area minus the flow blockage. The non-dimensional blockage B is related to A_{eff} [2] by,

$$1 - B = \frac{A_{eff}}{A_{actual}} \tag{3.6}$$

Khalid et al. [24] provides step-by-step procedures to evaluate B for steady flow in axial machines. The adjustment to these procedures so that they can be adopted for this investigation is described in Appendix C.

With some algebraic manipulation, Equations 3.2, 3.4, 3.5 can be consolidated into a single expression by eliminating the dependence on ΔW_2 and ΔV_{t2}. This establishes the relationship between the change in impeller total pressure ratio and the three independent incremental changes which completely represent the influence of impeller-diffuser interaction: ΔA_{eff}, Δs_2, $-\Delta\theta$. The expressions for this relationship are,

---

[2] A_{eff} has a weak dependence on θ but the approximation in Equation 3.6 is adopted in the current model for simplicity.

$$\frac{\Delta p_{02}}{p_{02}} = C_A\left(\frac{\Delta A_{eff}}{A_{eff}}\right) + C_s\left(\frac{\Delta s_2}{C_{p0}}\right) + C_\theta\left(-\Delta\theta\right) \tag{3.7}$$

where C_A, C_s, and C_θ are the influence coefficients of the three independent incremental changes stated above, defined by,

$$C_A = \left(\frac{U_2 - V_{t2}}{V_{t2}}\right)\left(\frac{1}{1 - M_{rel,2}^2}\right)\left(\frac{\gamma}{\gamma - 1}\right)\left(\frac{V_{t2}U_2}{C_{p0}T_{01} + V_{t2}U_2}\right) > 0 \tag{3.8}$$

$$C_s = -\left(1 + C_A\right)\left(\frac{\gamma}{\gamma - 1}\right) < 0 \tag{3.9}$$

$$C_\theta = \left(\frac{1}{\tan\alpha}\right)\left(\frac{\gamma}{\gamma - 1}\right)\left(\frac{V_{t2}U_2}{C_{p0}T_{01} + V_{t2}U_2}\right) > 0 \tag{3.10}$$

The sign convention of the influence coefficients in Equations 3.8 to 3.10 is defined by assuming both quantities $(U_2 - Vt2)$ and θ are positive, which is true for any impeller with backsweep. Substituting Equations 3.8 to 3.10 into Equation 3.7 reveals that a positive influence coefficient (C_A, C_θ) implies a positive contribution to impeller pressure ratio, while the negative one (C_s) implies the opposite. In summary, higher impeller total-to-total pressure ratio can be achieved by any of the followings:

- More effective area ⟶ Reduced blockage
- Reduced loss
- Reduced slip.

The three independent incremental changes are evaluated from the computations by mass and time averaging at the impeller exit, and the results are summarized in Table 3.2. It can be seen that placing the diffuser vanes closer to the impeller reduces both blockage ($A_{eff} \uparrow$) and slip ($\theta \downarrow$), but increases loss ($s_2 \uparrow$). The incremental impeller total pressure ratio $\Delta p_{02}/p_{02}$ can thus be estimated by substituting these changes into Equation 3.7. The comparison between the one-dimensional estimation (1-D, Equation 3.7) and the computed value (3-D) of $\Delta p_{02}/p_{02}$, obtained directly from the three dimensional unsteady flow data after mass and time averaging, is shown in Figure 3-7 a. It can be seen that the correspondence between the 1-D estimates and the 3-D computed results is good, and the "turn-around" behavior of the total pressure ratio with reducing radial gap size is in agreement with the 1-D model. Table 3.3 outlines the individual contribution of each of the independent factors which affects impeller total pressure ratio. The comparison reveals that the "turn-around" behavior is caused by the rapid increase in loss, which overtakes the other two incremental changes beneficial to pressure ratio.

3.3.2 One-Dimensional Model on Impeller Static Pressure Ratio

In addition to impeller total-to-total pressure ratio, attention should also be paid to the effect of interaction on total-to-static pressure ratio. The reason is that both pressure ratios (p_{02}/p_{01}, p_2/p_{01}) contribute to the stage pressure ratio p_3/p_{01}, which is the most important performance parameter of a centrifugal machine. The relationship can be written as,

$$\frac{p_3}{p_{01}} = C_p \frac{p_{02}}{p_{01}} + (1 - C_p)\frac{p_2}{p_{01}} \tag{3.11}$$

which is a rearranged form of the diffuser pressure recovery definition in Equation 2.1:

$$C_p = \frac{p_3 - p_2}{p_{02} - p_2}$$

Similar to the development for Δp_{02}, the alteration in impeller static pressure Δp_2 due to the interaction-induced incremental changes can also be evaluated using the one-dimensional approach. In fact, the development is much simpler because the evaluation can be conducted solely in the impeller frame as static pressure is a frame-independent thermodynamic variable. Thus the resulting relationship can be obtained by selecting the corresponding terms in Shapiro's [40] influence coefficient table. The complete expression is,

$$\frac{\Delta p_2}{p_2} = C_{\tilde{A}} \left(\frac{\Delta A_{eff}}{A_{eff}} \right) + C_{\tilde{s}} \left(\frac{\Delta s_2}{C_{p0}} \right) \tag{3.12}$$

where $C_{\tilde{A}}$ and $C_{\tilde{s}}$ are the influence coefficients defined as

$$C_{\tilde{A}} = \frac{\gamma M_{rel,2}^2}{1 - M_{rel,2}^2} > 0 \tag{3.13}$$

$$C_{\tilde{s}} = -\left(1 + C_{\tilde{A}}\right) \left(\frac{\gamma}{\gamma - 1} \right) < 0 \tag{3.14}$$

The main difference between Equation 3.12 and its total pressure counterpart, Equation 3.7, is the absence of the slip term involving $\Delta\theta$. Frame-independency of static pressure is the reason for the difference. The similarity between C_s in Equation 3.9 and $C_{\tilde{s}}$ in Equation 3.14 reflects that entropy production counteracts effective area in generating higher static or stagnation pressure. The sign convention in Equation 3.13 and 3.14 is defined by assuming subsonic impeller flow with $M_{rel} < 1$, a common practice because choking in the impeller passage should be avoided.

As in the procedure for $\Delta p_{02}/p_{02}$, the comparison between the one-dimensional estimation (1-D, Equation 3.12) and the computed value (3-D) of $\Delta p_2/p_2$ is shown in Figure 3-7 b. Again, the correspondence between the 1-D estimates and the 3-D computed results is good, and the "turn-around" trend of the static pressure ratio with varying radial gap size is captured by the one-dimensional model.

In summary, the one-dimensional model for estimating Δp_{02} and Δp_2 helps identify the interaction-induced change in three independent factors (blockage, loss, and slip) responsible for the incremental change in impeller pressure ratio. The model is in agreement with the computed "turn-around" behavior of pressure ratio when radial gap size is varied. According to Equation 3.11, understanding the interaction-induced change in p_{02} and p_2 addresses the entire upstream contribution to stage pressure ratio. The investigation of the interaction effects on stage performance will be completed by the study on the downstream change, namely C_p, which will be presented in the next chapter.

3.3.3 Flow Visualization on Computed Flow Field

The focus now is shifted towards the reason for the observed change in the three independent factors. The investigation can only be conducted by flow visualization on the computed unsteady three-dimensional flow field. The first quantity we look at is the loss production in the impeller because it has a direct influence on pressure ratio. The loss in an unsteady flow can be measured by the entropy [6], whose unsteady transport equation takes the following form for adiabatic flow:

$$\rho\frac{Ds}{Dt} = \frac{1}{T}\tau_{ij}\frac{\partial V_i}{\partial x_j} + \frac{k_e}{T^2}\frac{\partial T}{\partial x_i}\frac{\partial T}{\partial x_i} \tag{3.15}$$

where τ_{ij} the stress tensor, V_i the velocity vector, x_i the spatial coordinate and k_e the thermal conductivity. The right hand side of Equation 3.15 describes the source of entropy production due to viscous dissipation and heat transfer respectively; while the left hand side represents the unsteady convection of the entropy flux.

By applying Equation 3.15 to the flow data, the local volumetric entropy production rate $\rho\frac{Ds}{Dt}$ (unit: $\frac{\mathrm{J}}{\mathrm{K.s.m^3}}$) can be evaluated. This quantity provides immediate identification of the high loss region. The $\rho\frac{Ds}{Dt}$ contours on the transverse plane at the impeller trailing edge for the vaneless configuration are plotted in Figure 3-8. These show that the majority of the entropy generation occurs near the shroud, especially at the tip leakage exit region.

Figures 3-9 to 3-16 plot $\rho\frac{Ds}{Dt}$ contours at the same impeller location as in Figure 3-8, but they are generated from the $r_{2'}/r_2 = 1.092$ configuration. Each of the plots is obtained at an instant with equal time interval of one-eighth of a blade passing in between . Besides showing that loss again originates mostly at the tip leakage region, this series of plots also demonstrate the unsteady nature of the loss generation associated with this region. For the main blade tip leakage, the entropy production contours are noticeably denser at $t = \frac{6}{8}, \frac{7}{8}T$ compared to those obtained half a period apart at $t = \frac{2}{8}, \frac{3}{8}T$. The same description can be applied to the splitter tip leakage with the corresponding time shifted by half a blade passing. Loss generation is thus a periodic process with a frequency of blade passing. However, a more important question to an engineer is that whether this unsteady phenomenon can cause a change in the time-averaged loss at the impeller exit.

This question can be answered directly by comparing the time averaged entropy production for the vaneless and the vaned cases, i.e. plotting the incremental change of entropy production from the vaneless configuration $\Delta(\rho\frac{Ds}{Dt})$. The comparison is done for both $r_{2'}/r_2 = 1.054$ and 1.092 configurations which are plotted in Figure 3-17. The $\Delta(\rho\frac{Ds}{Dt})$ contours have been non-dimensionalized against the volume averaged entropy production in the vaneless configuration to quantify the effect of downstream vanes. Figure 3-17 shows that significantly higher incremental loss, by more than 100 times, is generated at the exit of the tip leakage flow when comparing the two vaned cases to the vaneless configuration. In addition, the smaller the radial gap, the higher the loss, confirms that the loss generation at the tip leakage exit is related to the flow unsteadiness in the region.

There is a possibility that the higher loss observed in the shroud region of the vaned configurations is due to an increased tip leakage mass flow induced by interaction. To find out if there is an increase in the amount of tip leakage mass flow when vanes are placed downstream, and more importantly, if such increase is indeed significant to affect impeller performance, the time-averaged accumulated amount of tip leakage mass flow ($\dot{m}_{tip}/\dot{m}$ after non-dimensionalizing) is compared for the three radial gaps in Figure 3-18. It can be seen that $\dot{m}_{tip}/\dot{m}$ has a predominately linear distribution along the impeller passage for both main blade and splitter. Similar results have been reported by Moore et.al. [31]. As expected, difference between the three configurations can only be found in the last 15% of the impeller passage, a result of the local change in blade loading induced by impeller-diffuser interaction (see Figure 3-3). Comparing the time-averaged accumulated tip leakage mass flow between the three cases ($\Delta\dot{m}_{tip,2}/\dot{m} = +0.2\%$ in Table 3.4) reveals that the change is too small to account for the incremental change in loss at the impeller exit ($\Delta s_2/s_2 = +5.0\%$ in Table 3.2).

By ruling out the effect of the time-averaged $\Delta\dot{m}_{tip,2}$, investigation can be concentrated on the unsteady aspects of the tip leakage flow. The quantity to be studied is the instantaneous tip leakage mass flux ρW_{tip} in which W_{tip} is the tip leakage jet velocity in the rotation frame. The fluctuation of W_{tip} is closely related to the tip region velocity gradient which determines the local viscous dissipation. Figure 3-19 compares the non-dimensional instantaneous main blade tip leakage mass flux $\frac{\rho W_{tip}}{\rho_2 U_2}$ for the three gaps at the 90%, 95%, 99% meridional stations. Only minor unsteadiness can be observed for the vaned cases at the 90% meridional station, but periodicity of the tip leakage is apparent at the 95% meridional station. At the 99% meridional station, the tip leakage mass flux for the vaned cases is so unsteady that the peak-to-peak amplitude of the mass flux is roughly equal to its time-averaged value.

It is expected that a smaller radial gap causes more unsteadiness to the flow field near the impeller exit and this shows up in the tip leakage flow as well. As seen in Figure 3-19, at the 99% meridional station the $r_{2'}/r_2 = 1.054$ configuration has a peak-to-peak variation of 0.247 for the quantity $\frac{\rho W_{tip}}{\rho_2 U_2}$, while the $r_{2'}/r_2 = 1.092$ configuration has a value of 0.198. The time-averaged value of $\frac{\rho W_{tip}}{\rho_2 U_2}$ at this location ranges from 0.231 to 0.244 for all three cases. The behavior of the splitter tip leakage flow is similar to that of the main blade and all the qualitative description of Figure 3-19 can be applied to Figure 3-20, with the peak of the variation shifted by half a blade passing.

For both the vaneless (Figure 3-8) and the vaned (Fig 3-9 to 3-16) configurations, the high dissipation observed near the shroud region is caused by a high velocity gradient associated with the cross flow between tip leakage flow and the main stream flow. For the vaned configurations, the tip leakage mass flux ρW_{tip} time variation comes mostly from the jet velocity W_{tip} variation because the tip leakage flow can be considered as incompressible as the corresponding Mach number is about 0.5. Therefore, the substantial unsteadiness in ρW_{tip} (Figure 3-19 and 3-20) should lead to an additional instantaneous tangential velocity gradient at the tip leakage region. The result is an increased rate of viscous dissipation, which is also confirmed by the entropy production rate plot shown in Figure 3-17.

To complete the investigation, the blade loading $\frac{p_{ps}-p_{ss}}{p_{02}-p_2}$ for both the main blade and splitter are respectively plotted in Figure 3-21 and 3-22. The comparison of the three configurations are conducted at the same meridional stations as above (90%, 95%, 99%). It can be seen that the tip leakage mass flux (Figure 3-19 and 3-20) are synchronized with the corresponding blade tip loading in terms of the occurrence of the peak and trough, confirming that the unsteady pressure difference set up by the downstream vanes is the driving force of the unsteady tip leakage flow. The observation that instantaneous blade tip loading and tip leakage mass flux is in phase indicates the tip leakage flow is quasi-steady. This can be confirmed by calculating the reduced frequency β for the tip leakage flow:

$$\beta = \frac{(N\Omega)(b)}{W_{tip}} = \frac{b/pitch}{W_{tip}/U_2} \qquad (3.16)$$

where b is the blade thickness and Ω is the impeller rotation speed expressed in radian/s. For the $r_{2'}/r_2 = 1.092$ configuration, β is evaluated to be $0.13 \ll 1$ at the 95% meridional station, explaining why tip leakage flow is quasi-steady and so unsteadiness has little effect on the quantity of tip leakage flow.

Besides increasing loss, the higher viscous dissipation in the vaned cases can influence blockage. This can be demonstrated by Figure 3-23 to 3-25 in which the time-averaged entropy rise $\frac{s-s_1}{C_p}$ of the three radial gap sizes are plotted. At the 90% meridional stations (Figure 3-23), the $\frac{s-s_1}{C_p}$ contours for all three configurations look similar. However, at the 95% meridional station (Figure 3-24), it becomes apparent that increased viscous dissipation near the tip leakage exit helps reduce the amount of high-loss fluid flowing across the the pitch. This is demonstrated by the lower value of entropy rise $s - s_1$ associated with the fluid collected at the casing-suction side corner. This trend continues as the flow approaches the blade trailing edge in Figure 3-25. The trailing edge plot also reveals that the $\frac{s-s_1}{C_p}$ contours are denser for the vaneless case, even in the main stream region. The findings are similar to those obtained by Graf [16] who concludes that closer coupling between the rotor and stator in an axial machine can help improve the endwall flow field in both loss and blockage, in the expense of more rotor profile loss and stator loss away from the tip region. As a result, the overall effective flow area A_{eff} is increased at the impeller exit.

The following summarizes the cause and effect for the increased viscous dissipation:

- Loading unsteadiness $\uparrow$
- Instantaneous pressure gradient across tip clearance $\uparrow$
- Tip leakage mass flux unsteadiness $\uparrow$
- Instantaneous velocity gradient $\uparrow$
- Time-averaged viscous dissipation $\uparrow$
- Time-averaged loss $\uparrow$

- Time-averaged flow blockage ↓

With the effect of unsteadiness on loss (Δs_2) and blockage (ΔA_{eff}) addressed, the only remaining factor is slip, which is expressed in terms of the swirl angle incremental change ($\Delta\theta$). Although slip is largely dependent on the impeller blade spacing [5], which is kept identical in the current study, flow separation can also change the impeller exit flow angle. However, the mass flux at the impeller exit plot (Figure 3-26) indicates that little separation occurs near the shroud for all three configurations, leaving the inviscid effect from the vanes as the primary factor for the incremental change in slip ($\Delta\theta$ listed in Table 3.2).

3.4 Summary

Results from the current numerical simulation are in agreement with Rodgers' [37] experimental findings that there is an optimum impeller-diffuser gap size for achieving the highest pressure ratio in the impeller. However, the flow descriptions obtained from the computation needs further analysis and organization to clarify the responsible mechanisms. Thus a one-dimensional model has been developed to help identify the factors which affect the impeller pressure ratio when the radial gap size between the impeller and diffuser is varied. The model can also be applied for preliminary performance evaluation.

It is inferred from the computed results that there are three factors detrimental to impeller pressure ratio. All of them can be affected by varying the impeller-diffuser coupling. Respectively they are:

- Loss
- Blockage
- Slip

All three are responsible for lowering impeller total pressure ratio while only the first two are related to the static pressure ratio.

Increased coupling between the impeller and diffuser creates a more unsteady flow field in the last 10% of the impeller passage. The resulting higher velocity gradients lead to higher viscous dissipation which:

- Increase loss
- Decrease blockage

The effect is particularly strong in the shroud region because the cross flow between the unsteady tip leakage flow and the main stream flow produces the highest velocity gradient. Increased coupling also reduces the slip of the impeller exit flow due to the inviscid effect of the closer diffuser vanes.

Altogether, coupling can be beneficial to impeller pressure ratio because of the reduced blockage and slip, provided the impeller and diffuser are not too closely placed so that loss overtakes the other two benefits.

Interaction	no	medium	strong
radius ratio $r_{2'}/r_2$	∞	1.092	1.054
mass flow $\dot{m}$ (% of reference value)	100.8	100.0	99.8
impeller total-to-total pressure ratio p_{02}/p_{01}	6.43	6.63	6.51
impeller total-to-static pressure ratio p_2/p_{01}	3.49	3.54	3.46
tangential velocity V_{t2}/U_2	0.618	0.629	0.628
polytropic efficiency η_{poly} (in %)	90.6	90.9	90.2

Table 3.1: Comparison of computed impeller performance parameters from different radial gap size ($r_{2'}/r_2$)

Interaction	no	medium	strong
blockage B_2	0.1353	0.1263	0.1241
$\frac{\Delta A_{eff}}{A_{eff}}$		+1.04%	+1.30%
entropy $\frac{T_2(s_2-s_1)}{U_2 V_{t2}}$	0.1038	0.1010	0.1088
$\frac{\Delta s_2}{C_{p0}}$		-0.0006	+0.0035
slip θ	55.7°	54.8°	54.2°
$\Delta\theta$ (radian)		-0.0164	-0.0255

Table 3.2: Incremental changes of independent variables in the impeller flow field due to vanes being placed downstream

individual factors	medium interaction	strong interaction
reduced blockage	+1.80%	+2.21%
increased loss	+0.53%	-3.32%
reduced slip	+1.08%	+1.67%
Σ	+3.41%	+0.56%

Table 3.3: Relative importance of independent factors for impeller total pressure ratio

Interaction	no	medium	strong
radius ratio $r_{2'}/r_2$	∞	1.092	1.054
main blade	3.6	3.6	3.7
splitter	2.1	2.1	2.1
Σ: total $\frac{\dot{m}_{tip,2}}{\dot{m}}$	5.6	5.7	5.8

Table 3.4: Comparison of accumulated tip leakage mass flow at impeller trailing edge for different radial gap size

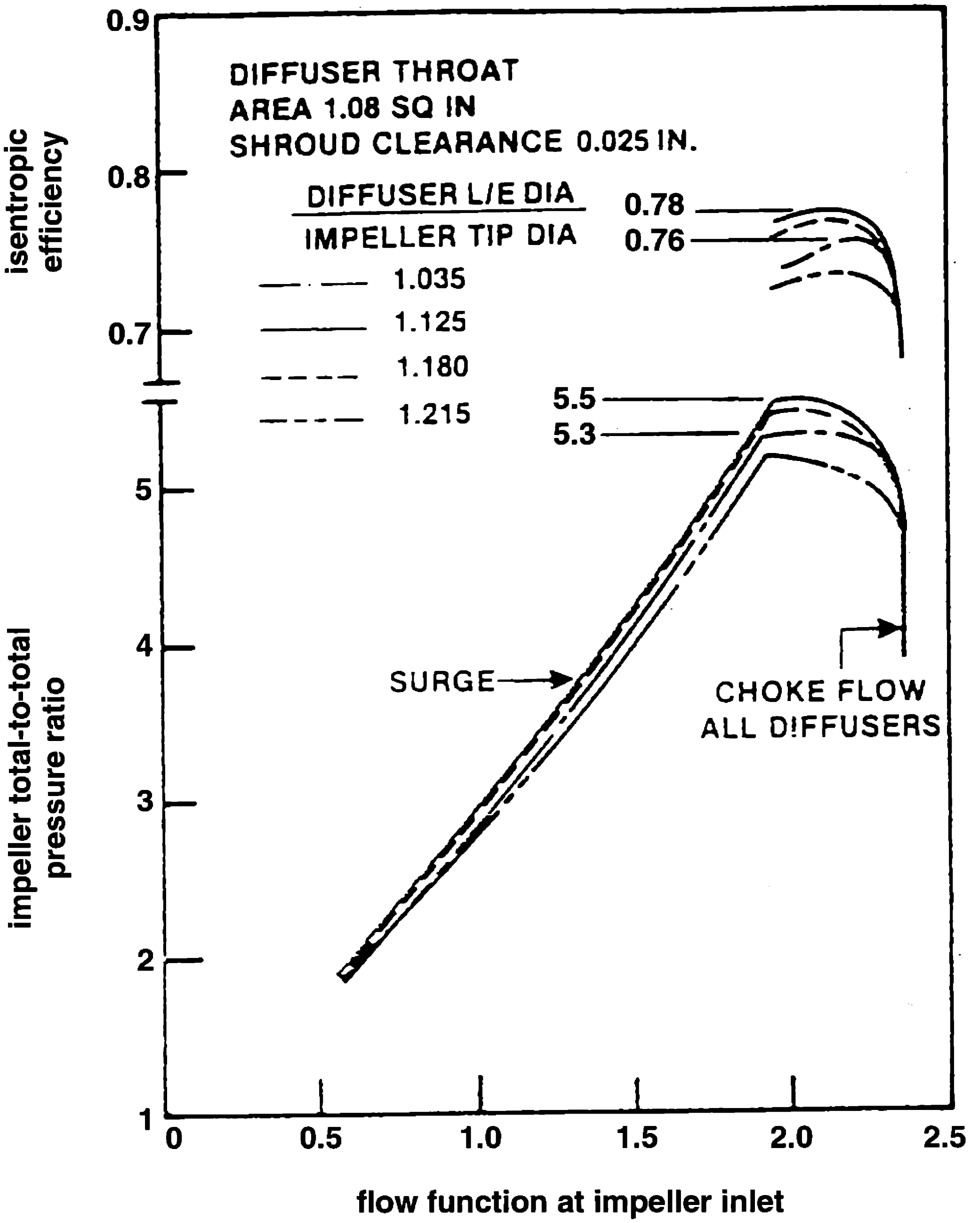

Figure 3-1: Effect of radial gap size $r_{2'}/r_2$ on impeller performance, reproduced from [37]

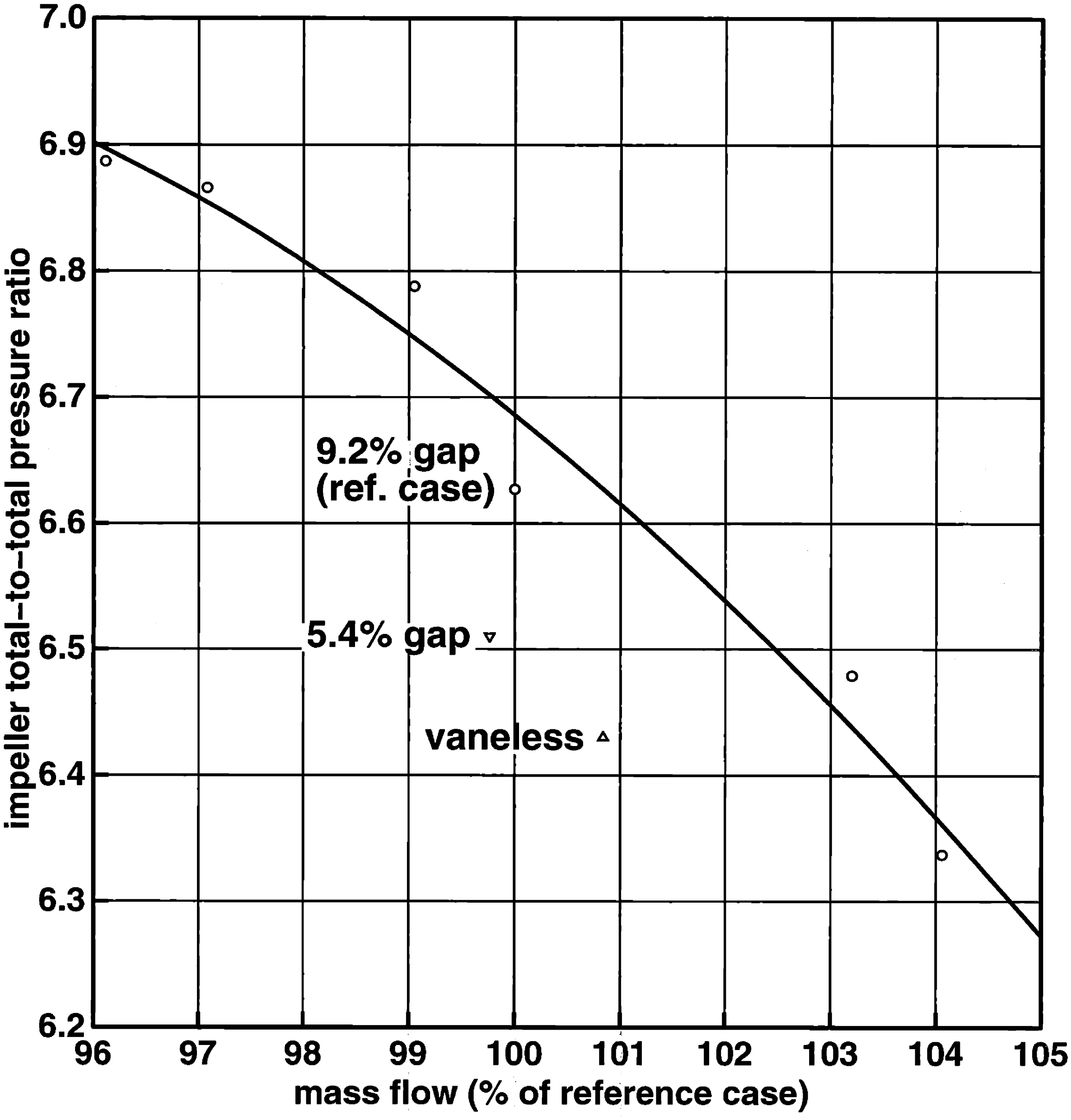

Figure 3-2: Impeller total-to-total pressure for the three different radial gap sizes, with the complete characteristic of $r_{2'}/r_2 = 1.092$ case shown

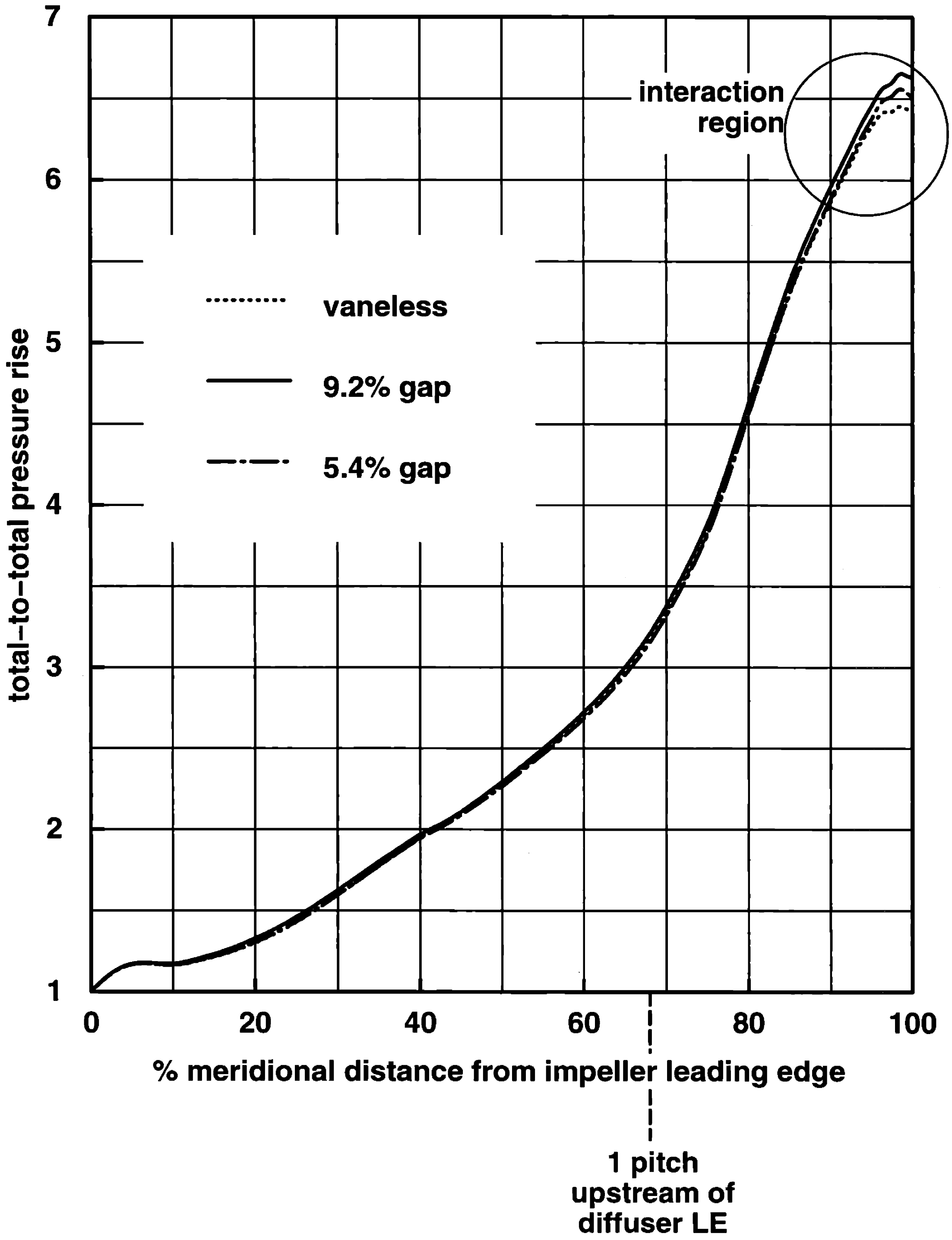

Figure 3-3: Mass and time averaged total pressure distribution along the impeller passage for the three different radial gap sizes

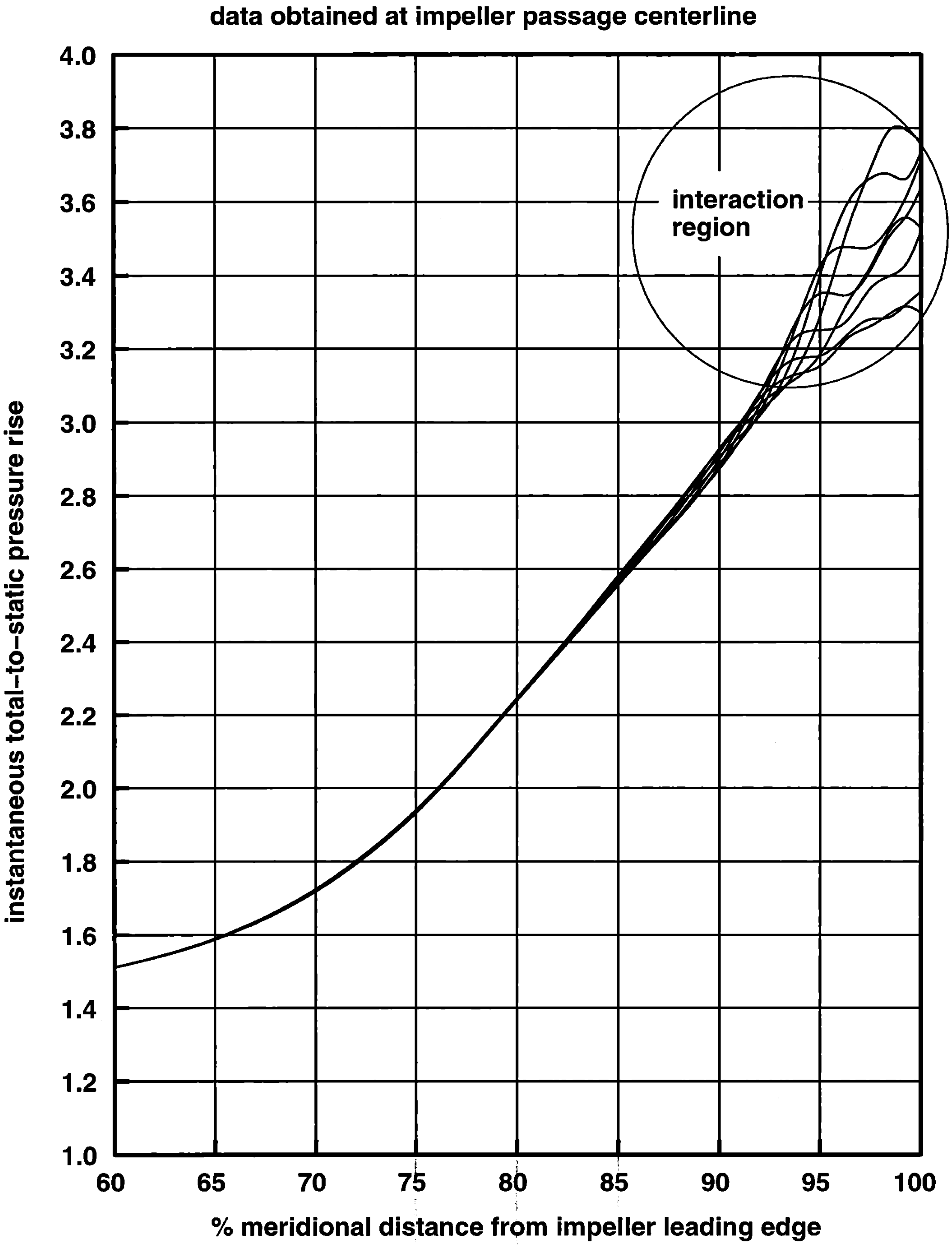

Figure 3-4: Instantaneous total-to-static pressure ratio p/p_{01} along impeller passage centerline of the $r_{2'}/r_2 = 1.092$ configuration, obtained at 8 different instants of one period with equal time intervals in between

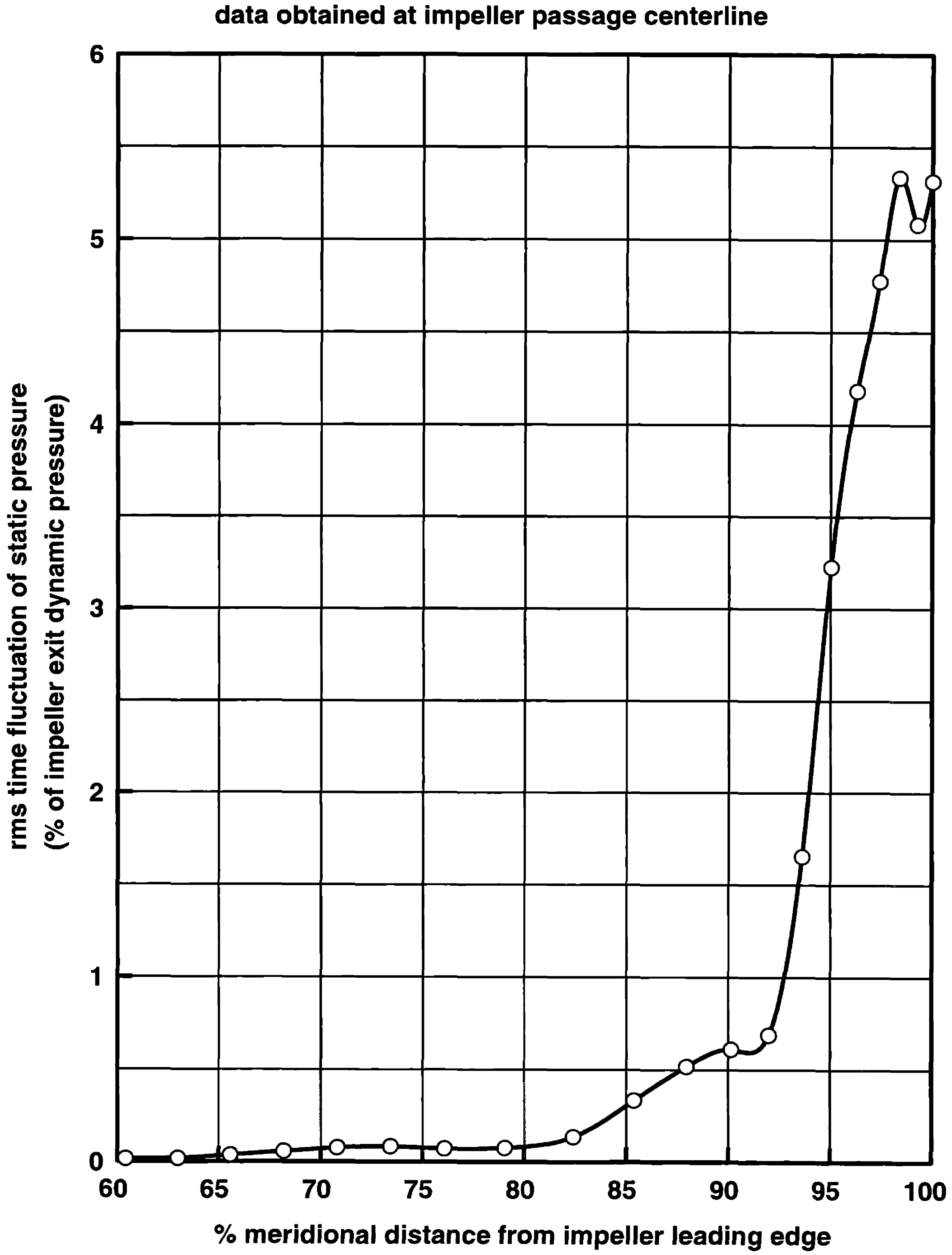

Figure 3-5: Rms time fluctuation of static pressure along impeller passage centerline of the $r_{2'}/r_2 = 1.092$ configuration, non-dimensionalized against impeller exit dynamic pressure $p_{02} - p_2$

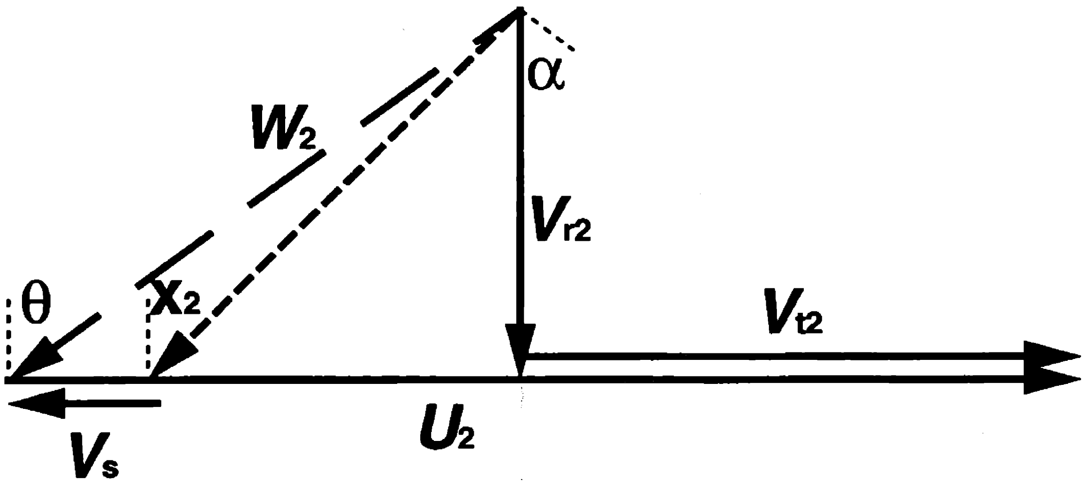

Figure 3-6: Velocity triangle at the impeller exit

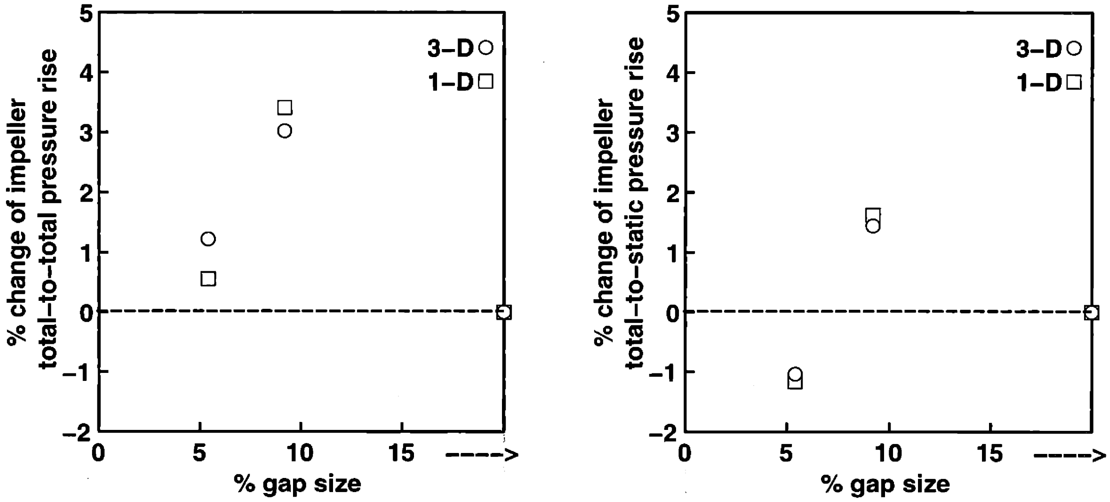

(a) $\frac{\Delta p_{02}}{p_{02}}$ (b) $\frac{\Delta p_2}{p_2}$

Figure 3-7: Effect of radial gap size on impeller total pressure ratio and static pressure ratio, expressed in increment change from the vaneless configuration

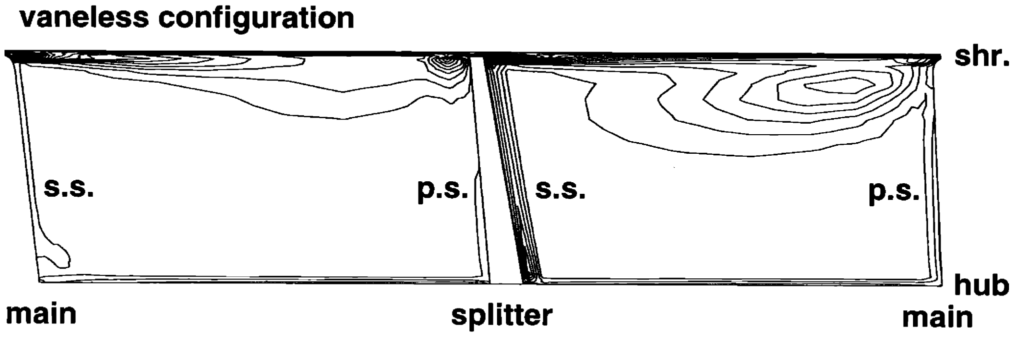

vaneless configuration

Figure 3-8: Contours of entropy production $\rho\frac{Ds}{Dt}$ at impeller exit for vaneless configuration

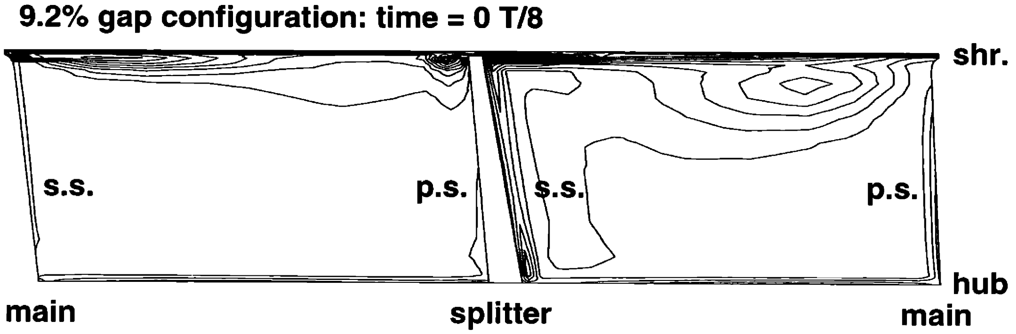

9.2% gap configuration: time = 0 T/8

Figure 3-9: Contours of entropy production $\rho\frac{Ds}{Dt}$ at impeller exit for $r_{2'}/r_2 = 1.092$ ($t = 0.000T$)

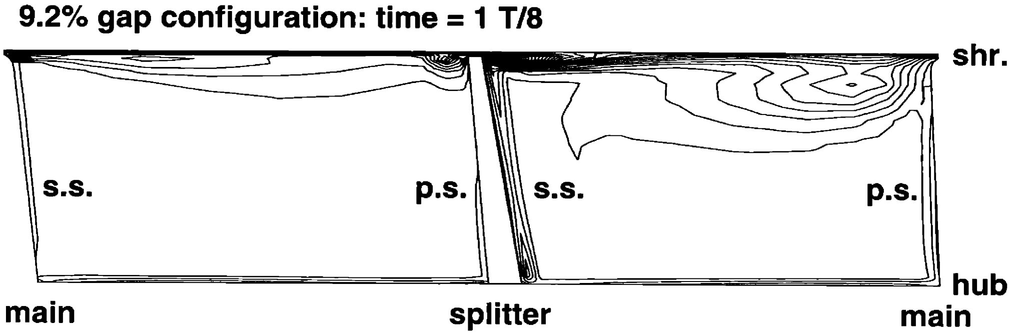

9.2% gap configuration: time = 1 T/8

Figure 3-10: Contours of entropy production $\rho\frac{Ds}{Dt}$ at impeller exit for $r_{2'}/r_2 = 1.092$ ($t = 0.125T$)

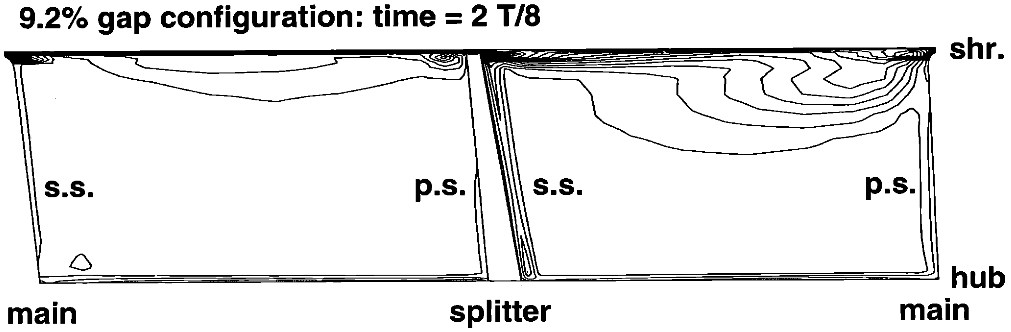

Figure 3-11: Contours of entropy production $\rho\frac{Ds}{Dt}$ at impeller exit for $r_{2'}/r_2 = 1.092$ $(t = 0.250T)$

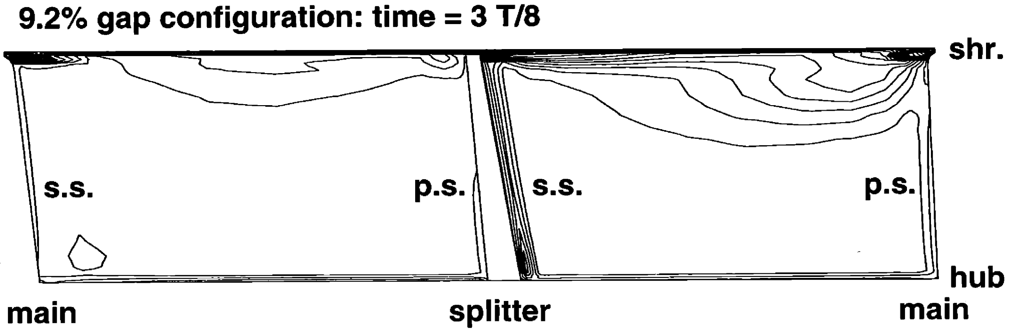

Figure 3-12: Contours of entropy production $\rho\frac{Ds}{Dt}$ at impeller exit for $r_{2'}/r_2 = 1.092$ $(t = 0.375T)$

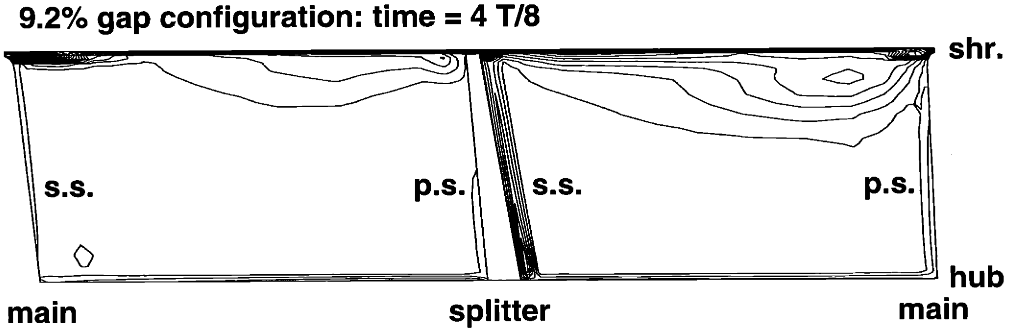

Figure 3-13: Contours of entropy production $\rho\frac{Ds}{Dt}$ at impeller exit for $r_{2'}/r_2 = 1.092$ $(t = 0.500T)$

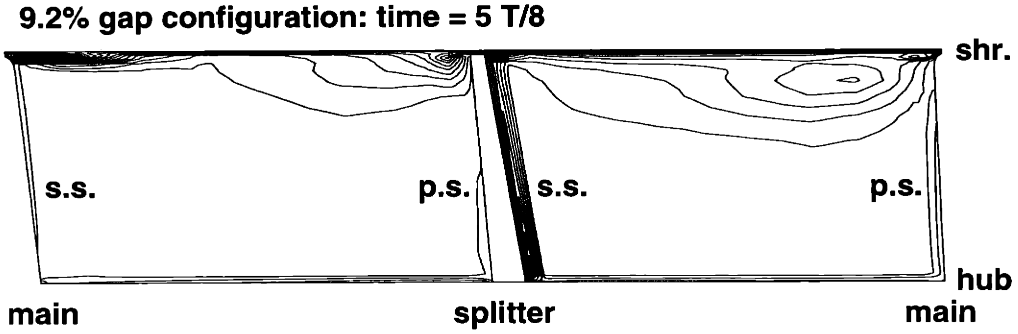

Figure 3-14: Contours of entropy production $\rho\frac{Ds}{Dt}$ at impeller exit for $r_{2'}/r_2 = 1.092$ $(t = 0.625T)$

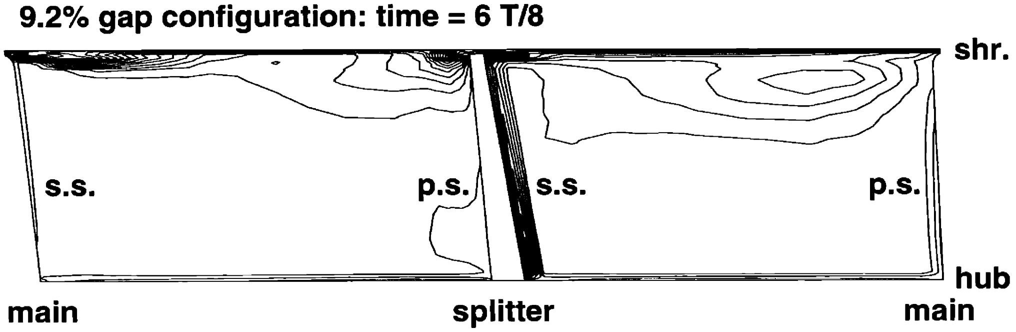

Figure 3-15: Contours of entropy production $\rho\frac{Ds}{Dt}$ at impeller exit for $r_{2'}/r_2 = 1.092$ $(t = 0.750T)$

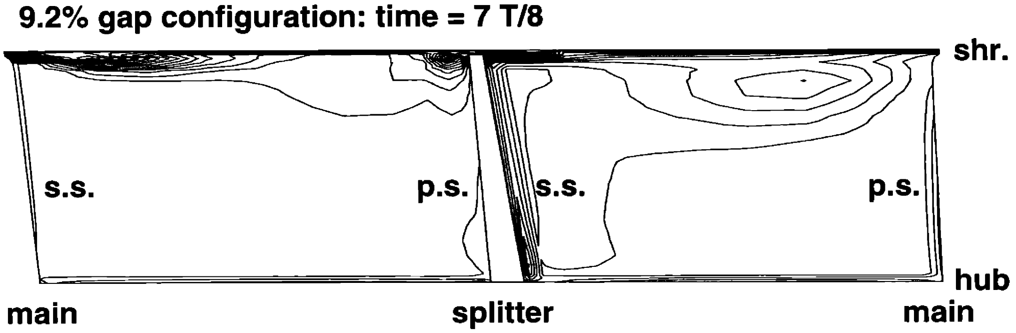

Figure 3-16: Contours of entropy production $\rho\frac{Ds}{Dt}$ at impeller exit for $r_{2'}/r_2 = 1.092$ $(t = 0.875T)$

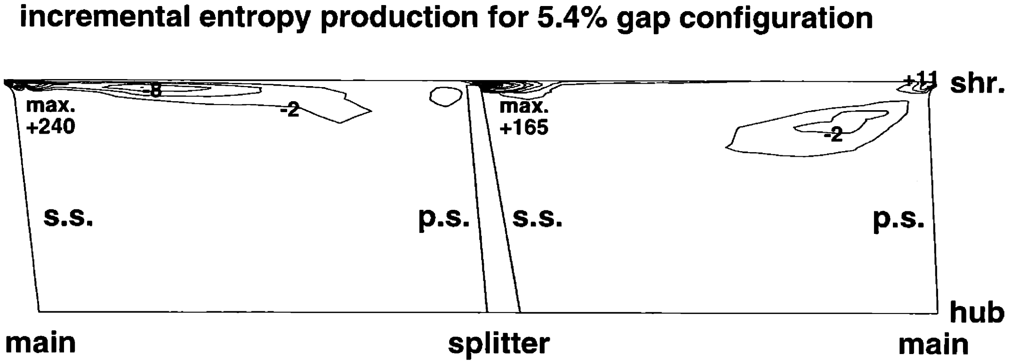
incremental entropy production for 5.4% gap configuration

(a) $r_{2'}/r_2 = 1.054$

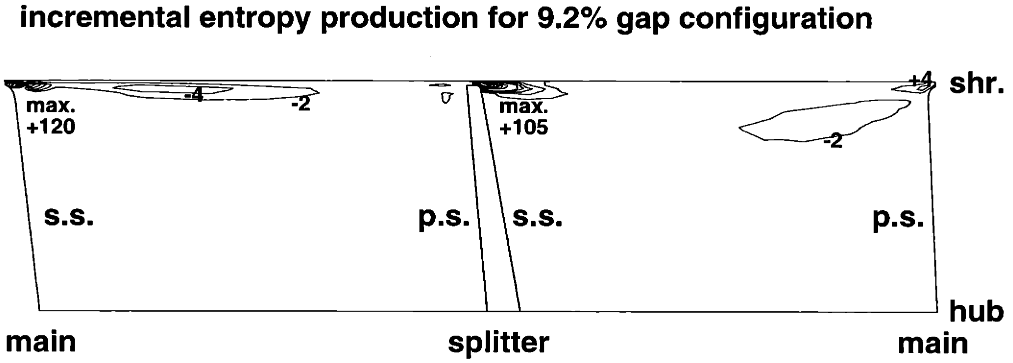
incremental entropy production for 9.2% gap configuration

(b) $r_{2'}/r_2 = 1.092$

Figure 3-17: Incremental entropy production $\Delta(\rho\frac{Ds}{Dt})$ for the two vaned configurations when compared to the vaneless configuration

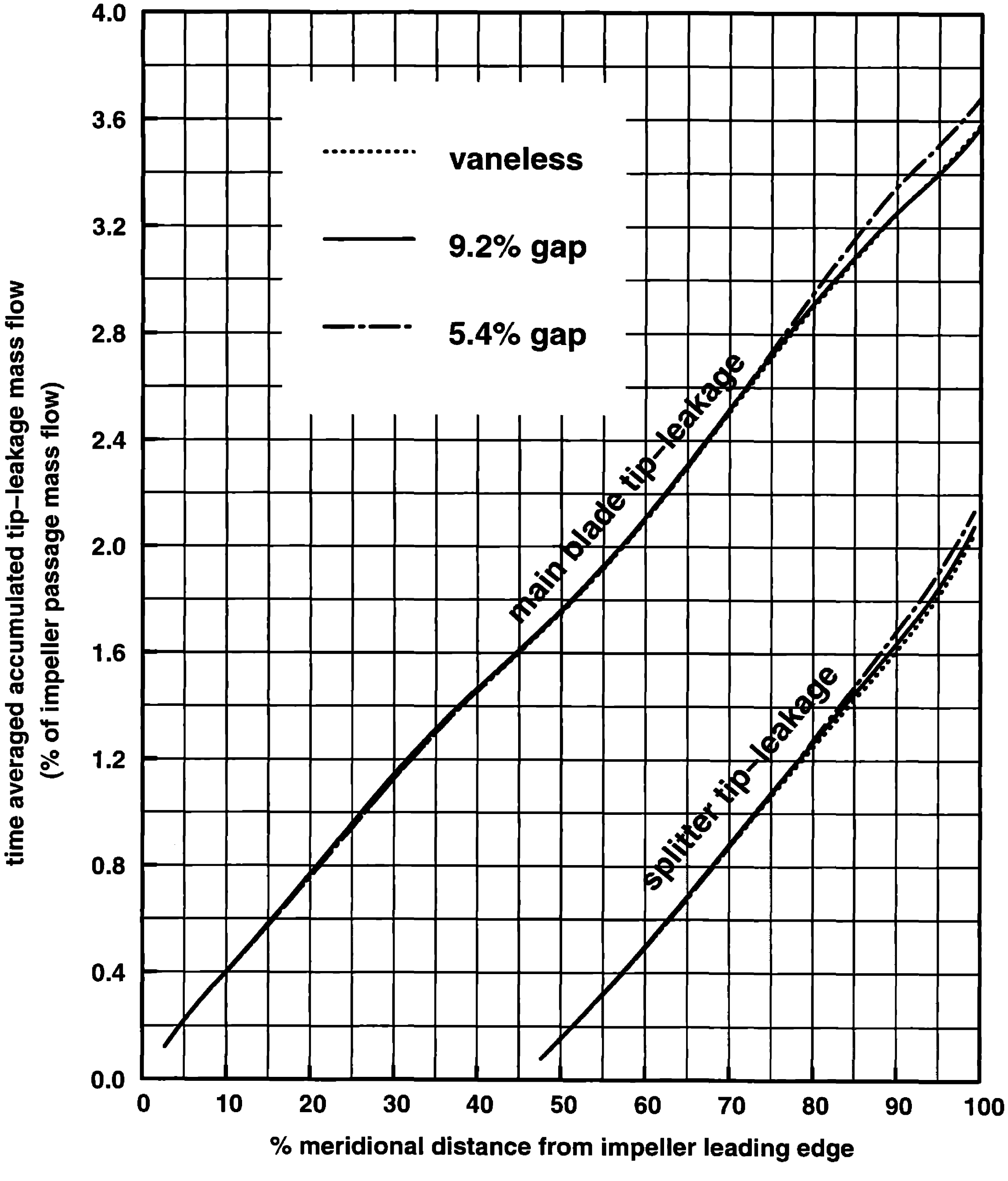

Figure 3-18: Time averaged accumulated tip leakage mass flow $\frac{\dot{m}_{tip}}{\dot{m}}$ for three different radial gap sizes

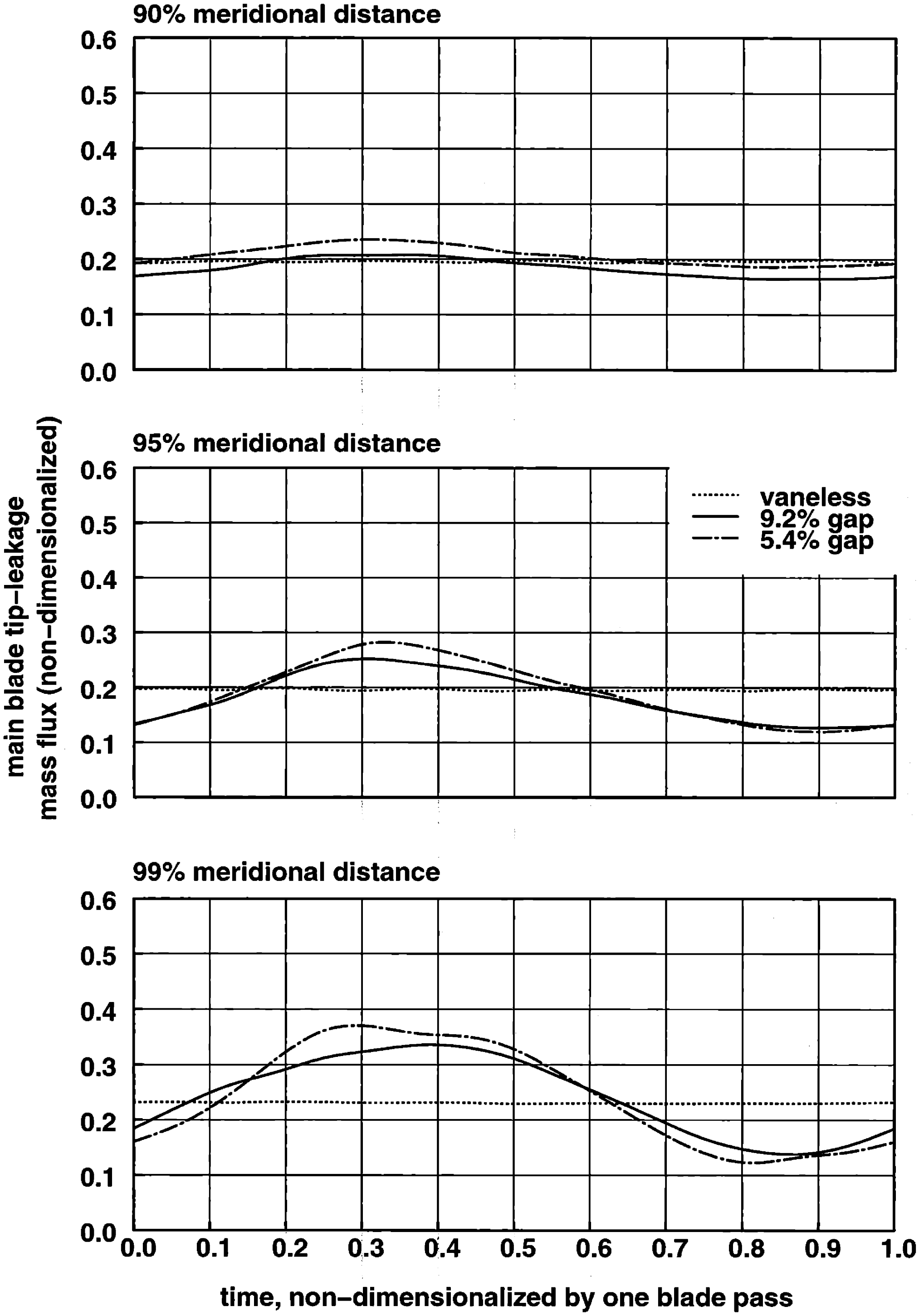

Figure 3-19: Comparison of main blade clearance periodic tip leakage mass flux at 90%, 95%, 99% meridional stations for three different radial gap sizes

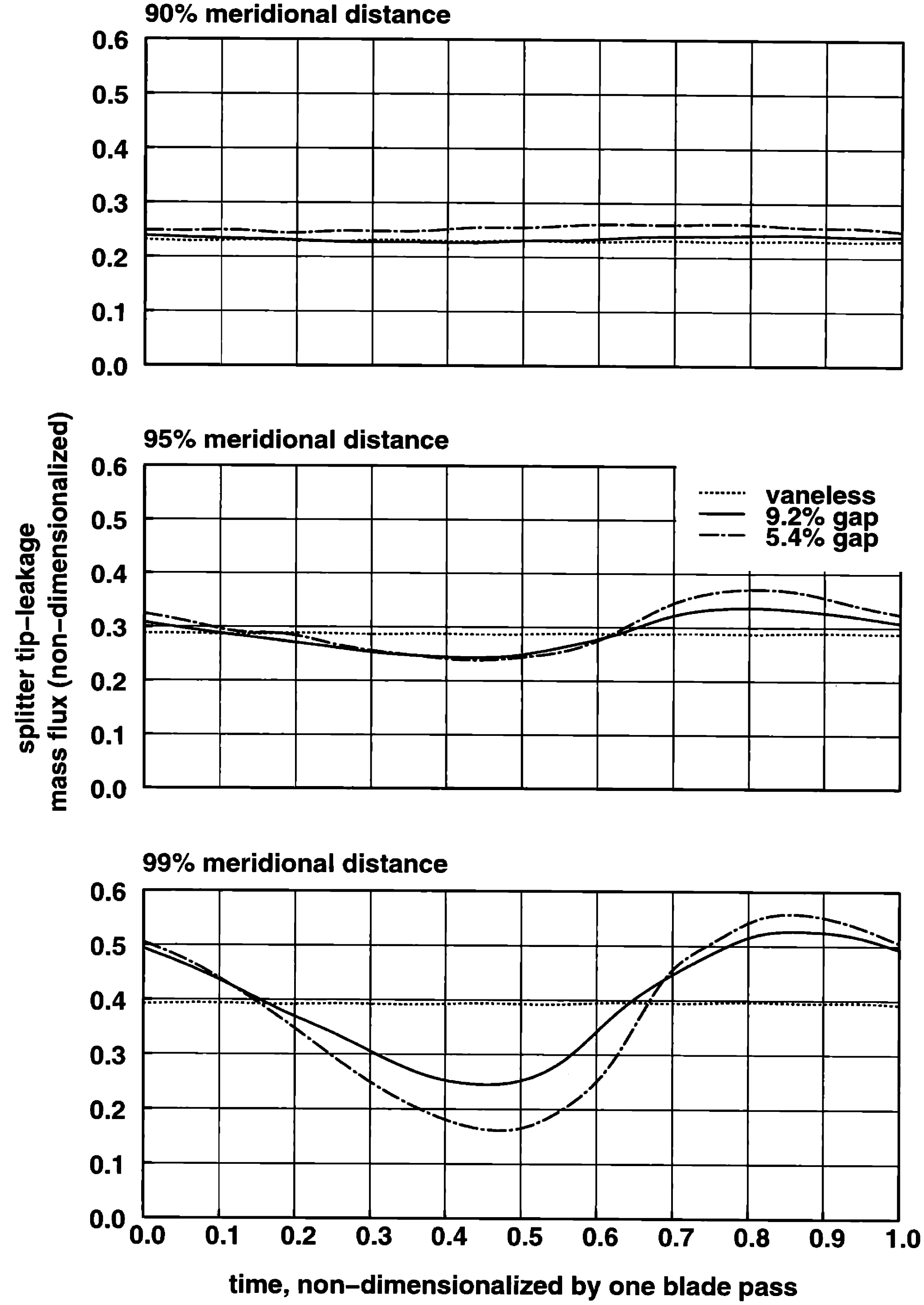

Figure 3-20: Comparison of splitter clearance periodic tip leakage mass flux at 90%, 95%, 99% meridional stations for three different radial gap sizes

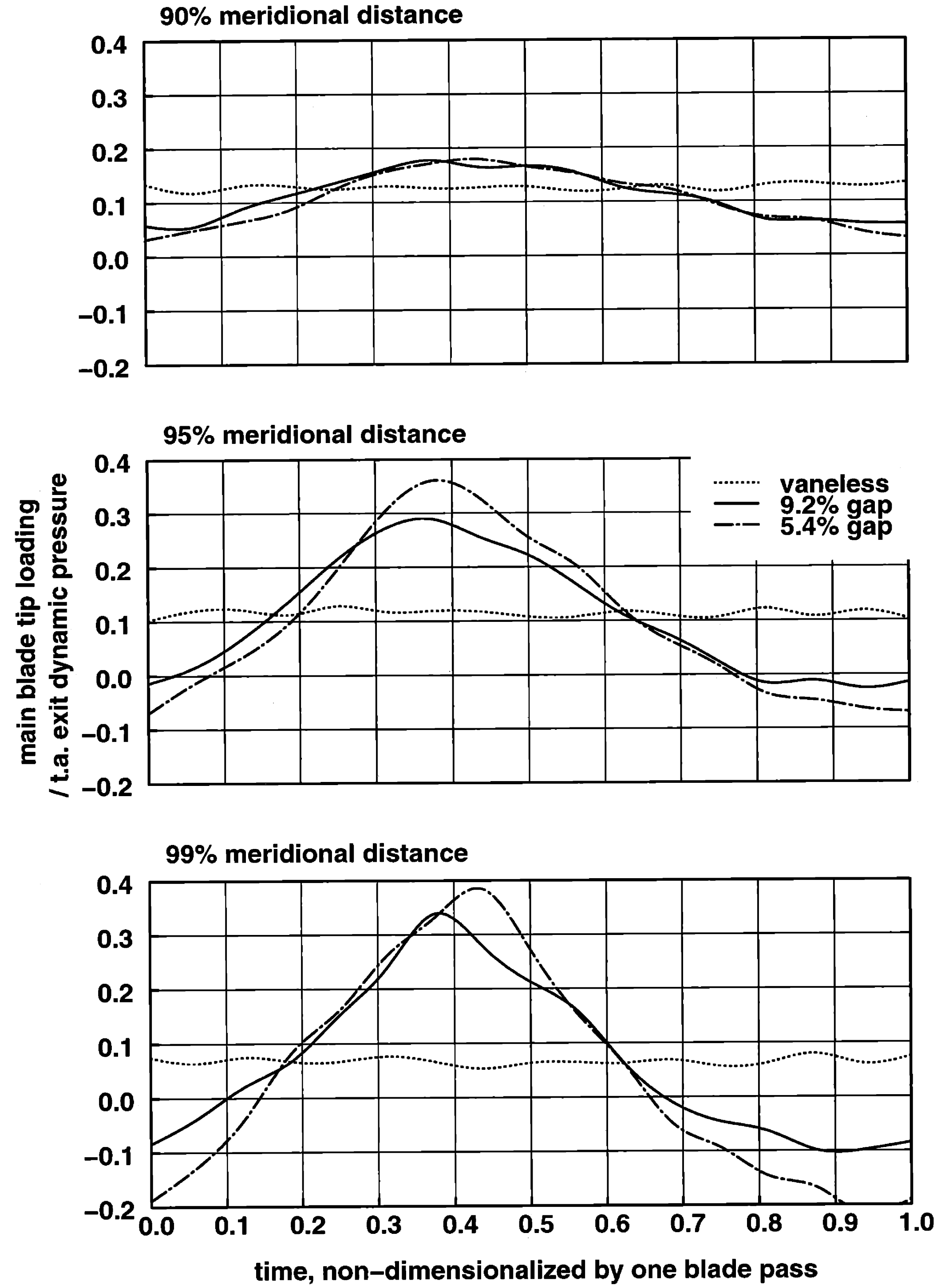

Figure 3-21: Comparison of periodic main blade tip loading $\frac{p_{ps}-p_{ss}}{\overline{p_{02}}-\overline{p_2}}$ at 90%, 95%, 99% meridional stations for three different radial gap sizes

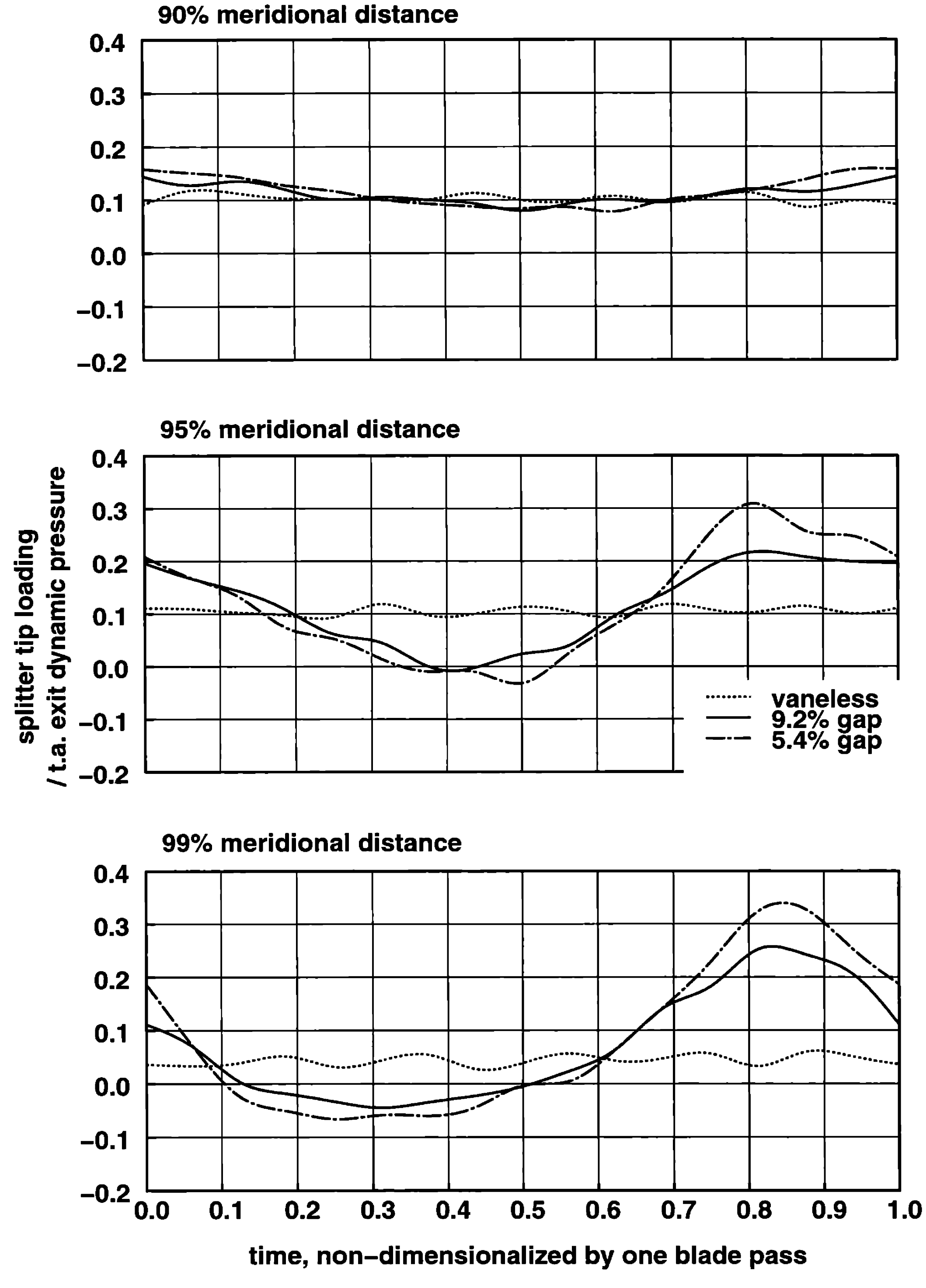

Figure 3-22: Comparison of periodic splitter tip loading $\frac{p_{ps}-p_{ss}}{p_{02}-p_2}$ at 90%, 95%, 99% meridional stations for three different radial gap sizes

vaneless configuration

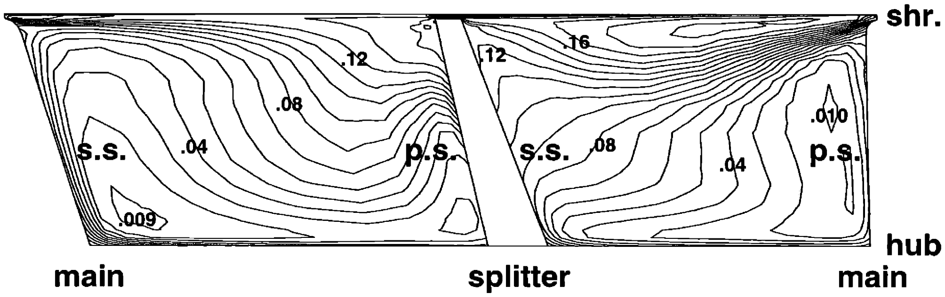

vaned diffuser with 9.2% gap

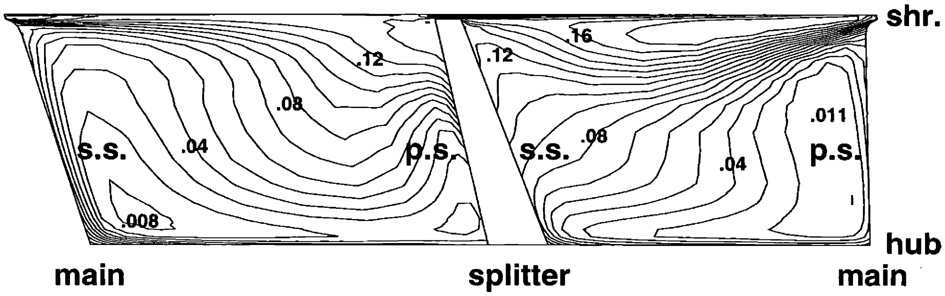

vaned diffuser with 5.4% gap

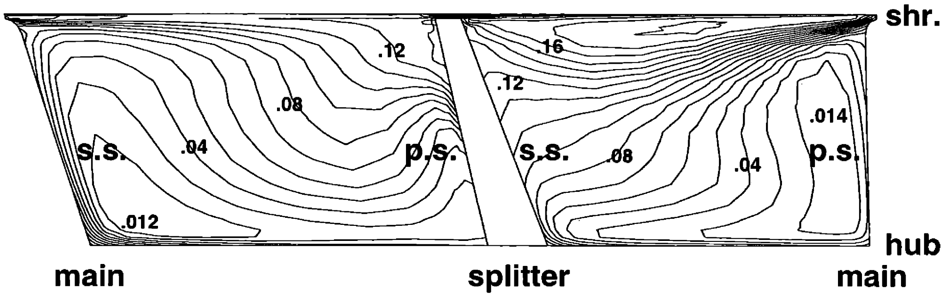

Figure 3-23: Comparison of entropy rise $\frac{s-s_1}{C_p}$ at the 90% meridional station between three different radial gap sizes

vaneless configuration

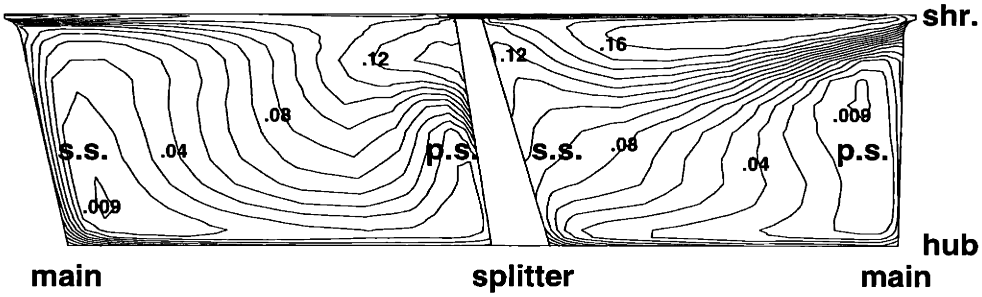

vaned diffuser with 9.2% gap

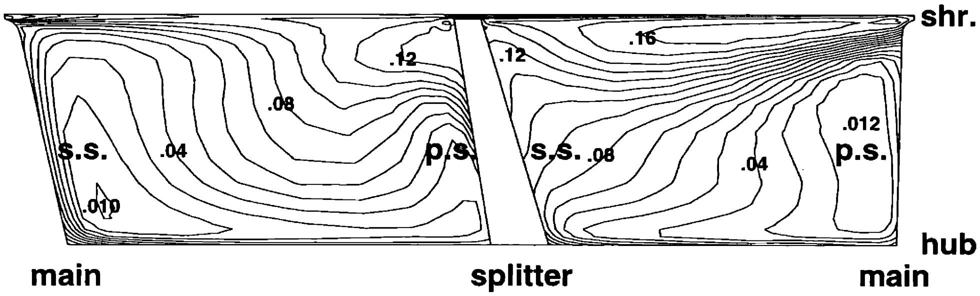

vaned diffuser with 5.4% gap

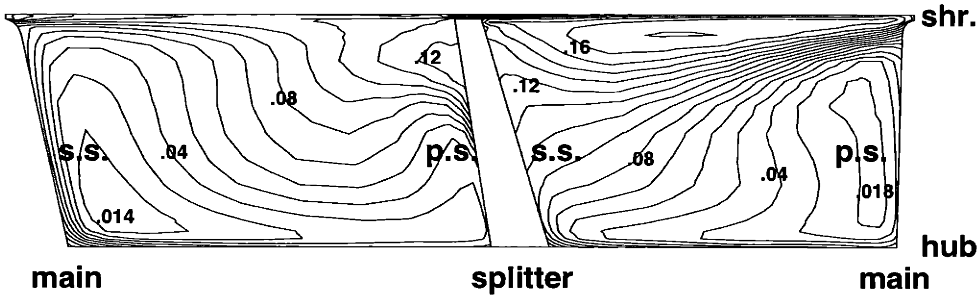

Figure 3-24: Comparison of entropy rise $\frac{s-s_1}{C_p}$ at the 95% meridional station between three different radial gap sizes

vaneless configuration

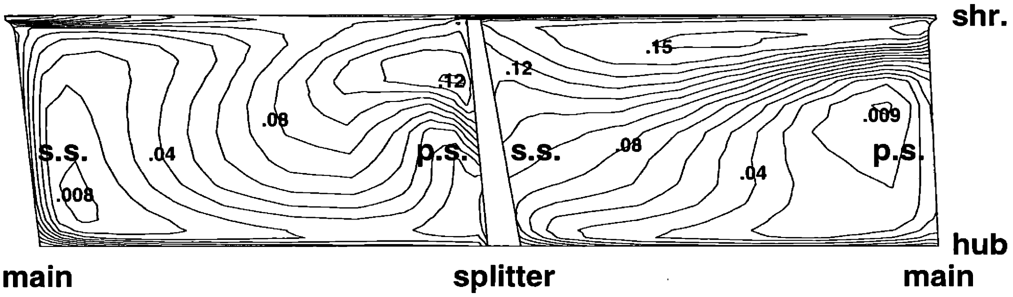

vaned diffuser with 9.2% gap

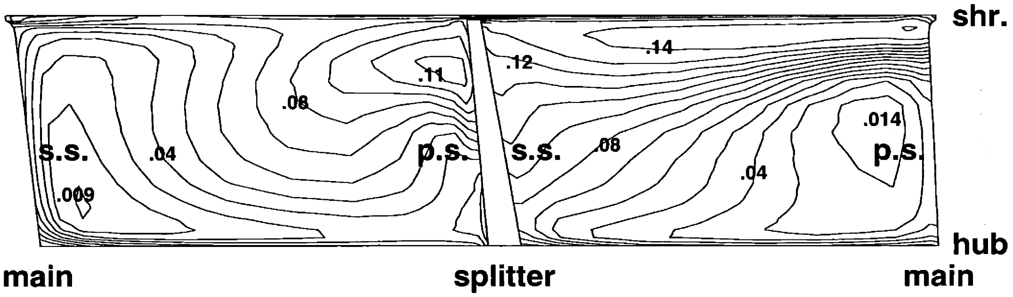

vaned diffuser with 5.4% gap

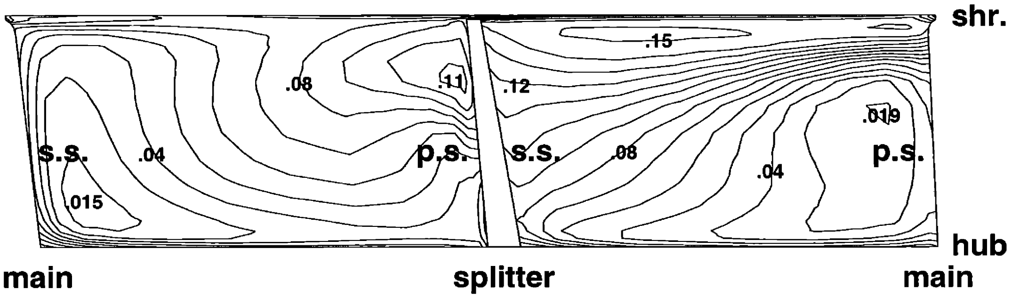

Figure 3-25: Comparison of entropy rise $\frac{s-s_1}{C_p}$ at the 99% meridional station between three different radial gap sizes

vaneless configuration

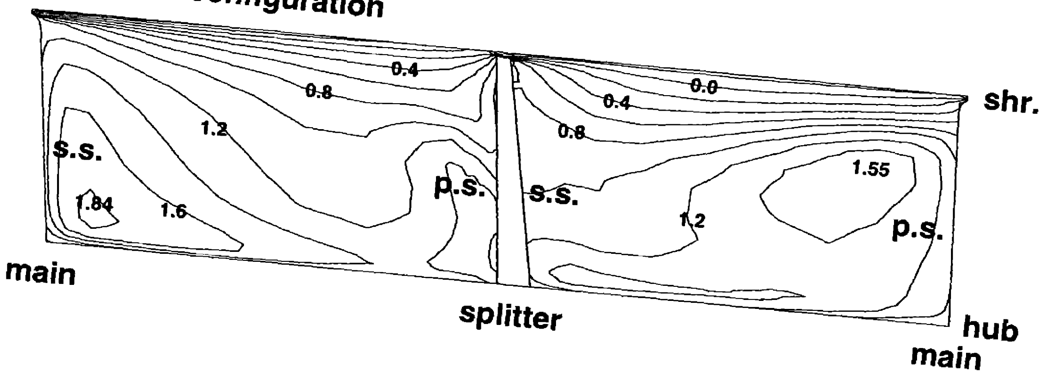

vaned diffuser with 9.2% gap

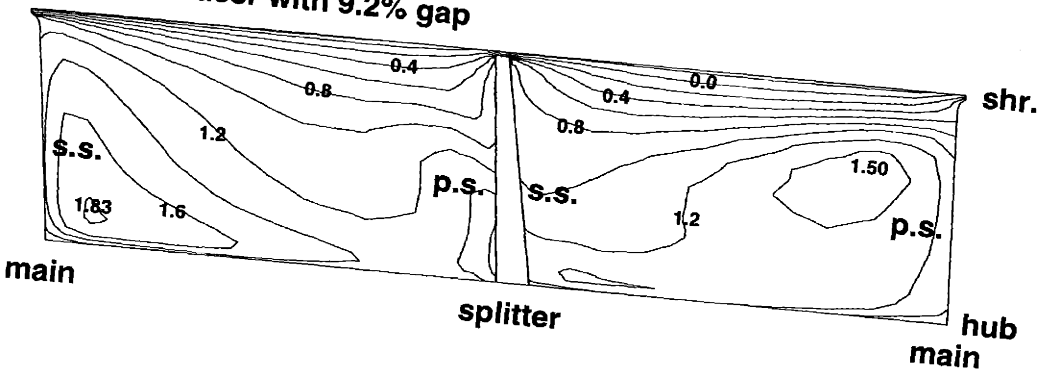

vaned diffuser with 5.4% gap

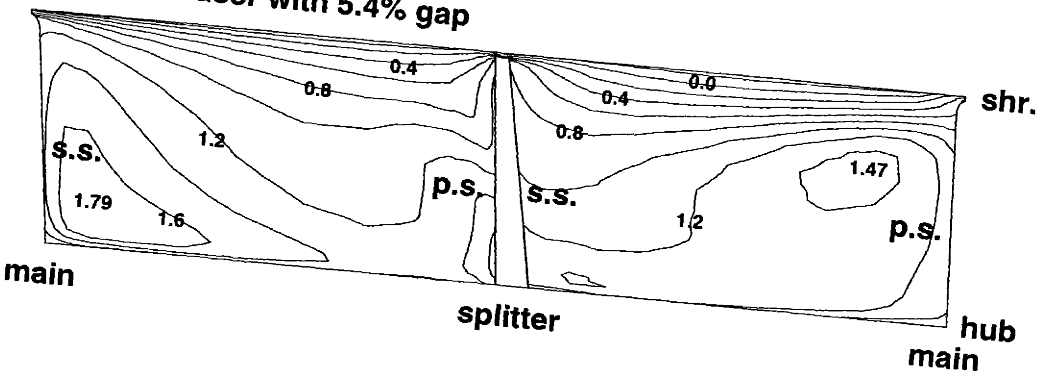

Figure 3-26: Comparison of non-dimensional mass flux at the 99% meridional station between three different radial gap sizes

CHAPTER 4

INFLUENCE OF INTERACTION ON DIFFUSER FLOW AND STAGE PERFORMANCE

4.1 Introduction

This chapter presents qualitative and quantitative descriptions of the flow in the diffuser with different combinations of upstream parameters prescribed at the interaction plane. The main objective is to quantify the importance of inlet unsteadiness on the diffuser performance against other upstream factors, namely:

- axial (hub-to-shroud) distortions
- momentum-averaged inlet swirl angle [14]

The influence of the axial distortions has been investigated by Phillips [33], who concludes that its effect on diffuser pressure recovery C_p is minimal compared to that from the inlet swirl angle, which has been identified by Filipenco and Deniz et.al. [9, 10, 14, 15] as the single most important parameter in setting C_p.

It is recognized that interaction can change the impeller outflow angle. As seen in Table 3.2, the flow angle in the relative frame (θ in Figure 3-6) shifts from 55.7° for the vaneless configuration to 54.8° for the $r_{2'}/r_2 = 1.092$ configuration. However, since a designer can always match the diffuser geometry to the modified impeller outflow angle by adjusting the diffuser alignment, unsteadiness remains the only interaction-caused factor to be understood (in terms of its effect on the diffuser performance); thus flow unsteadiness is the focus of this chapter.

The approach is, again, to set up three control numerical experiments, so that the two inlet factors stated above can be isolated. The time-accurate calculation for the $r_{2'}/r_2 = 1.092$ configuration is chosen as the reference case, which also supplies the boundary conditions for the two subsequent diffuser-alone steady calculations. Respectively named as calculations 2, 4, 5, the corresponding procedures have been outlined in Section 2.4 and Table 2.2 presents the difference these calculations are designed to isolate. It should be stressed again that the unsteadiness and axial distortions in the comparison are representative of those found in the impeller exit flow because they are all derived from the data of the full interaction case.

4.2 Numerical Results

The swirl angle distribution in the vane leading edge region is shown in Figure 4-1, with the flow direction pointing out from the page. The data are obtained at the vane leading edge plane at $r_{2'}/r_2 = 1.092$. Comparing the results from calculations 2 and 4 indicates that eliminating upstream unsteadiness has a minimal impact on the swirl angle distribution near the leading edge. The angle distribution from calculation 5 does look different from the other two cases because axially uniform flow has been prescribed upstream. However, the area enclosed by the 70° contour is basically the same for all three cases, and this region is where most of the flow momentum is. Thus, eliminating upstream axial distortions relocates the high momentum region away from the hub and towards the center, but has little impact on the momentum ratio of the flow entering the diffuser channel, as $\alpha_{2'}$ virtually stays constant for the three cases.

The results of the three calculations are summarized in Figure 4-2 which describes the development of both pressure recovery C_p and loss C_{loss} in the diffuser channel. It can be seen that the radial distribution of the pressure recovery (after mass averaging) is similar for the three cases. More than half of the pressure recovery is obtained in the throat region, which extends from $r/r_2 = 1.092$ (leading edge) to $r/r_2 = 1.18$, demonstrating the vane's function of reducing the angular momentum of the incoming flow. Elimination of upstream unsteadiness (difference between calculations 2 and 4) increases C_p by 0.008 while further elimination of upstream axial distortions (difference between calculations 4 and 5) increases C_p by another 0.005. Compared to the magnitude of the change in C_p (0.013), a similar change of C_{loss} (0.017) is observed when both inlet unsteadiness and inlet distortion are eliminated from the incoming flow. Thus the effect of inlet unsteadiness on the overall diffuser performance is roughly comparable to that due to inlet axial distortions. Put it quantitatively, the 0.008 reduction in C_p due to unsteadiness is equivalent to mismatching the vane orientation by 0.3°, as demonstrated in Deniz's [9] experiments on some commonly available straight-vaned diffusers. Such change is an order of magnitude smaller than the operating range of those diffusers, confirming that the flow angle alignment with the diffuser vane is the single most important factor that determines diffuser performance.

4.3 Explanation of Observations

This section is divided into two parts. Section 4.3.1 discusses the effect of interaction on diffuser performance. By combining this and the impact on the impeller performance (Chapter 3), a global look at the influence of interaction on stage performance is possible and will be presented in Section 4.3.2.

4.3.1 Effect of Interaction on Diffuser Performance

Phillips [33] concludes that for steady incoming flow with axial distortions, momentum transfer within the flow energizes region of high flow angle misalignment, causing local separation bubbles to reattach to the vane suction surface, thus preserving diffuser performance. His argument is equally applicable to the unsteady flow situation. In other words, in addition to axial distortions, unsteadiness merely adds an additional level of non-uniformity to the flow.

This point is illustrated by Figure 4-3 which plots the instantaneous mid-pitch (midway between the vane leading edges) swirl angle on the leading edge plane at $r_{2'}/r_2 = 1.092$ for the full interaction calculation (no. 2). The time variation at three axial locations (respectively 10% from the shroud, mid-span, and 10% from the hub) are shown. Also shown for comparison is the mid-pitch swirl angle at the same locations for the steady calculation with upstream unsteadiness already eliminated (no. 4). For the steady flow situation, it can be seen that axial variation of swirl angle $\alpha_{2',mp}(x)$ is more than 12°, with $\alpha_{2',mp,hub} = 64°$ and $\alpha_{2',mp,shroud} = 76°$. The subscript mp signifies the angles are obtained at mid-pitch.

In addition to the 12° axial variation, unsteadiness adds another 8° to the swirl angle non-uniformity, resulting in a total variation of 20°. As seen in Figure 4-3, the additional 8° comes from the periodic peak-to-peak angle fluctuation. A remaining question is how the flow can enter the diffuser channel without triggering massive separation when some portion has incidence so mis-aligned with the vanes. The answer can be found in the static pressure distribution of the two calculations.

Figure 4-4 shows the time-averaged static pressure distributions of the unsteady calculation (no. 2) near the leading edge on three axial planes (10% from shroud, mid-span, 10% from hub), and Figure 4-5 shows the distributions for the steady calculation (no. 4) at the same locations. All the plots have the same contour intervals ($\Delta\left(\frac{p-p_2}{p_{02}-p_2}\right) = 0.05$). All six distributions look very similar regardless of axial location, although upstream axial distortions have been retained in both calculations. This implies that the diffuser flow is subject to virtually identical time-averaged two-dimensional pressure gradient, whose establishment depends solely on the time-averaged and spatially-averaged alignment of the flow incidence (momentum averaged inlet swirl angle) with the diffuser vanes. Only the alignment can ensure that a favorable pressure field exists to guide the flow into the diffuser channel. The type or magnitude of the non-uniformity around this angle is largely irrelevant.

Although the improvement in pressure recovery and loss after eliminating upstream unsteadiness and axial distortions is only marginal, it is still of interest to understand why there is an improvement. In fact, it can be examined using the one-dimensional flow model presented by Greitzer [18]. This analysis basically shows that nozzles suppress velocity non-uniformities while diffusers worsen them because the increasing pressure level in a diffuser decelerate the slower streams more than the quicker streams. The implication is that bringing the non-uniform flow to a uniform state before it passes through a diffuser introduces less loss compared to performing this procedure inside (or after the flow has exited) the diffuser. The former is exactly what happens in the two steady calculations (no. 4 and 5) in which upstream non-uniformities in the time domain and in the spatial domain are eliminated. The flow is brought to a more uniform state before it enters the diffuser, and as a result, loss is reduced and pressure recovery is increased. Since the time variation for the swirl angle (8°) is in the same order of magnitude as that due to axial distortions (12°), their effect on pressure recovery and loss are roughly comparable to each other, as seen in Figure 4-2.

In conclusion, the computed diffuser performance depends primarily on the alignment of the time and spatially-averaged flow incidence with the diffuser vanes. The independence of diffuser performance from upstream unsteadiness is in contrast to the sensitivity of impeller performance to downstream unsteadiness, as identified in Chapter 3.

4.3.2 Effect of Interaction on Stage Total-to-Static Pressure Ratio

The relative importance of each factor in contributing to stage total-to-static pressure ratio can be studied by linearizing Equation 3.11:

$$\frac{\Delta' p_3}{p_3} = K_{p02}\left(\frac{\Delta' p_{02}}{p_{02}}\right) + K_{p2}\left(\frac{\Delta' p_2}{p_2}\right) + K_{Cp}\left(\frac{\Delta' C_p}{C_p}\right) \tag{4.1}$$

Of the three independent variables, p_{02} and p_2 are the contribution from the impeller (Chapter 3) while C_p is the contribution from the diffuser (Chapter 4, above).

In Equation 4.1, Δ' signifies the change due to the reduction of radial gap size. K_{p02}, K_{p2}, and K_{Cp} are the corresponding influence coefficients. Their definitions are,

$$K_{p02} = \frac{C_p p_{02}}{p_3} > 0 \tag{4.2}$$

$$K_{p2} = \frac{(1 - C_p)p_2}{p_3} > 0 \tag{4.3}$$

$$K_{Cp} = \frac{(p_{02} - p_2)C_p}{p_3} > 0 \tag{4.4}$$

The performance changes associated with the reduction of radial gap size from $r_{2'}/r_2 = 1.092$ (Calculation 2) to $r_{2'}/r_2 = 1.054$ (Calculation 3) can then be substituted into Equation 4.1 for evaluation of their effect on the stage total-to-static pressure ratio p_3/p_{01}. The changes are summarized in Table 4.1.

As seen in Table 4.1, the gap size reduction (increased interaction) has more influence on the impeller performance, for which both p_{02}/p_{01} and p_2/p_{01} have a roughly 2% reduction. The diffuser performance is relatively insensitive to gap size reduction, as Cp increases by less than 1%. Substituting these changes into Equation 4.1 gives a value for $\Delta' p_3/p_3$ of -1.65%. Of this -1.65% change, -1.32% is due to the $\Delta' p_{02}$ term, -0.60% is due to the $\Delta' p_2$ term, and +0.27% is due to the diffuser term $\Delta' C_p$. The results demonstrate that most of the interaction influence on stage total-to-static pressure ratio can be attributed to the changes in the impeller. The explanation can be found in Chapter 3 which shows that the unsteadiness associated with the tip-leakage flow is responsible for the change in blockage and loss in the impeller exit flow. Both are major contributors to impeller pressure ratios (p_{02}/p_{01} and p_2/p_{01}) according to Table 3.3. In other words, impeller tip leakage flow is the principal mechanism for the impeller-diffuser interaction induced changes in stage performance.

4.4 Summary

Alignment of the diffuser vanes with the time and spatially-averaged impeller exit flow angle is singled out as the most important factor in setting the diffuser performance. The effects of other inlet factors, unsteadiness and axial distortions are found to be at least an order of magnitude smaller than the alignment effect.

However, since the current calculations are conducted near design point, there is little separated flow in the diffuser flow field for unsteadiness to act on. Separated flow may provide a similar mechanism as the impeller tip leakage flow to magnify the influence of the impeller-diffuser interaction on stage performance. Engineers should be cautious in applying the current findings in off-design conditions.

It is also possible that interaction can affect diffuser performance by changing the impeller exit flow angle, but a design engineer only needs to adjust the vane angle slightly to match flow angle shift to keep this influence to a minimum. Diffuser performance is thus less susceptible to interaction influence than impeller performance when the diffuser is operating near its design point.

Interaction		medium	strong	Δ'
	$r_{2'}/r_2$	1.092	1.054	
impeller influence	p_2/p_{01}	3.542	3.456	-2.44%
	p_{02}/p_{01}	6.625	6.509	-1.75%
diffuser influence	C_p	0.622	0.627	+0.77%
	α_2	67.4°	66.9°	
Σ: stage performance (from Equation 4.1)	p_3/p_{01}	5.461	5.371	-1.65%

Table 4.1: Change of stage total-to-static pressure ratio and other performance parameters due to a reduction of radial gap size $r_{2'}/r_2$ from 1.092 to 1.054

Calculation 2: Time-accurate calculation
full interaction (data presented after time averaging)

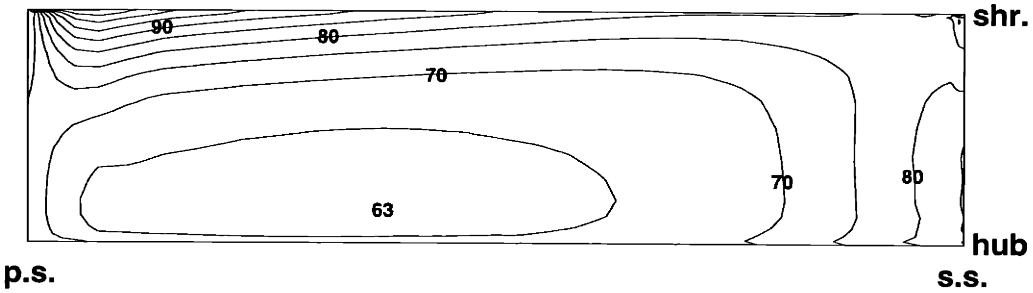

Calculation 4: Steady calculation
with inlet unsteadiness eliminated

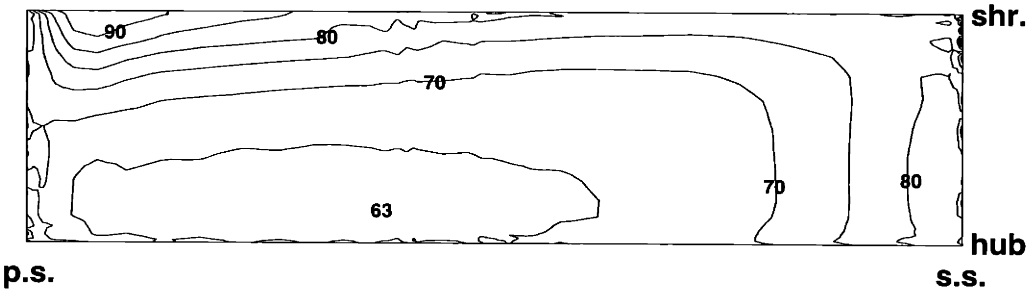

Calculation 5: Steady calculation with
both inlet unsteadiness and axial distortions eliminated

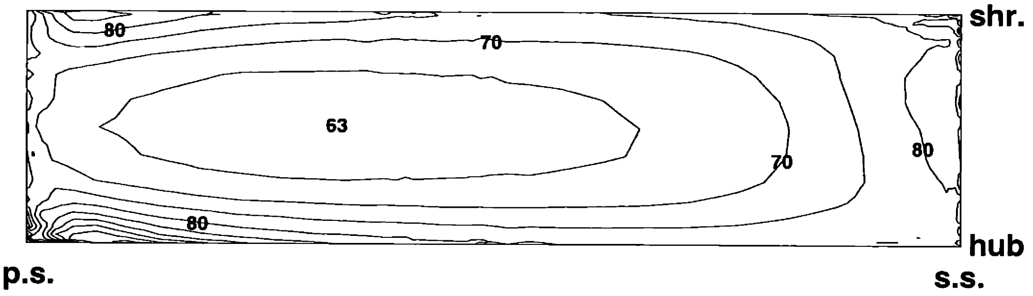

Figure 4-1: Comparison of local swirl angle (in degrees) at the diffuser vane leading edge plane at $r/r_2 = 1.092$ after elimination of upstream non-uniformities: unsteadiness and axial distortions

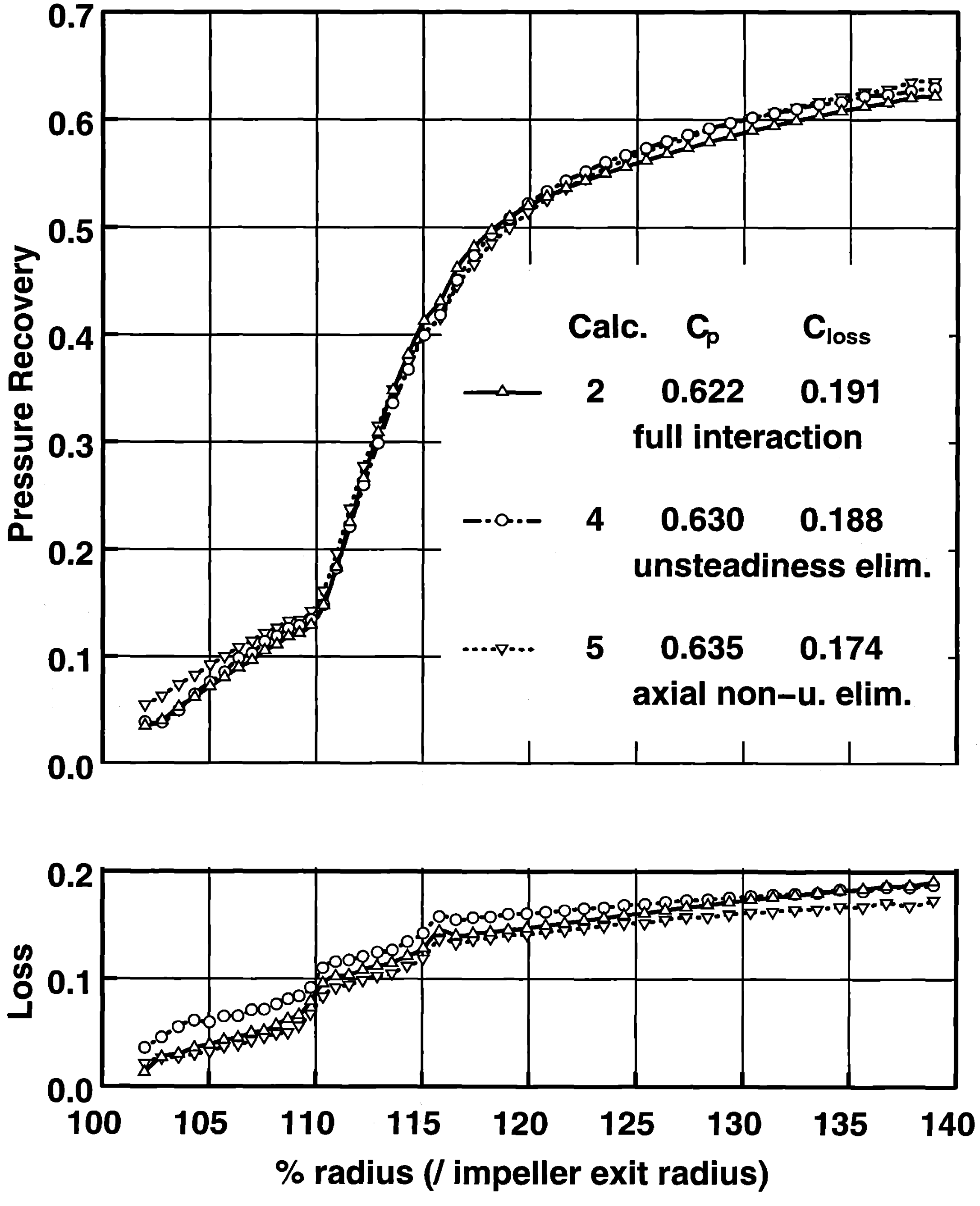

Figure 4-2: Comparison of pressure recovery C_p and loss C_{loss} for calculations 2, 4, 5

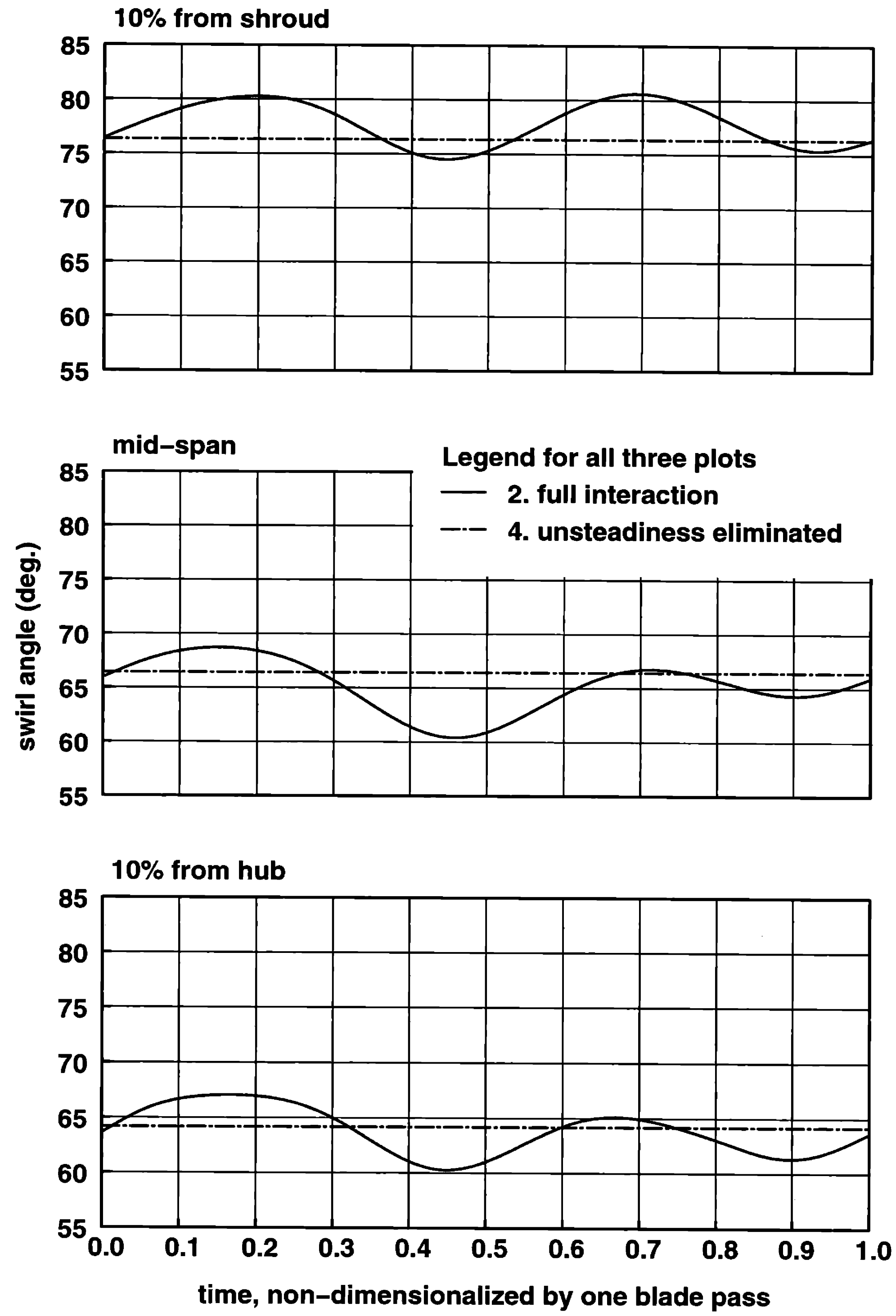

Figure 4-3: Effect of unsteadiness on the swirl angle at mid-pitch of the diffuser inlet plane

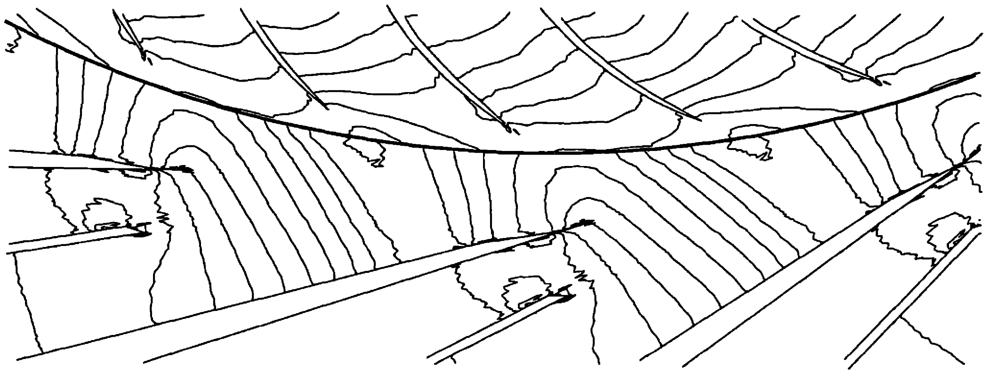

(a) 10% from shroud

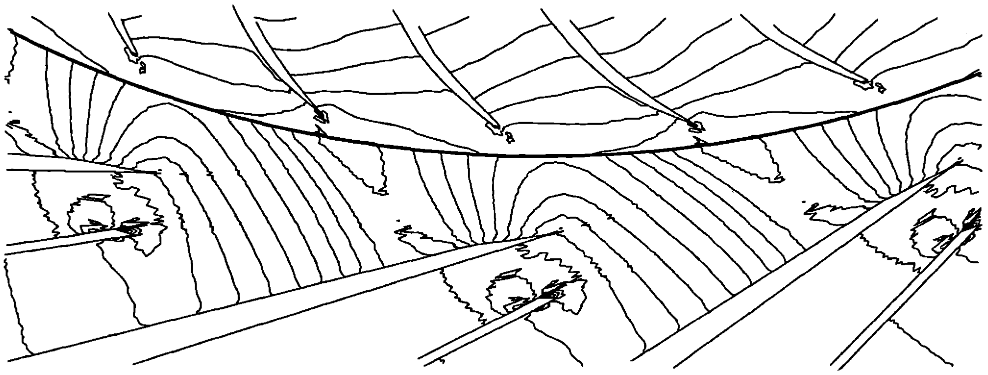

(b) mid-span

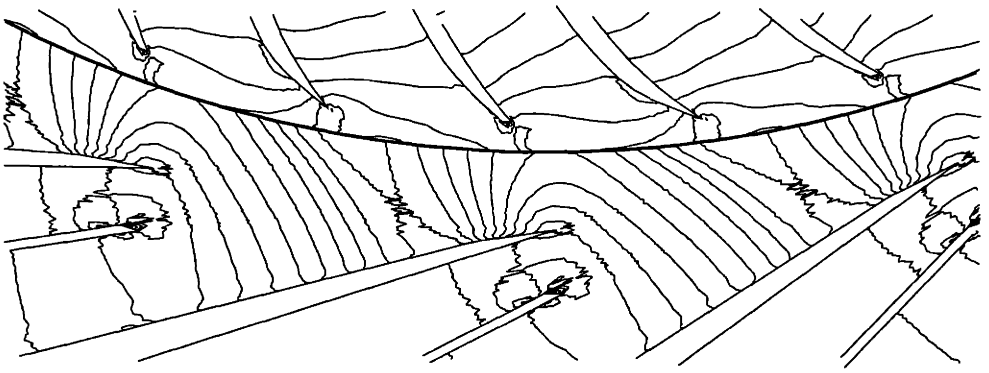

(c) 10% from hub

Figure 4-4: Comparison of time-averaged pressure distribution ($\Delta\left(\frac{p-p_2}{p_{02}-p_2}\right) = 0.05$) around the leading edge region at three different axial planes for the $r/r_2 = 1.092$ configuration (Calculation 2)

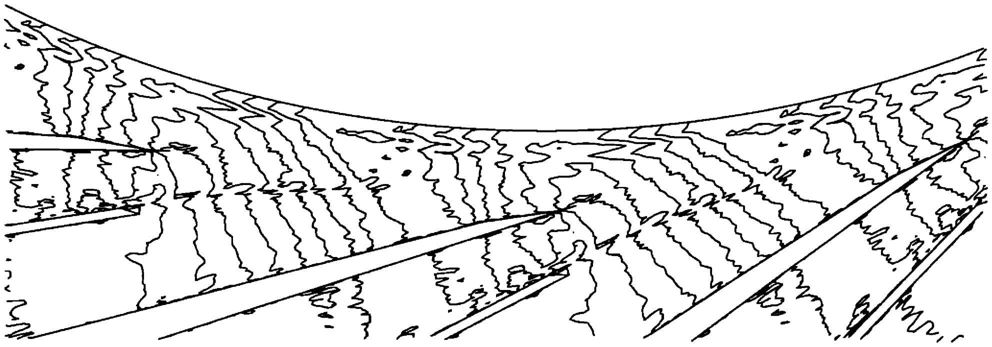

(a) 10% from shroud

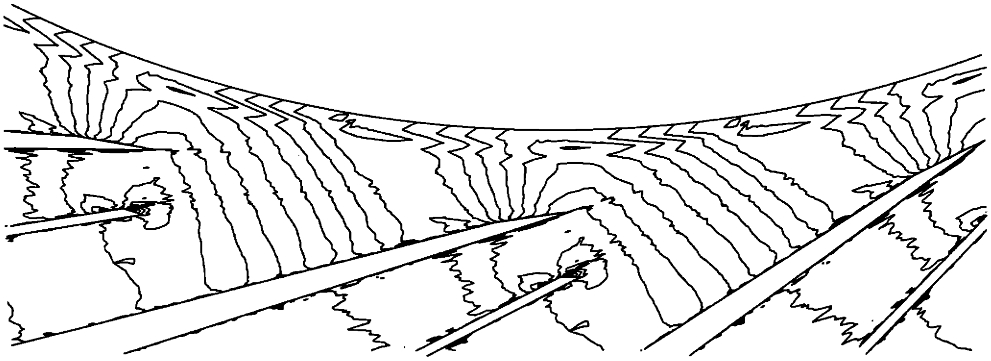

(b) mid-span

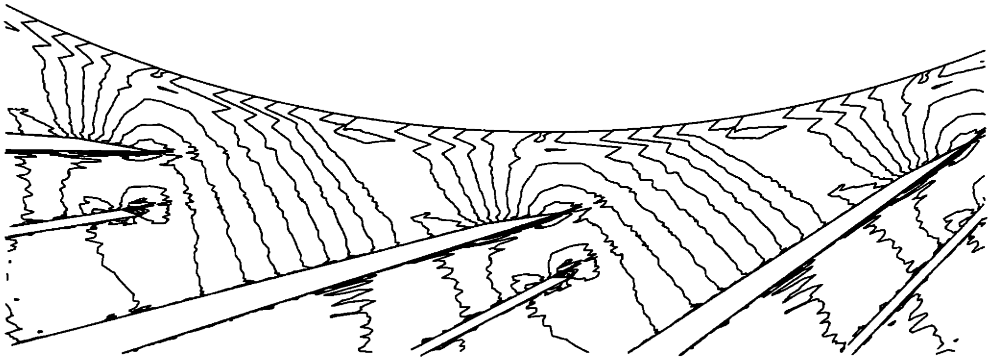

(c) 10% from hub

Figure 4-5: Comparison of pressure distribution ($\Delta\left(\frac{p-p_2}{p_{02}-p_2}\right) = 0.05$) around the leading edge region at three different axial planes for the diffuser alone calculation with upstream unsteadiness eliminated (Calculation 4)

CHAPTER 5

SYNTHESIS OF COMPUTED RESULTS FOR CENTRIFUGAL COMPRESSOR STAGE

This chapter is aimed at providing guidelines for centrifugal compressor design and performance data interpretation. Section 5.1 provides suggestions for effective implementation of numerical performance simulation, while Section 5.2 comments on current design trends.

5.1 Guidelines for Numerical Simulation

Time-accurate unsteady flow simulation of turbomachines has been available for almost a decade, although it is still common in the industry to use steady flow calculations in design. The task of simulating multi-stages, coupled with complex geometries encountered in actual fabrication (seals, exit collectors, etc), is just too demanding on computational resources. To avoid carrying out unsteady flow simulation, engineers have been using body forces, which include deterministic stresses, to simulate the effect of neighboring components. Examples of this approach can be found in [36, 27]. With better understanding of the influence on performance due to interaction established from this investigation, it is possible to provide some insights that can be applied to quasi-steady calculations.

As indicated in Chapter 4, diffuser performance depends primarily on the alignment of the diffuser vanes with the spatially-averaged and time-averaged impeller exit flow angle. The implication is that reasonably accurate prediction on diffuser performance (in terms of C_p and C_{loss}) can be obtained from quasi-steady calculation with the upstream impeller modeled as axisymmetric body forces. This is because the body force model is capable of simulating the *time-averaged* angular momentum generation inside the impeller, while simultaneously allowing the presence of circumferential non-uniformity originated from the vane. With both accounted for, the correct pitchwise distribution of the time-averaged swirl angle at the impeller exit can be established. To further improve the prediction accuracy, modeling of upstream unsteadiness is necessary so that its influence on the diffuser pressure recovery and loss can be captured, especially when the diffuser is operating in an off-design condition.

On the other hand, simulating impeller performance with quasi-steady calculation by replacing the downstream diffuser vanes with asymmetric body forces will have a more serious effect on prediction accuracy because of the effect of unsteady tip leakage flow. As seen in Chapter 3, without the non-axisymmetric pressure field set up by the downstream vanes, the unsteadiness in the tip leakage flow can no longer exist. It is this unsteadiness which substantially alters the blockage and loss associated with tip leakage, which in turn causes a measurable change in impeller performance. Since stage performance depends on both impeller performance and diffuser performance, and impeller performance can be measurably affected by interaction, it is recommended that time-accurate calculation be used for stage performance prediction.

The one-dimensional model developed in Chapter 3 then provides an effective platform to present flow data (obtained from CFD or experiment) for making design decisions, because it shows the trade-off between loss, blockage, and slip which completely cover the detrimental influence to the pressure rise in an adiabatic impeller. More work is nevertheless necessary before the current model can be developed into a fully predictive design tool, as the values of all three factors have to be obtained from three-dimensional time-accurate calculations or experiments.

One other caution should be raised concerning time-accurate calculation, namely the possibility of numerical instability due to flow coupling. Our experience has shown that the quality of the prescribed initial conditions, especially at the entrance to the diffuser, is crucial for achieving convergence. The reason is that the pressure field at the interaction region depends largely on the diffuser performance, as discussed in Chapter 4. If the prescribed diffuser flow incidence is too mis-aligned with the vanes, the pressure field in the interaction region cannot be established correctly, and the impeller performance simulation suffers. As a result, the flow alignment further deteriorates and eventually the simulation fails. It is found that initial conditions built upon individual flow field obtained from single component calculation are adequate for maintaining numerical stability.

In conclusion, flow coupling plays a crucial role in performance simulation, from convergence capability to prediction accuracy. Its effect on prediction accuracy mainly comes from its influence on tip leakage flow behavior, which is a result of the unsteady blade loading.

5.2 Comments on Current Design Trends

In Chapter 3, it is shown that blockage and loss due to the tip leakage flow is detrimental to the impeller pressure rise. Eliminating the tip leakage flow may be an effective way to improve impeller performance. However, tip-clearance gap of current design has basically been brought down to the fabrication tolerance limit and is unlikely to be reduced further without some technology leap, like application of active control to the clearance gap [2]. Meanwhile, engineers have to rely on reducing the blade tip loading to control the amount of tip leakage flow. Introduction of more backsweep near the tip by leaning the blade is an effective way to achieve the reduction.

It is possible to further improve impeller performance by adjusting the balance between the blockage and loss (both closely associated with tip leakage) so that it is optimized for the highest impeller pressure rise. As shown in Chapter 3, the simplest way to accomplish this is to increase flow coupling by reducing the radial gap size between the impeller and diffuser. The main flow mechanism responsible for the consequent reduction of blockage is the higher viscous dissipation rate at the tip leakage due to a more unsteady flow field. Additional benefit also comes in the form of slip reduction because of the stronger potential effect originating from the vanes. However, one should exercise caution in introducing flow coupling , because as demonstrated in Chapter 3, the increased loss can negate the benefit of blockage and slip reduction.

Casing treatment may provide another option in adjusting the blockage-loss balance of the impeller exit flow, although it is more recognized as a measure to widen the stall margin. The one-dimensional model developed in Chapter 3 deals with both blockage and loss, so it can be used to describe the trade-off between loss and blockage when evaluating the effect of casing treatment on impeller pressure rise. Future investigation should be aimed at finding out whether combining flow coupling with casing treatment can further improve impeller performance.

In conclusion, it has been demonstrated that tip leakage is an important flow feature which can measurably affect impeller performance through its influence on blockage and loss. Many design issues arise because of their potential in altering the tip leakage flow behavior. This investigation has shown that one of these geometrical parameters which can lead to such changes is the radial gap size between the impeller and diffuser.

CHAPTER 6

CONCLUSION

A computational investigation has been undertaken to elucidate the effects of impeller-diffuser interaction on the stage performance, especially on stage total-to-static pressure rise. This chapter provides an overview of the research contributions, and explains the implications of these contributions in future centrifugal machine design and performance analysis. Finally, recommendations for further study are outlined.

6.1 Overview of Research Contributions

6.1.1 Generic Findings

The research contributions from this work are summarized as follows. The first two items are generic for any blade row interaction, whether it is impeller-diffuser in centrifugal machines or rotor-stator in axial machines.

- The importance of impeller-diffuser interaction on impeller tip leakage flow and the consequent impact on loss, blockage, slip and ultimately on stage pressure rise has been demonstrated.
- Much of the interaction effect on impeller pressure rise has been captured with a one-dimensional model, although the factors involved, loss, blockage, and slip

have to be obtained from time-accurate calculation.

An example of rotor-stator interaction influence in axial machines can be found in Graf [16], who has observed changes in blockage and loss at the rotor exit after applying different degrees of interaction downstream of the rotor.

6.1.2 Specific Findings

Representative of current design trends, the current impeller being studied has a tip clearance gap size equal to 2% of exit blade height, a 52° backsweep, and an impeller blade-diffuser vane ratio of one to one. Since these geometrical parameters can have significant influence on the quantity of the tip leakage flow and the unsteady forcing which acts on it, they can eventually affect the loss and blockage at impeller exit. On the other hand, the diffuser is operating in a near-design condition, providing little separated flow for unsteadiness to use as a mechanism to influence diffuser performance. As a result, engineers should be cautious in applying the next two conclusions to off-design conditions or to configurations with geometrical parameters very different from the current set.

- The effect of inlet unsteadiness on diffuser pressure recovery and loss has been shown to be similar to that from inlet axial distortions. Both have little influence when compared to the dominant factor, alignment of diffuser vanes with the spatially-averaged and time-averaged flow angle.
- The reason for the association of an optimum impeller-diffuser gap size with the maximum total pressure rise in impeller has been defined. This occurs because the penalty of loss increase overtakes the benefits from blockage and slip reduction when diffuser vanes are placed too close to the impeller blades.

6.2 Implications in Future Design

The implications of the fluid behavior observed in the computed results are summarized in the following:

- The influence of the diffuser is not limited to pressure recovery, but it can also enhance the impeller performance. The influence originates from the pressure field established by the vanes, which in turn affects the tip leakage flow. The consequent influence on impeller performance is found to be significant, as it results in a total-to-total pressure ratio increase by more than 3%.
- Future design of impeller should be aimed at reducing the amount of tip leakage flow. It is thus recommended to reduce the impeller blade tip loading by leaning the blade so that there is more backsweep near the tip.

6.3 Recommendations for Future Study

Additional research is recommended in the following areas:

- The flow fields examined are obtained using CFD. Detailed unsteady flow measurements from physical experiments should be obtained to assess the unsteadiness observed in the tip-leakage flow and the consequent increase of viscous dissipation rate.
- Investigations should be conducted on how to incorporate flow coupling and casing treatment into a single design. Both are known to reduce the blockage associated with tip leakage flow. Whether their combined influence is simply additive and how the combination will impact tip leakage flow behavior remains to be studied.
- It is recommended blade lean be utilized to reduce the amount of tip leakage by decreasing the blade tip loading. Numerical experiments can be conducted to provide design guidelines, especially in terms of the effect on the unsteady blade loading distribution.

- Further numerical experiments can be conducted by applying time-averaged body force modeling to one of the components in the impeller-diffuser configuration effect while retaining discrete blades (or vanes) in the other component. This approach can thus eliminate the unsteadiness aspect from impeller-diffuser interaction. For the configuration modeled with real impeller blades and diffuser body forces, the computed results can quantitatively describe the contribution of unsteadiness to the reduction in slip. Although the inviscid effect from the vanes has been identified as the major contributor to the slip reduction in the current investigation, its importance compared to that associated with the unsteady tip leakage flow remains to be described quantitatively.
- Analytical estimates of the three factors, blockage, loss and slip have to be developed before the one-dimensional model in Chapter 3 can be used as a fully predictive design tool. Modifications can be made to Denton's [11] model on the mixing of tip leakage flow with main flow to estimate the changes in blockage and loss due to interaction influence on tip leakage. Slip modeling can be developed following the approach for its counterpart in axial machines, deviation. Detailed correlations between deviation, blade spacing and camber can be found in Cumpsty [5].

Appendix A

Time-Averaging Procedures for Diffuser Inlet Nodes

This appendix contains the details of the time-averaging procedures for the elimination of unsteadiness at the diffuser inlet boundary for Calculation 4. As mentioned in Chapter 2, the procedures apply conservation principles in the time domain at every inlet boundary node. The following are the discretised equations used in the procedures:

Conservation of mass:

$$\overline{\rho}\,\overline{V_r} = \frac{1}{n}\sum_{i=1}^{n} \rho_i\, V_{ri} \tag{A.1}$$

Conservation of impulse:

$$\overline{p} + \overline{\rho}\,\overline{V_r}^2 = \frac{1}{n}\sum_{i=1}^{n} \left(p_i + \rho_i\, V_{ri}^2\right) \tag{A.2}$$

Conservation of angular momentum:

$$\overline{\rho}\,\overline{V_r}\,\overline{V_t} = \frac{1}{n}\sum_{i=1}^{n} \left(\rho_i\, V_{ri}\, V_{ti}\right) \tag{A.3}$$

Adiabatic:

$$\overline{\rho}\,\overline{V_r}\,\overline{T_0} = \frac{1}{n}\sum_{i=1}^{n}(\rho_i\,V_{ri}\,T_{0i}) \tag{A.4}$$

State:

$$\overline{p} - \overline{\rho}\,R\,\overline{T} = 0 \tag{A.5}$$

Definition of total temperature:

$$\overline{T_0} - \overline{T}\left(1 + \frac{\gamma - 1}{2}\overline{M}^2\right) = 0 \tag{A.6}$$

Definition of Mach number:

$$\overline{M} - \sqrt{\frac{\overline{V_r}^2 + \overline{V_t}^2}{\gamma\,R\,\overline{T}}} = 0 \tag{A.7}$$

where $\overline{\rho}$, $\overline{V_r}$, $\overline{V_t}$, $\overline{p}$, $\overline{T_0}$, $\overline{T}$ and $\overline{M}$ are the 7 unknowns to be solved. Once solved, these 7 variables will form the boundary conditions of the diffuser inlet boundary for Calculation 4. n, the number of time steps in one blade passing, has to be larger than 500 to ensure numerical stability in the interaction region. The instantaneous quantities on the right hand side of the equations are obtained from the computed unsteady flow field. Gauss-Siedel method is found to be the most effective for solving this set of equations (Equations A.1 to A.7).

APPENDIX B

DEVELOPMENT OF ONE-DIMENSIONAL QUASI-STEADY FLOW MODEL

This appendix contains the details for the development of a one-dimensional quasi-steady flow model which describes the response of impeller channel velocity W_2 to changes in loss s and effective flow area A_{eff} (Equations 3.5). The development is based on Shapiro [40]. The equations involved are respectively,

Conservation of mass:

$$\frac{\Delta\rho}{\rho} + \frac{\Delta A_{eff}}{A_{eff}} + \frac{\Delta W}{W} = 0 \tag{B.1}$$

Adiabatic:

$$\frac{\Delta T}{T} + (\gamma - 1) M_{rel}^2 \frac{\Delta W}{W} = 0 \tag{B.2}$$

State:

$$\frac{\Delta p}{p} = \frac{\Delta\rho}{\rho} + \frac{\Delta T}{T} \tag{B.3}$$

Definition of entropy:

$$\frac{\Delta s}{C_{p0}} = \frac{\Delta T}{T} - \frac{\gamma - 1}{\gamma}\frac{\Delta p}{p} \tag{B.4}$$

Rearranging Equations B.1 to B.4 into the following matrix form isolates the two independent variables ($\frac{\Delta A_{eff}}{A_{eff}}$, $\frac{\Delta s}{C_{p0}}$) from the other four dependent variables:

$$\begin{bmatrix} 1 & -1 & -1 & 0 \\ -\frac{\gamma-1}{\gamma} & 0 & 1 & 0 \\ 0 & 1 & 0 & 1 \\ 0 & 0 & 1 & (\gamma-1)M_{rel}^2 \end{bmatrix} \begin{bmatrix} \frac{\Delta p}{p} \\ \frac{\Delta \rho}{\rho} \\ \frac{\Delta T}{T} \\ \frac{\Delta W}{W} \end{bmatrix} = \begin{bmatrix} 0 \\ \frac{\Delta s}{C_{p0}} \\ -\frac{\Delta A_{eff}}{A_{eff}} \\ 0 \end{bmatrix} \tag{B.5}$$

Equations 3.5 can then be obtained by inverting the above matrix:

$$\frac{\Delta W_2}{W_2} = \left[\frac{-1}{1 - M_{rel,2}^2}\right]\frac{\Delta A_{eff}}{A_{eff}} + \left[\left(\frac{\gamma}{\gamma - 1}\right)\left(\frac{1}{1 - M_{rel,2}^2}\right)\right]\frac{\Delta s_2}{C_{p0}}$$

APPENDIX C

BLOCKAGE EVALUATION

This appendix contains the details on the extension of Khalid et al.'s [24] blockage evaluation procedures, intended for axial blade row with steady flow, to the unsteady flow field of an impeller passage.

Similar to that in steady flow, the time-averaged blocked area is,

$$A_{actual} - \overline{A_{eff}} = \overline{B} A_{actual} \tag{C.1}$$

and the time-averaged blockage $\overline{B}$ can be obtained by,

$$\overline{B} = \overline{\left(\frac{\int \left(1 - \frac{\rho W_m}{\rho_e W_e}\right) dA}{\int dA} \right)} = 1 - \frac{\overline{\int \left(\frac{\rho W_m}{\rho_e W_e}\right) dA}}{A_{actual}} \tag{C.2}$$

Thus Khalid et al.'s procedures can be conducted at each time instant and the instantaneous values of B can then be time-averaged to get $\overline{B}$.

Khalid et al. suggested that the velocity gradient cut-off value, which defined the blocked region boundary, should be 2. The expression is,

$$\frac{\mid \nabla(\rho V_m) \mid}{\rho_{avg} C_x / c} = 2 \tag{C.3}$$

Cut-off Value	1.9	2.5	3.8
$r_{2'}/r_2 = 1.092$	+0.96%	+1.04%	+1.11%
$r_{2'}/r_2 = 1.054$	+1.03%	+1.30%	+1.18%

Table C.1: Effect of the velocity gradient cut-off value on the computed $\frac{\Delta A_{eff}}{A_{eff}}$

where C_x is the axial velocity in an axial machine and c is the chord, representing the flow path length. To represent the characteristic dimensions of the present impeller flow field, the channel velocity W_{avg} and the impeller diameter D are more appropriate. Thus the non-dimensional velocity gradient is rewritten as,

$$\frac{\mid \nabla(\rho W) \mid}{(\rho W)_{avg}/D} \tag{C.4}$$

A wide range of cut-off values has been tested. As seen in Table C.1, they all show the same trend for blockage reduction $\frac{\Delta A_{eff}}{A_{eff}}$ when the interaction is stronger. Thus the value of 2.5 is selected as the cut-off criterion.

BIBLIOGRAPHY

[1] ARNDT, N., ACOSTA, A., BRENNEN, C., AND CAUGHEY, T. "Experimental Investigation of Rotor-Stator Interaction in a Centrifugal Pump with Several Vaned Diffusers". *ASME Journal of Turbomachinery, Vol. 112* (1990), pp. 98–108.

[2] BAE, J. W. *Active Control of Tip Clearance Flow in Axial Compressors.* PhD thesis, Department of Aeronautics and Astronautics, Massachusetts Institute of Technology, To be Published.

[3] BAGHDADI, S., AND MCDONALD, A. "Performance of Three Vaned Radial Diffusers with Swirling Transonic Flow". *ASME Journal of Fluids Engineering, Vol. 97* (1975), pp. 155–160.

[4] CLEMENTS, W., AND ARTT, D. "The influence of Diffuser Vane Leading Edge Geometry on the Performance of a Centrifugal Compressor". ASME Paper 89-GT-163 (1989).

[5] CUMPSTY, N. *Compressor Aerodynamics.* Longman Scientific and Technical, Essex, England, 1989.

[6] DAWES, W. "A Simulation of the Unsteady Interaction of a Centrifugal Impeller with its Vaned Diffuser: Flow Analysis". *ASME Journal of Turbomachinery, Vol. 117* (1995), pp. 213–222.

[7] DAWES, W., 1996. Personal Communication.

[8] DEAN, R., AND SENOO, Y. "Rotating Wakes in Vaneless Diffusers". *ASME Journal of Basic Engineering, Vol. 82* (1960), pp. 563–574.

[9] DENIZ, S. "Effects of Inlet Conditions on Centrifugal Diffuser Performance". Massachusetts Institute of Technology, Gas Turbine Lab Report No. 225 (1997).

[10] DENIZ, S., GREITZER, E., AND CUMPSTY, N. "Effects of Inlet Flow Field Conditions on the Performance of Centrifugal Compressor Diffusers Part 2: Straight-Channel Diffuser". ASME Paper 98-GT-474 (1998).

[11] DENTON, J. "Loss Mechanisms in Turbomachines". *ASME Journal of Turbomachinery, Vol. 115* (1993), pp. 621–656.

[12] DOMERCQ, O., AND THOMAS, R. "Unsteady Flow Investigation in a Transonic Centrifugal Compressor Stage". AIAA Paper 97-2877 (1997).

[13] EPSTEIN, A., AND SENTURIA, S. "Macro Power from Micro Machinery". *Science, Vol. 276* (1997), p. 1211.

[14] FILIPENCO, V. "Experimental Investigation of Flow Distortion Effects on the Performance of Radial Discrete-Passage Diffusers". Massachusetts Institute of Technology, Gas Turbine Lab Report No. 206 (1991).

[15] FILIPENCO, V., DENIZ, S., JOHNSTON, J., GREITZER, E., AND CUMPSTY, N. "Effects of Inlet Flow Field Conditions on the Performance of Centrifugal Compressor Diffusers Part 1: Discrete-Passage Diffuser". ASME Paper 98-GT-473 (1998).

[16] GRAF, M. *Effects of Stator Pressure Field on Upstream Rotor Performance.* PhD thesis, Department of Mechanical Engineering, Massachusetts Institute of Technology, 1996.

[17] GRAF, M., AND SHARMA, O. "Effects of Downstream Stator Pressure Field on Upstream Rotor Performance". ASME Paper 96-GT-507 (1996).

[18] GREITZER, E. *Class notes from Internal Flows in Turbomachines.* M.I.T. Department of Aeronautics and Astronautics, 1992.

[19] HETHERINGTON, R., AND MORITZ, R. "Influence of Unsteady Flow Phenomena on the Design and Operation of Aero Engines". *AGARD Conference Proceedings No. 177 on Unsteady Phenomena in Turbomachinery* (1976).

[20] HILL, P., AND PETERSON, C. *Mechanics and Thermodynamics of Propulsion.* Addison-Wesley Publishing Co., Reading, MA, 1992.

[21] INOUE, M. "Radial Vaneless Diffusers: A Re-Examination of the Theories of Dean and Senoo and of Johnston and Dean". *ASME Journal of Fluids Engineering, Vol. 105* (1983), pp. 21–27.

[22] INOUE, M., AND CUMPSTY, N. "Experimental Study of Centrifugal Impeller Discharge Flow in Vaneless and Vaned Diffusers". *ASME Journal of Engineering for Gas Turbines and Power, Vol. 106* (1984), pp. 455–467.

[23] JOHNSTON, R., AND DEAN, R. "Losses in Vaneless Diffusers of Centrifugal Compressors and Pumps". *ASME Journal of Basic Engineering, Vol. 88* (1966), pp. 49–60.

[24] KHALID, S., KHALSA, A., WAITZ, I., TAN, C., GREITZER, E., CUMPSTY, N., ADAMCZYK, J., AND MARBLE, F. "Endwall Blockage in Axial Compressors". ASME Paper 98-GT-188 (1998).

[25] KIRTLEY, K., AND BEACH, T. "Deterministic Blade Row Interactions in a Centrifugal Compressor Stage". *ASME Journal of Turbomachinery, Vol. 114* (1992), pp. 304–311.

[26] KRAIN, H. "A Study on Centrifugal Impeller and Diffuser Flow". *ASME Journal of Engineering for Power, Vol. 103* (1981), pp. 688–697.

[27] LEJAMBRE, C., ZACHARIAS, R., BIEDERMAN, B., GLEIXNER, A., AND YETKA, C. "Development and Application of Multistage Navier-Stokes Solver

Part II: Application to a High Pressure Compressor Design". *ASME Journal of Turbomachinery, Vol. 120* (1998), pp. 215–223.

[28] MARBLE, F., 1998. Personal Communication.

[29] MEECE, C. "Gas Turbine Technologies of the Future". International Symposium on Air Breathing Engines Paper 95-7006 (1995).

[30] MIKOLAJCZAK, A. "The Practical Importance of Unsteady Flow". *AGARD Conference Proceedings No. 177 on Unsteady Phenomena in Turbomachinery* (1976).

[31] MOORE, J., MOORE, J., AND TIMMIS, P. "Performance Evaluation of Centrifugal Compressor Impellers Using Three-Dimensional Viscous Flow Calculations". *ASME Journal of Engineering for Gas Turbines and Power, Vol. 106* (1984), pp. 475–481.

[32] MUGGLI, F., WISS, D., EISELE, K., ZHANG, Z., CASEY, M., AND GALPIN, P. "Unsteady Flow in the Vaned Diffuser of a Medium Specific Speed Pump". ASME Paper 96-GT-157 (1996).

[33] PHILLIPS, M. "Role of Flow Alignment and Inlet Blockage on Vaned Diffuser Performance". Massachusetts Institute of Technology, Gas Turbine Lab Report No. 229 (1997).

[34] PINARBASI, A., AND JOHNSON, M. "Detailed Off Design Flow Measurements in a Centrifugal Compressor Vaned Diffuser". ASME Paper 97-GT-343 (1997).

[35] REGALADO, A. "CPR for the Artificial Heart". *Technology Review, Vol. 102* (1999), pp. 53–55.

[36] RHIE, M., GLEIXNER, A., SPEAR, D., FISCHBERG, C., AND ZACHARIAS, R. "Development and Application of Multistage Navier-Stokes Solver Part I: Multistage Modeling Using Bodyforces and Deterministic Stresses". *ASME Journal of Turbomachinery, Vol. 120* (1998), pp. 205–214.

[37] Rodgers, C. "The Performance of Centrifugal Compressor Channel Diffusers". ASME Paper 82-GT-10 (1982).

[38] Senoo, Y., Kinoshita, Y., and Ishida, M. "Asymmetric Flow in Vaneless Diffusers of Centrifugal Blowers". *ASME Journal of Fluids Engineering, Vol. 99* (1977), pp. 104–114.

[39] Shang, T., Epstein, A., Giles, M., and Sehra, A. "Blade Row Interaction Effects on Compressor Measurements". *AIAA Journal of Propulsion and Power, Vol. 9* (1993), pp. 569–578.

[40] Shapiro, A. *The Dynamics and Thermodynamics of Compressible Fluid Flow*. The Ronald Press Company, New York, USA, 1953.

[41] Storer, J., and Cumpsty, N. "Tip Leakage Flow in Axial Compressors". *ASME Journal of Turbomachinery, Vol. 113* (1991), pp. 252–259.

[42] Tamaki, H., Nakao, H., and Saito, M. "The Experimental Study of Matching between Centrifugal Compressor Impeller and Diffuser". *ASME Journal of Turbomachinery, Vol. 121* (1999), pp. 113–118.

[43] Valkov, T., and Tan, C. "Effect of Upstream Rotor Vortical Disturbances on the Time-Average Performance of Axial Compressor Stators: Part 1 - Framework of Technical Approach and Wake-Stator Blade Interactions". ASME Paper 98-GT-312 (1998).

[44] Valkov, T., and Tan, C. "Effect of Upstream Rotor Vortical Disturbances on the Time-Average Performance of Axial Compressor Stators: Part 2 - Rotor Tip Vortex/Streamwise Vortex-Stator blade Interactions". ASME Paper 98-GT-313 (1998).

[45] Van Zante, D. E., Strazisar, A. J., Wood, J. R., Hathaway, M. D., and Okiishi, T. H. "Recommendations for Achieving Accurate Numerical Simulation of Tip Clearance Flows in Transonic Compressor Rotors". ASME Paper 99-GT-390 (1999).